BIOCHEMICAL, KINETIC AND SPECTROSCOPIC CHARACTERIZATIONS OF NON-HEME IRON OXYGENASE ENZYMES

by

BISHNU P SUBEDI

Presented to the Faculty of the Graduate School of Science
The University of Texas at Arlington in Partial Fulfillment
of the Requirements
for the Degree of

DOCTOR OF PHILOSOPHY

THE UNIVERSITY OF TEXAS AT ARLINGTON
May 2015

Acknowledgements

I would like to express my greatest appreciation and thanks to my advisor Professor Brad S Pierce for giving me the opportunity to work in his lab and providing valuable guidance and encouragement during the research period. I would also like to thank Professor Frank W Foss both for being a member in my thesis committee and a collaborator on MiaE project. My sincerest thanks goes to Professor Frederick MacDonnell for his valuable suggestions as a chair in my thesis committee.

I also thank the Department of Chemistry and Biochemistry at The University of Texas at Arlington for supporting my graduate study, the UTA *Shimadzu Center* for Advanced Analytical Chemistry for the use of HPLC and LC-MS/MS instrumentation utilized in this work, and the UTA Center for Nanostructured Materials for the use of EPR facilities. I would also like to thank Professor Paul Lindahl and Dr. Mrinmoy Chakrabarti, Texas A&M University for their generous assistance in collecting Mössbauer spectra for MiaE, similarly Professor Brian Fox and Justin Acheson, University of Wisconsin, Madison for collaboration on MiaE structural study and Professor Tim Larson, Virginia Tech Department of Biochemistry for the IPTG inducible Azotobacter vinelandii CDO expression vector.

I would like to thank all of my friends in the Dr. Pierce's research group, without whom my research would not have been completed. I would also like to thank my friends and family who have supported me during my graduate study. My special thanks goes to my wife and daughter who were constantly in my side. At the end, I would like to express my appreciation to my father who always advised me to choose a path which has no dead end.

March 18, 2015

Abstract

BIOCHEMICAL, KINETIC AND SPECTROSCOPIC CHARACTERIZATIONS OF NON-HEME IRON OXYGENASE ENZYMES

Bishnu P Subedi, Ph.D.

The University of Texas at Arlington, 2015

Supervising Professor: Brad S Pierce

MiaE is a non-heme diiron enzyme which catalyzes the O_2-dependent hydroxylation of selected tRNA-nucleotides as part of a multienzyme posttranscriptional hypermodification pathway. This tRNA-modifying enzyme is postulated to signal O_2-availability within the pathogenic bacteria, *Salmonella typhimurium*. Recombinant MiaE was cloned from *Salmonella typhimurium genomic DNA*, purified to homogeneity, and characterized by steady-state kinetics and spectroscopic techniques (UV-visible, Circular Dichroism, dual mode electron paramagnetic resonance (EPR), and Mössbauer) for comparison to other non-heme diiron enzymes. Remarkably, regardless of the substrate used in peroxide-shunt assays, hydroxylation of the terminal isopentenyl-C4-position was observed with > 97% *E*-stereoselectivity. The role of tRNA-protein macromolecular interactions on enzymatic reactivity and diiron site conformation was investigated studied using 17 nucleotide RNA oligomer corresponding to the anticodon stem and loop (ACSL) portion of substrate tRNAs. Steady-state reactions utilizing ACSL-substrates were investigated using a recombinant electron transfer chain. A variety of spectroscopic methods were employed to complement kinetic assays and observed structural perturbations within the protein-RNA secondary structure and diiron active site geometry. The tRNA-induced spectroscopic perturbations are reminiscent to be observed in the

hydroxylase component of other monooxygenase enzymes upon binding their corresponding effector-protein. Thus, substrate-enzyme interactions may play a regulatory role in tRNA-hydroxylation for MiaE.

Cysteine dioxygenase (CDO) is a non-heme mononuclear iron enzyme that catalyzes the O_2-dependent oxidation of L-cysteine (L-Cys) to produce cysteine sulfinic acid (CSA). In contrast to mammalian CDO, all known bacterial CDO enzymes lack the Cys-Tyr post-translational modification. The relatively uncharacterized 'Gln-type' bacterial CDO enzymes offer a unique point of comparison to better understand the role of outer-sphere interactions in thiol dioxygense chemistry. In this work, the 'Gln-type' CDO enzyme was cloned from the soil bacteria *Azotobacter vinelandii,* purified to homogeneity, and characterized kinetically and spectroscopically for comparison to the *Mm* CDO enzyme. Remarkably, in steady-state assays using 3-mercaptopropionic acid (3-mpa), L-cysteine (cys), and cyteamine (ca), *Av* CDO exhibits nearly identical maximal velocity ($k_{cat} = v_0/[E]$) for each substrate ($0.2 < k_{cat} < 1.0$ s^{-1}). However, *Av* CDO exhibits a specificity (k_{cat}/K_M = 18,000 $M^{-1}s^{-1}$) for 3-mpa over two orders of magnitude higher than observed for either cys (120 $M^{-1}s^{-1}$) and ca (20 $M^{-1}s^{-1}$). This observations suggests that the 'Gln-type' *Av* CDO enzyme has been misannotated as a cysteine dioxygenase and is, in fact, a 3-mercaptopropionic acid dioxygenase (MPDO). Complementary X-band EPR experiments were performed on *Av* CDO using nitric oxide as a surrogate for O_2-binding. As with most non-heme mononuclear iron oxidase/oxygenase enzymes, *Av* CDO exhibits an obligate ordered addition of substrate (3-mpa, cys, and ca) prior to NO. Previously published results demonstrate that the electronic structure of the substrate-bound iron-nitrosyl produced in *Mm* CDO (*Mm* ES-NO) exhibits an unusual $\{FeNO\}^7$ ($S = 1/2$) electronic ground state. In stark contrast to this, the *Av* ES-NO exhibits a $\{FeNO\}^7$ ($S = 3/2$) species with near axial magnetic symmetry ($E/D = 0.009$).

Table of Contents

List of Illustrations

List of Tables

Chapter 1

Introduction

Metalloenzymes

Nearly one third of all enzymes require metal cofactor(s) to function properly. Among these, the oxidase/oxygenase class of Fe/O_2-dependent metalloenzymes remains one of the most extensively characterized enzymes to date. While the mechanistic paradigm of the heme-dependent monooxygenases such as cytochrome P450 has been extensively characterized, fewer mechanistic details are available for the analogous non-heme diiron monooxygeanse enzymes. This diverse family of enzymes has been identified all throughout the biological kingdom and is capable of catalyzing an impressive array of chemical oxidations (mono- and dioxygenations, aliphatic desaturation). Despite accommodating a broad spectrum of substrates, the first-coordination sphere of the diiron active site is essentially conserved among non-heme diiron oxidase/oxygenase enzymes.

Heme vs non-heme iron enzymes

Heme monooxygense enzymes contain a 5-coordinate iron site coordinated equatorially by protoporphyrin IX macrocyclic ligand and axially by a single protein derived amino acid (Try, Cys, His). The peripheral substituents of the porphyrin tetrapyrole ring varies greatly among heme-metalloproteins (heme a, b, c, d, o, and seroheme), however, the monooxygenase class of enzymes uniformly utilize only the heme b cofactor (*1*). Since the heme b macrocycle is uniform, the activity of these monooxygenase enzymes is largely modulated by the nature of the protein derived axial ligand (*proximal side*). Within cytochrome P45O, the heme b moiety is coordinated to a proximal Cys-thiolate. The O_2-binding site is trans to the proximal Cys-residue. The stability of the Fe-bound O-O bond is largely influenced by distal hydrogen-bonding interactions within the active site cavity.

Figure 1.1 A illustrates the typical heme b active site observed among cytochrome P450 enzymes.

In stark contrast to the heme monooxygenase enzymes, the active site of non-heme iron oxygenase/oxidase enzymes are comprised of either a mononuclear or binuclear iron active site coordinated by histidine and carboxylate ligands as illustrated in Figure 1.1 B (*2*). From a basic characterization point of view, the heme cofactor gives rise to intense ($\varepsilon_{\sim 400nm}$ > 100,000 M^{-1} cm^{-1}) π-π* and ligand to metal charge transfer (LMCT) transitions which can be readily interrogated by UV-visible spectroscopy (*2*). By comparison, LMCT transitions are vastly attenuated ($\varepsilon_{300\text{-}400}$ 4000-7000 $M^{-1}cm^{-1}$) or lacking among non-heme iron enzymes (*3, 4*) thus making these enzymes significantly more challenging to characterize.

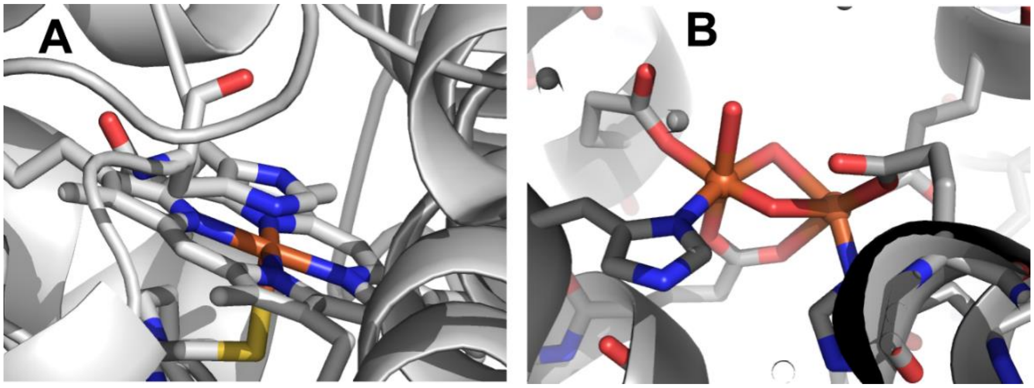

Figure 1.1 X-ray crystal structures comparing the active site of heme and non-heme monoxoygenase enzymes. A. Cytochrome P450 (pdb 2DOE) isolated form Streptomyces coelicolor and B. the non-heme diiron site within the hydroxylase component of methane monooxygenase (MMOH) (pdb 1MTY) isolated from *Methylococcus capsulatus* (Bath).

Non-heme iron oxidase/oxygenases and activation of molecular oxygen

Reaction of organic molecules with molecular oxygen is thermodynamically favorable but this phenomenon is kinetically controlled due to violation of total spin conservation law (triplet oxygen vs singlet products)(*5-7*). This kinetic barrier is easily overcome by metalloenzymes, which contain transition metals within their active site. The enzymatic metallocenters can exist in paramagnetic oxidation states, thus allowing for direct reaction with molecular oxygen (*8*). Most of the non-heme iron enzymes activate oxygen (except hemerythrin and ferritin) to initiate a vast array of chemical oxidation reactions [hydroxylations (mono or di), aliphatic desaturation, ring cyclization, halogenations, and H-atom abstraction] (*6*). Oxygen activating non-heme iron enzymes are an important area of mechanistic study due to their capacity to activate otherwise unreactive C-H bonds, chemo- and stereo-specifically. In principle, a greater understanding of the substrate-gated events involved in orchestrating formation of high-valent Fe-oxo intermediates in this enzyme family could pave the way toward the development of small biomimetic model complexes for use in industrial oxidations.

Table 1.1 Common oxygen activating mononuclear non-heme iron enzymes (Fe(II) dioxygenases)

Enzyme groups	Function
2 His / 1 carboxylate	
a) Extradiol catechol dioxygenase	C-C bond in catechol is oxidized to give 2-hydroxymucaldehyde acid
b) α-keto glutarate dioxygenase	C-H bond activation/ oxidation in hydrocarbons
c) Rieske dioxygenase	cis-dihydroxylation of arenes to cis-dihydro-diol products
3 His 'facial triad'	
Cysteine dioxygenase (CDO)	Oxidation of L-cysteine to cysteine sulfinic acid

Non-heme mononuclear iron enzymes (2-His-1-carboxylate facial triad)

Non-heme mononuclear iron dioxygenase enzymes react directly with molecular oxygen without the requirement for an external reductant. Typically this class of enzymes contain a single ferrous iron coordinated by 2-His residues and single carboxylate (Glu/Asp) ligand along one face of an octahedron. This leaves the opposite octahedral face available for substrate and/or O_2-binding (*9*). This active site configuration is commonly referred to as the 2-His-1-carboxylate facial triad motif (Table 1.1) (*2, 10*).

.As shown in Table 1.1, there are numerous examples of non-heme mononuclear dioxygenases enzymes containing a 2-His-1-carboxylate active site motif. Figure 1.2 illustrates the general O_2-activation mechanism observed for the extradiol-cleaving catechol dioxygenases. These enzymes catalzyze the O_2-dependent oxidation of the carbon-carbon bond of aromatic ring outside of the alcohol to produce 2-hydroxymucaldehyde acid (*10*).

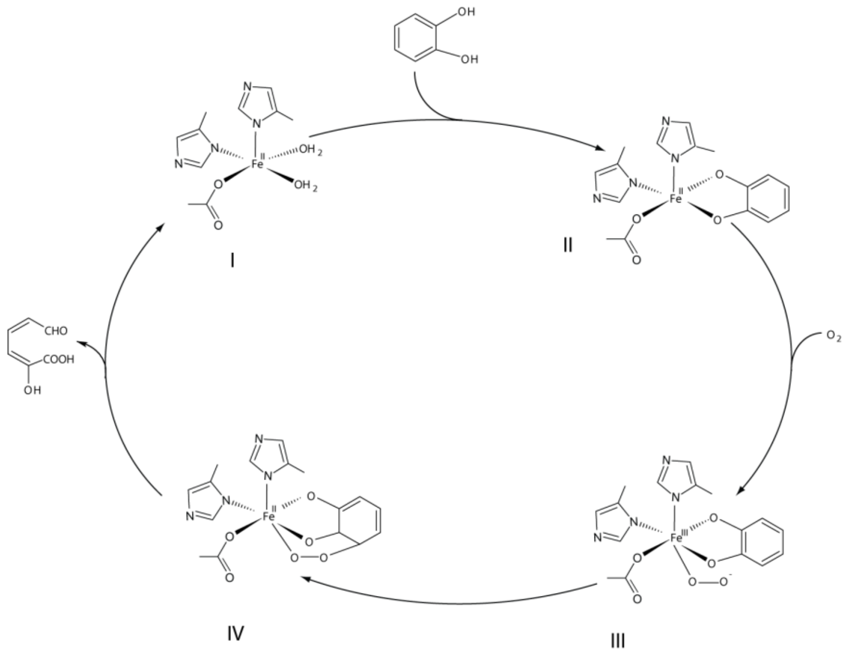

Figure 1.2 Proposed catalytic cycle of an extradiol dioxygenase

Another common subclass of this enzyme family is the α-ketogluterate/O_2-dependent non-heme mononuclear iron enzymes. While the 2-His-1-carboxylate motif is conserved among this class of dioxygenases, these enzymes exhibit an obligate need for α-ketogluterate as a co-substrate during the catalytic turnover (*2, 5, 10*). As illustrated in Figure 1.3, the functionalization of an unactivated C-H bond occurs in parallel with the oxidative decarboxylation of a α-ketogluterate.

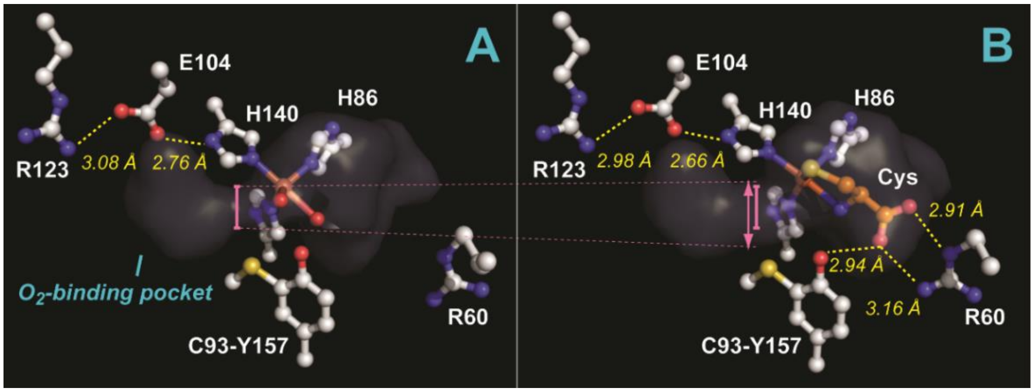

Figure 1.3 CDO crystal structure. 1.6 Å resolution crystal structures for the resting [A] (PDB code 4IEZ) and substrate-bound [B] (PDB code 4IEV) mammalian CDO active site at pH 8.0.(*21*) The available cavity space surrounding the active site is indicated by the transparent surface map

Recently, considerable attention has been focused on the mammalian thiol dioxygenase enzymes (TDO) cysteine dioxygenase (CDO) and cysteamine (2-aminoethanethiol) dioxygenase (ADO). Of the TDO enzymes, mammalian CDO is the best characterized(*11-14*). This enzyme catalyzes the first committed step in the catabolic dissimilation of Cys to produce inorganic sulfate, pyruvate, hypotaurine, and taurine (*15, 16*). Intracellular Cys concentration is the limiting factor in GSH synthesis, therefore the activity of CDO directly competes with cellular redox buffering under conditions of low Cys availability and oxidative stress (*17*). While results from steady-state kinetics of CDO are available, few direct mechanistic details are known regarding the [Fe-O] intermediates involved in thiol-oxidation (*18-20*).

Multiple high-resolution crystal structures of the resting and substrate-bound enzyme have been solved which highlight the atypical mononuclear iron coordination for the mammalian CDO active site (*21-25*). As illustrated in Figure 1.3, the active site coordination of CDO is comprised of iron ligated by the N_{ε}-atoms of His86, His88, and His140, representing a new 3-His variant on the classic 2-His-1-carboxylate facial triad observed in mononuclear non-heme iron enzymes (*26*). To date only 2 enzymes with a 3-His facial triad motif (CDO and diketone dioxygenase, Dke1) have been crystallographically (*27*) and spectroscopically characterized (*28, 29*). On the basis of sequence homology, it has been proposed that the active site of mammalian ADO also contains a 3-His facial triad (*30*). Furthermore, two bacterial TDO enzymes isolated from *Variovorax paradoxus* [mercaptosuccinate dioxygenase, (MSDO) and 3-mercaptopropionate dioxygenase (MPDO)] also exhibit a similar 3-His metal binding sequence analogous to CDO (*31, 32*). The conserved 3-His metal binding site observed among all known TDO enzymes suggest that the first-coordination sphere represents a key feature necessary for oxidation of thiols.

Another unusual feature within the mature eukaryotic CDO active site is a post-translational modification 3.3 Å from the Fe-center in which spatially adjacent Cys93 and Tyr157 residues are covalently cross-linked to produce a C93-Y157 pair. Among CDO enzymes identified, Y157 is conserved across phylogenic domains, whereas the C93-Y157 pair is unique only to eukaryotes. An analogous post-transcriptional modification has been observed in only three other enzymes previously(*33-35*). Since one of these enzymes is the copper-radical enzyme, galactose oxidase (GO), it was initially proposed that a Tyr-Cys radical may also be involved in the CDO catalytic cycle (*25*). However, a variety of studies involving C93/Y157 active site variants and known radical scavengers have demonstrated that the C93-Y157 pair is not redox active during native catalysis (*25, 36, 37*). The exact mechanism of C93-Y157 formation remains unresolved.

Prior to the addition of O_2, Cys coordinates to the mononuclear ferrous site of CDO in a bidentate fashion through a thiolate and neutral amine (*22, 25, 37*). As illustrated in Figure. 1.3B, additional ligation of the Cys thiol-group within the trigonal plane opposite H86 and H88 positions the carboxylate group of Cys favorably for charge stabilization by the R60 guanidinium group. While the overall coordination number remains constant, the Fe-site geometry is altered upon substrate binding to produce a pseudo-square pyramidal ($\sim C_{4V}$) geometry. It is expected that this geometric perturbation would significantly increase the O_2-reactivitiy of the Fe-site.

One feature that is becoming increasing apparent is the role of the C93-Y157 pair in providing appropriate substrate orientation and stereo-selectivity. The bidentate substrate coordination provides two points of simultaneous interaction. A third point of interaction is produced by hydrogen bonding between the Cys-carboxylate group and the C93-Y157 pair (2.94 Å). This third interaction is also stabilized electrostatically by interaction with R60 (separated by 2.91 - 3.16 Å). Collectively, these interactions satisfy the "*three point interaction rule*" for chiral selection.(*38*) In support of this model, several reports published demonstrate that cross-link formation increases the catalytic activity, (O_2/CSA)-coupling efficiency of CDO, and substrate-specificity (*36, 39, 40*).

Within the 2-His-1-carboxylate family of non-heme iron containing oxidases and oxygenases, a general mechanism for catalysis has emerged based on extensive synthetic, mechanistic, spectroscopic, and crystallographic characterization(*41-43*). Typically, the monoanionic active site contains a 5 or 6-coordinate ferrous iron with solvent molecules serving as the non-protein ligands. In the absence of substrate and/or cofactor, the reduced active site is unreactive toward O_2 (*43*). Based on this model, at least two reasonable reaction pathways have been proposed for CDO, which ultimately lead to the production of CSA and a ferrous iron resting state for the enzyme (*23, 37, 44-46*). A detailed discussion of these potential mechanisms is presented (*47*).

A common feature for all reaction mechanisms proposed is the formation of a transient substrate-bound Fe^{III}-superoxo species (*B*). Indeed, ferric-superoxide intermediates have been proposed for several 2-His-1-carboxylate non-heme mononuclear iron enzymes including isopenicillin-N-synthase (IPNS), 1-aminocyclopropane-1-carboxylic acid oxidase (ACCO), and hydroxyethylphosphonate dioxygenase (HEPD)(*48-50*). In heme-containing enzymes, a variety of ferric-superoxide intermediates have been crystallographically and spectroscopically characterized(*51-53*). However, to date, only one such example has been identified within this class of non-heme iron enzymes (2, 3-HPCD)(*54*). Interestingly, the catalytically active, Mn^{II}-substituted form of 2, 3-HPCD also produces a transient Mn^{III}-superoxo species upon addition of oxygen to the substrate-bound enzyme (*55, 56*). Whether or not Fe^{III}-superoxo intermediates are a common mechanistic intermediate for oxidase and oxygenase enzymes is currently a matter of debate.

Scheme 1.1 Summary of mechanisms proposed for CDO-catalyzed oxidation of Cys to produce CSA.

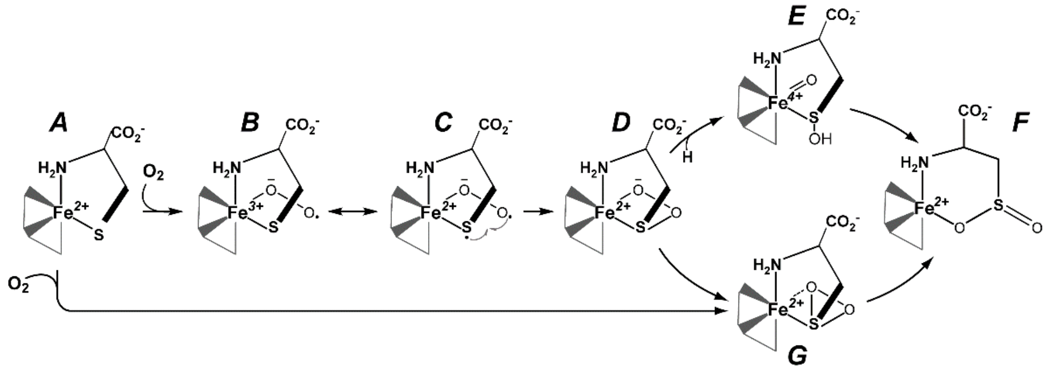

We previously demonstrated that the catalytic cycle of CDO can be '*primed*' by 1-electron through chemical oxidation to produce CDO with ferric iron in the active site (*47*). While catalytically inactive, the substrate-bound form of Fe^{III}-CDO is more amenable to interrogation by UV-visible and EPR spectroscopy than the '*as-isolated*' Fe^{II}-CDO enzyme. Chemical-rescue experiments were performed in which superoxide ($O_2^{\bullet -}$) was introduced to the substrate-bound Fe^{III}-CDO to produce and spectroscopically (EPR and UV-visible) characterize a transient intermediate kinetically matched to CSA formation. Tentatively, this intermediate has been assigned as a substrate-bound Fe^{III}-superoxide species. While it is not clear if this transient species is produced within the native catalytic cycle of CDO, it offers a point of comparison to intermediates observed in other non-heme mononuclear iron enzymes. This work also represents the first reported instance of superoxide-rescue to produce transient intermediates within a non-heme iron enzyme.

Non-heme diiron enzymes

Non-heme enzymes and model complexes have historically attracted considerable interest in the realm of bioinorganic chemistry. This intense focus of research efforts can largely be explained by the vast number of functionally (and structurally) diverse enzymes identified throughout the biological kingdom and the incredible versatility exhibited in chemical oxidations (mono- and dioxygenations, aliphatic desaturation) they initiate (*57*). Remarkably, all of these divergent oxidations are facilitated by minor perturbations to what is essentially a conserved first-coordination sphere to the diiron cluster. Table 1.2 shows some notable enzymes of non-heme diiron enzyme family along with their biological function (*3, 4, 58-63*).

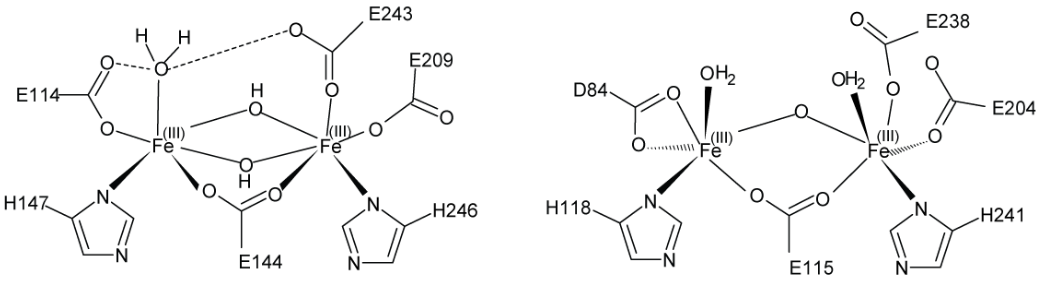

MMOH

RNR-R2

Figure 1.4 Active site structures of non-heme diiron enzymes

Table 1.2 Common non-heme diiron enzymes

Protein/source	Substrate	Function of diiron center
Hemerythrin (Hr)/ marine invertebrates	O_2	reversible binding of O_2, analogous to hemoglobin
R2 component of Ribonucleotide reductase/ mammals, *E. coli*, viruses	tyrosine residue	formation of a catalytically essential tyrosine radical necessary for dNTP synthesis
Ferritin (Fr)/ vertebrates, bacteria	ferrous iron	storage of physiological iron (Ferroxidase)
Tolune-4-monooxygenase (T4moH)/ *Pseudomonas*	toluene	O_2 dependent oxidation of toluene to produce p-cresol
Methane monooxygenase (MMOH)/ Methanotropic bacteria	methane	O_2 dependent oxidation of methane to produce methanol
Stearoyl-ACP Δ^9-desaturase Δ9D / higher plants	stearoyl-ACP	regiospecific insertion of a *cis*-double bond in fatty acid precursors between C9 and C10.

Among this family of enzymes are the hydroxylase enzymes of the bacterial multicomponent monooxygenases (methane monooxygenase MMOH; toluene 2-(or 4-) monooxygenase, T2mOH, T4mOH; the small subunit of ribonucleotide reductase (R2 of RNR), and the soluble stearoyl-acyl carrier protein Δ^9-desaturase (Δ9D)(*3, 4, 58-60*). In spite of their conserved first coordination sphere (Figure 1.4), they can perform diverse reactions utilizing molecular oxygen in presence of reductive equivalents as shown in Figure 1.5. For example, MMO catalyzes the 2 electron oxidation of methane to produce methanol. Alternatively, the small subunit (R2) of RNR generates tyrosine radical which is ultimately used to reduce ribonucleotides to deoxyribonucleotide, and Δ9D creates double bond selectively in saturated fatty acids (*3, 4, 64*). The resting state of this class of enzymes is diferric (Fe^{III}-Fe^{III}) and thus the exogeneous electrons are required prior to activation of oxygen. In most cases, the terminal source of electrons is NADH or NADPH. A separate oxidoreductase enzyme is generally required for delivery of these electrons to the diiron active site (*60*).

The catalytic mechanism of the hydroxylase component of methane monooxygenase (MMOH) has been extensively studied. According to proposed reaction mechanism of MMOH (Figure 1.6), the enzyme activation starts with the reduction of resting diiron enzyme by two electrons. The reduced diferrous center now reacts with molecular oxygen to generate a peroxo diferric complex (intermediate P). This peroxo diiron(III) species immediately transform into intermediate Q; a di(μ-oxo)iron(IV) species. This high-valent diferryl iron species (Q), an oxidizing intermediate, is responsible for substrate oxidation (*60*).

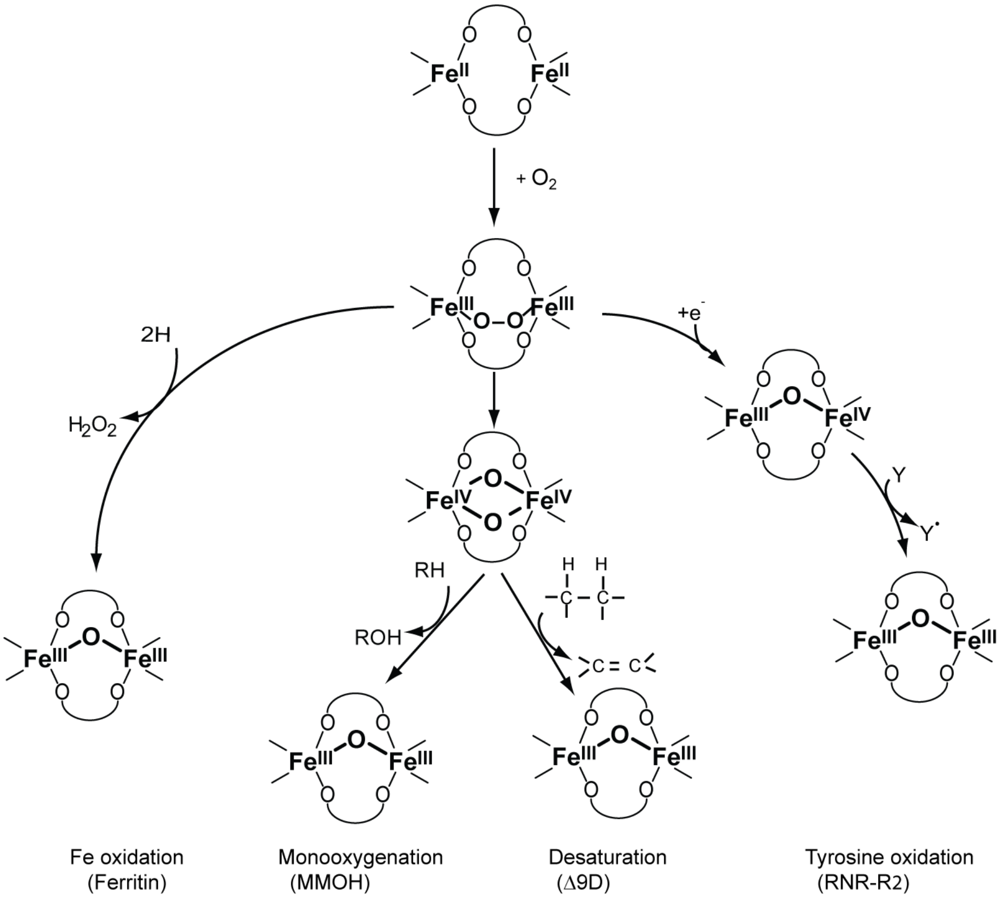

Figure 1.5 General enzymatic reaction pathways of non-heme diiron enzymes.

In their native form, the typical quaternary protein structure observed in non-heme diiron enzymes is multimeric (*65*). This protein configuration raises the possibility for inter-protomer communication and potential for '*half-sites*' reactivity. These factors significantly complicate functional characterization for this class of enzymes. For example, among the hydroxylase components of bacterial multicomponent monooxygenase (BMM) enzymes, a non-covalent heterotrimeric dimer complex $(\alpha\beta\gamma)_2$ is the most frequently observed protein configuration (*66*). By contrast, the simplest quaternary structure reported for non-heme diiron enzymes is homodimeric (α_2). To illustrate, both the small subunit of ribonucleotide reductase (R2) and stearoyl-acyl carrier protein (18:0-ACP) Δ^9-desaturase (Δ9D) exhibit a homodimeric protein configuration in which each protomer contains a diiron active site (*57, 67, 68*). Interestingly, it has been reported that both Δ9D and R2 exhibit properties consistent with '*half-sites*' reactivity; implying that the two protomers of these homodimeric enzymes do not act independently during catalysis(*69-72*). Rapid-mix/chemical quench experiments with Δ9D demonstrate the most compelling evidence for '*half-sites*' reactivity within a non-heme diiron enzyme. In these reactions the pre-reduced enzyme-substrate complex [Δ9D:18:0-ACP] was rapidly mixed with O_2-saturated buffer prior to chemical quenching at selected time points. The observed product (18:-1-ACP) formation followed two distinct kinetic phases, an initial 'burst-phase' (k_{burst} ~ 95 s^{-1}) followed by a second linear phase (k_{linear} ~ 4 s^{-1})(*73*). As the Δ9D is a homodimer, each protomer has an equivalent diiron site capable of generating product and thus the expected amplitude of this burst phase should be twice the protein concentration. Remarkably, the observed amplitude in these experiments was roughly equivalent to one product (18:1-ACP) generated per Δ9D homodimer. On the basis of these experiments it was concluded that the two active sites within Δ9D are not simultaneously catalytically active.

By contrast, the O_2-activation within the diiron site of R2 represents a single turnover event, which can best be described as post-transcriptional modification of an endogenous tyrosine residue to create a stable tyrosine radical. Regardless, even in the absence of catalytic turnover, evidence for inter-subunit cooperatively was observed during the binding of metal within apoR2. In this work it was demonstrated that metal binding within a single protomer (β_I) of the R2 homodimer initiates a negative allosteric effect, which prevents metal binding within the adjacent protomer (β_{II}). Furthermore, metal incorporation into the second β_{II}-protomer only occurs during or after O_2-activation at the intact diiron site within the β_I-protomer(*74, 75*).

An additional complication arises from the fact that the active site located within one protomer is spectroscopically indistinguishable from an active site on an adjacent protomer generates an inherent ambiguity in assigning spectroscopic features. Thus, despite a wealth of mechanistic and structural studies on non-heme diiron enzymes, to date our fundamental understanding of how the protein environment modulates the reactivity of the diiron cluster remains somewhat superficial.

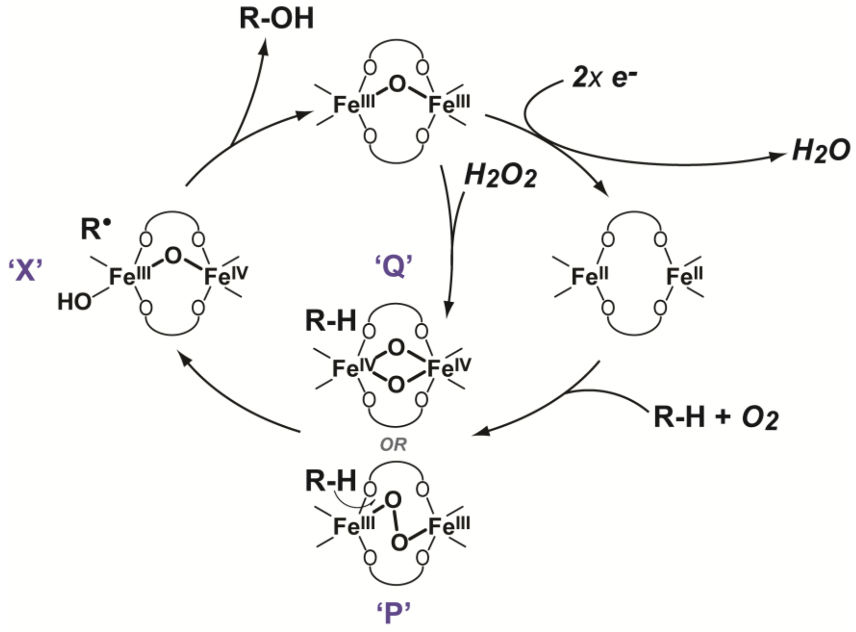

Figure 1.6 General enzymatic reaction pathway of non-heme diiron monooxygenases

A potential solution to these problems comes in the form of a recently characterized non-heme diiron enzyme (MiaE) isolated from S*almonella typhimurium*(*76-78*). MiaE catalyzes the O_2-dependent hydroxylation of a hypermodified tRNA nucleotide at position 37 ($ms^2i^6A_{37}$) to produce 2-methylthio-N^6-(4-hydroxyisopentenyl)-adenosine

($ms^2io^6A_{37}$). In facultative anaerobic bacteria such as *S. typhimurium,* it has been postulated that the extent of A_{37}-hydroxylation is a signaling event in the regulation of aromatic amino acid uptake, enterochelin synthesis, iron transport, and aerobiosis(*79-83*). Remarkably, this enzyme exhibits a monomeric (α) protein configuration (*one active site within a single protomer*) as indicated by size exclusion chromatography (13), analytical ultracentrifugation (24), and X-ray crystallography (*presented here*). To our knowledge, this is the first example of a monomeric non-heme diiron oxygenase/oxidase. This enzyme represents an unprecedented opportunity to study a minimal non-heme diiron catalytic system in the absence of any potential for inter-protomer cooperativity. By contrast to this enzyme, MiaE isolated from *Pseudomonas putida* (pdb code 2ITB) exhibits the typical homodimeric (α_2) protein configuration observed among most non-heme diiron enzymes. Characterization of both enzyme forms provides an unparalleled opportunity to directly observe differences in reactivity between a monomeric and homodimeric non-heme diiron enzyme forms. Moreover, the structural factors influencing tRNA-recognition for MiaE are poorly understood and its impact on enzymatic activity is completely unexplored.

Background on tRNA post-transcriptional modifications

Transfer ribonucleic acid (tRNA) molecules are the essential components of protein synthesis machinery. tRNA molecules appear to be highly modified within the cell to perform their roles more efficiently. The shortcoming of nucleosides to perform multiple function by this biopolymer in translational machinery is partly fulfilled by the modification of the four canonical nucleosides (adenosine, guanosine, cytidine, and uridine) by creating micro-heterogeneity in the tRNA molecules. Modifications decorate the nucleosides in tRNA by the addition of small groups with the help of specific modifying enzymes after transcription (*84*).

To date, nearly 90 post-transcriptional modifications of transfer RNA (tRNA) have been identified across all phylogenic domains of life *(85, 86)*. Given the central role of tRNA to protein biosynthesis, the enzymes involved in catalyzing these modifications serve as critical checkpoints to synchronize production of specific proteins to cellular events(*87*). For instance, specific RNA modifications have been identified which are closely related to both viral and bacterial virulence [human immunodeficiency virus (HIV), *Salmonella*, and *Shigella*]. Since tRNAs found in higher eukaryotic organisms are more extensively modified as compared to bacterial and viral tRNAs, it has been proposed that tRNA modifications may facilitate immune self-discrimination; allowing the host to differentiate between its endogenous tRNA and that of an infectious organism. Moreover, several human disease states have been directly linked to improperly spliced or modified tRNA molecules [cancer, type 2 diabetes, and mitochondrial-linked disorders]. Consequently, the regulation of enzymes involved in tRNA-modification represents a largely unexplored but potentially important new path to control infectious organisms and improve human health.

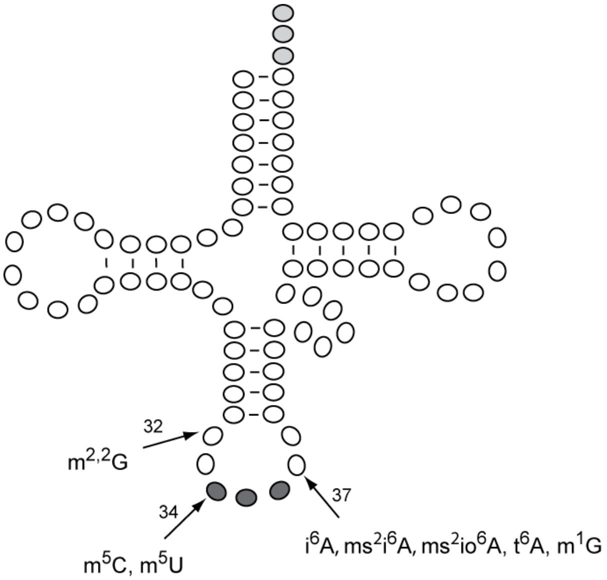

Figure 1.7 Common posttranscriptional modifications in anticodon site of tRNA

Within the antistem codon loop (ASL) of tRNA, nucleoside modifications are frequently observed at position 34 (the wobble position) or position 37 (3' adjacent to anticodon)(*81, 88*). In many instances modification of the nucleoside involves a single chemical step such as the addition of a methyl or methylthiol group to the base. Alternatively, some modifications employ multiple enzymes within a complex biochemical pathway to produce hypermodified nucleotides. For instance, nearly all eukaryotic and bacterial tRNAs that read codons starting with U are modified by the enzymes MiaA and MiaB as illustrated in Scheme 2. In the first step, dimethylallyl (Δ^2-isopentyl) diphosphate-tRNA transferase [E.C. 2.5.1.8] (designated MiaA) catalyzes the nucleophilic substitution of the dimethylallyl group from dimethylallyl pyrophosphate (DMAPP) to the exocyclic 6-amino nitrogen of A_{37} (N^6) to yield N^6-isopentenyl-adenosine (i^6A_{37}) with release of inorganic pyrophosphate.(*89*) The second enzymatic transformation involves the formal methylthiolation of i^6A_{37} at the C2-position to produce 2-methylthio-N^6-isopentyl-adenosine ($ms^2i^6A_{37}$). The enzyme that catalyzes this remarkable transformation (2-methylthio-N^6-isopentenyl-adenosine synthase, designated MiaB) requires S-adenosylmethionine as a co-substrate and is a member of the radical *S*-adenosylmethionine (SAM) methylthiotransferase family of enzymes(*90-92*). With the notable exception of $tRNA_{I,V}^{Ser(GGA)}$, nearly all eukaryotic and bacterial tRNAs that read codons starting with U contain the ms^2i^6A-modification (*79, 93*).

While absent in eukaryotes, some facultative bacteria utilize a non-heme diiron enzyme (MiaE, 2-methylthio-N^6-isopentenyl-adenosine(37)-tRNA monooxygenase) to catalyze the O_2-dependent hydroxylation of $ms^2i^6A_{37}$ to produce 2-methylthio-N^6-(4-hydroxyisopentenyl)-adenosine ($ms^2io^6A_{37}$)(*77*). While MiaE can utilize i^6A_{37} as a substrate, whole cell assays suggest a preference for $ms^2i^6A_{37}$(*94-96*). MiaA and MiaB are common in both eukaryotes and prokaryotes (*82*); however, MiaE is found within a small subset of facultative anaerobic bacteria such as S*almonella typhimurium*. It has been postulated that within these bacteria the extent of A_{37}-hydroxylation is involved in regulating aromatic amino acid uptake, enterochelin synthesis, iron transport, and aerobiosis (*79-83*).

Scheme 1.2 The MiaA, MiaB, and MiaE hypermodification pathway

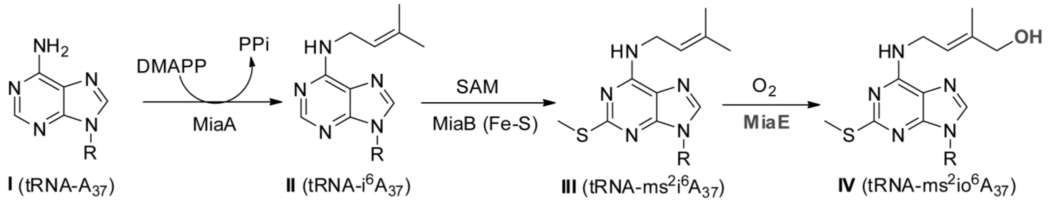

Sequence alignment and spectroscopic characterization (EPR/Mössbauer) of MiaE indicate that it is a member of the non-heme diiron family of enzymes (*77, 78, 83*). Other members of this family include the hydroxylase components of the bacterial multicomponent monooxygenases (BMM) [methane monooxygenase (MMOH), toluene-monooxygenases (ToMOH)], the small subunit of ribonucleotide reductase (R2), and stearoyl-acyl carrier protein Δ^9-desaturase (Δ9D)(*57, 67, 68*). The mechanistic paradigm for this class of enzymes starts with the 2 electron reduction of the resting diferric center to produce a diferrous cluster. The diferrous center can then react with molecular oxygen to produce a high-valent oxidizing species capable of substrate oxidation(*77, 97-99*). For example, the hydroxylase component of methane monooxygenase (MMOH) from *Methylococcus capsulatus* (Bath) is one of the most extensively characterized non-heme diiron enzymes(*100-102*). In this enzyme, a high-valent diferryl iron species, termed compound Q, has been identified as the oxidizing intermediate responsible for substrate oxidation (*103, 104*). Alternatively, a diferric peroxo species has been proposed to be the catalytically competent intermediate in the ToMOH-catalyzed oxidation of aromatic hydrocarbons (*105*). As with heme oxidase enzymes, many non-heme diiron enzymes exhibit a ‘peroxide-shunt’ pathway in which the high valent substrate-oxidizing intermediate can be produced by addition of hydrogen peroxide to the resting diferric enzyme. This pathway removes the need for an external electron source, but frequently at the cost of product yield and specificity (*67, 68, 97*).

Chapter 2

Peroxide-shunt substrate-specificity for the Salmonella typhimurium O2-dependent tRNA modifying monooxygenase (MiaE)

Andra L. Corder, Bishnu P. Subedi, Siai Zhang, Amanda M. Dark, Frank W. Foss, Jr., and Brad S. Pierce, Department of Chemistry and Biochemistry, College of Science, The University of Texas at Arlington, Arlington, Texas 76019 (This work was published on *2013, Biochemistry 52*, 6182-6196)

Abstract

Post-transcriptional modifications of transfer RNA (tRNA) are made to structurally diversify tRNA. These modifications alter non-covalent interactions within the ribosomal machinery, resulting in phenotypic changes related to cell metabolism, growth, and virulence. MiaE is a carboxylate bridged, non-heme diiron monooxygenase, which catalyzes the O_2-dependent hydroxylation of a hypermodified-tRNA nucleoside at position 37 (2-methylthio-N^6-isopentenyl-adenosine(37)-tRNA) [*designated* $ms^2i^6A_{37}$]. In this work, recombinant MiaE was cloned from *Salmonella typhimurium*, purified to homogeneity, and characterized by UV-visible and dual-mode X-band EPR spectroscopy for comparison to other non-heme diiron enzymes. Additionally, three nucleoside substrate-surrogates (i^6A, Cl^2i^6A, and ms^2i^6A) and their corresponding hydroxylated products (io^6A, Cl^2io^6A, and ms^2io^6A) were synthesized to investigate the chemo- and stereospecificity of this enzyme. In the absence of the native electron transport chain, the peroxide-shunt was utilized to monitor the rate of substrate hydroxylation. Remarkably, regardless of the substrate (i^6A, Cl^2i^6A, and ms^2i^6A) used in peroxide-shunt assays, hydroxylation of the terminal isopentenyl-C4-position was observed with > 97% *E*-stereoselectivity. No other non-specific hydroxylation products were observed in enzymatic assays. Steady-state kinetic

experiments also demonstrate that the initial rate of MiaE hydroxylation is highly influenced by the substituent at the C2-position of the nucleoside base (v_0/[E] for $ms^2i^6A > i^6A > Cl^2i^6A$]. Indeed, the > 3-fold rate enhancement exhibited by MiaE for the hydroxylation of the free ms^2i^6A nucleoside relative to i^6A is consistent with previous whole cell assays reporting the io^6A and ms^2io^6A product distribution within native tRNA-substrates. This observation suggests that the nucleoside C2-substituent is a key point of interaction regulating MiaE substrate specificity.

Introduction

Post-transcriptional modifications of transfer RNA (tRNA) have been identified across all phylogenic domains of life (*Archaea, Bacteria,* and *Eucarya*) (*93*). Ironically, more genes are devoted to enzymes involved in the modification of tRNA nucleosides than to the various tRNA genes themselves (*93, 106*). These modifications are made to structurally diversify tRNA from the four canonical nucleoside building blocks [adenosine,(A); guanosine, (G); uridine, (U); and cytosine, (C)] (*107*). At present, nearly 90 structurally unique nucleoside modifications have been identified in tRNA (*93*). In many instances, the physiologic role of such modifications is unclear; however, several examples have been identified to suggest that the presence of modified nucleosides in tRNA can impact central metabolism (*citric acid cycle*), thiamine biosynthesis, and bacterial virulence (*108*). Of these modifications, perhaps the best understood are those localized within the anticodon stem loop (ASL) (*109*). Specific modifications within the ASL region of tRNA have been shown to improve aminoacyl-tRNA selection, regulate gene expression, and decrease translational frame-shifting (*93*).

Within the ASL, the majority of nucleoside modifications occur at either position 34 (the wobble position) or position 37 (3’ adjacent to anticodon) (*108*). In many instances modification of the nucleoside involves a single chemical step such as the addition of a methyl or methylthiol group to the base. Alternatively, some modifications employ multiple enzymes within a complex biochemical pathway to produce a hypermodified nucleoside. Scheme I illustrates a particularly interesting hypermodification pathway which occurs at adenine-37 (A_{37}) within the ASL. In facultative anaerobes such as *S. typhimurium*, the extent of A_{37}-modification is believed to regulate aromatic amino acid uptake, enterochelin synthesis, iron transport, and aerobiosis (*107, 108, 110*).

In the first reaction shown in Scheme I, dimethylallyl (Δ^2-isopentyl) diphosphate-tRNA transferase [E.C. 2.5.1.8] (designated MiaA) catalyzes the nucleophilic substitution of the dimethylallyl group from dimethylallyl pyrophosphate (DMAPP) to the exocyclic 6-amino nitrogen of A_{37} (N^6) to yield N^6-isopentenyl-adenosine (i^6A_{37}) with release of inorganic pyrophosphate (*89*). The second enzymatic transformation involves the formal methylthiolation of i^6A_{37} at the C2-position to produce 2-methylthio-N^6-isopentyl-adenosine ($ms^2i^6A_{37}$). The enzyme that catalyzes this remarkable transformation (2-methylthio-N^6-isopentenyl-adenosine synthase, designated MiaB) requires S-adenosylmethionine (*92*) as a co-substrate and is a member of the "radical-SAM" iron-sulfur super family of enzymes (*92, 111*). With the notable exception of $tRNA_{I,V}^{Ser(GGA)}$, nearly all eukaryotic and bacterial tRNAs that read codons starting with U contain the ms^2i^6A-modification (*93, 107*). The final enzyme in this pathway (MiaE, 2-methylthio-N^6-isopentenyl-adenosine(37)-tRNA monooxygenase) catalyzes the O_2-dependent hydroxylation of $ms^2i^6A_{37}$ to produce 2-methylthio-N^6-(4-hydroxyisopentenyl)-adenosine ($ms^2io^6A_{37}$) (*77*). While MiaE can utilize i^6A_{37} as a substrate, whole cell assays suggest a preference for $ms^2i^6A_{37}$ (*94-96*). MiaA and MiaB are common in both eukaryotes and prokaryotes (*82*); however, MiaE is found only within a small subset of facultative anaerobic bacteria such as S*almonella typhimurium, Rhizobium leguminosarum, Corynebacterium fascians,* and *Agrobacterium* *tumefaciens* (*82, 83*). Interestingly, S*almonella typhimurium* mutants lacking MiaE are unable to grow on citric acid cycle intermediates succinate, fumarate, or malate (*112*). These *miaE*$^-$ mutants do not exhibit decreased catalytic activity or expression of citric acid cycle enzymes. Furthermore, their uptake of dicarboxylic acids is also unaffected (*112*). Based on these observations, it has been suggested that S*almonella typhimurium* utilizes the hypermodified ms^{2}io^{6}A$_{37}$ as a signal for the availability of molecular oxygen. Thus, ms^{2}io^{6}A$_{37}$ may serve as a means to help regulate aerobiosis (*93, 95, 113*).

Scheme 2.1 Hypermodification pathway for ms^{2}io^{6}A$_{37}$ (*113*)

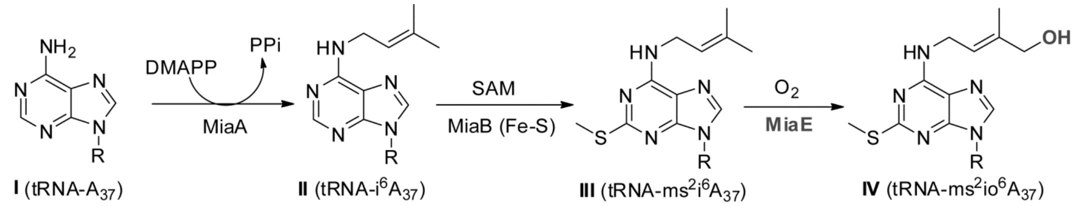

Sequence alignment and spectroscopic characterization (EPR/Mössbauer) of MiaE indicate that it is a member of the non-heme diiron family of enzymes (*77, 83*). Other members of this family include the hydroxylase components of the bacterial multicomponent monooxygenases [methane monooxygenase (MMOH), toluene-monooxygenases (ToMOH)], the small subunit of ribonucleotide reductase (R2), and stearoyl-acyl carrier protein Δ^9-desaturase (Δ9D) (*57, 67, 68*). The study of non-heme enzymes and model complexes has historically attracted considerable interest in the realm of bioinorganic chemistry. This intense focus of research efforts can largely be explained by the vast number of functionally (and structurally) diverse non-heme diiron enzymes identified throughout the biological kingdom and the incredible versatility exhibited in chemical oxidations (mono- and dioxygenations, aliphatic desaturation) they initiate. Remarkably, all of these divergent oxidations are facilitated by minor perturbations to what is essentially a conserved first-coordination sphere to the diiron cluster. The mechanistic paradigm for this class of enzymes starts with the 2 electron reduction of the resting diferric center to produce a diferrous cluster. The diferrous center can then react with molecular oxygen to produce a high-valent oxidizing species capable of substrate oxidation (*77, 97-99*). For example, the hydroxylase component of methane monooxygenase (MMOH) from *Methylococcus capsulatus* (Bath) is one of the most extensively characterized non-heme diiron enzymes (*100-102*). In this enzyme, a high-valent diferryl iron species, termed compound Q, has been identified as the oxidizing intermediate responsible for substrate oxidation (*103, 104*). Alternatively, a diferric peroxo species has been proposed to be the catalytically competent intermediate in the ToMOH-catalyzed oxidation of aromatic hydrocarbons (*105*). As with heme oxidase enzymes, many non-heme diiron enzymes exhibit a ‘peroxide-shunt’ pathway in which the high valent substrate-oxidizing intermediate can be produced by addition of hydrogen peroxide to the resting diferric enzyme. This pathway removes the need for an external electron source, but frequently at the cost of product yield and specificity (*67, 68, 97*).

In this work, three nucleoside substrate surrogates [N^6-isopentenyl-adenosine (i^6A); 2-methylthiol-N^6-isopentenyl-adenosine, (ms^2i^6A); and 2-chloro-N^6-isopentenyl-adenosine, (Cl^2i^6A)] were synthesized such that the chemo and stereospecificity of recombinant MiaE cloned from *Salmonella typhimurium* could be examined. In these assays, the non-heme diiron peroxide-shunt was used in lieu of the native electron-transport chain to perform steady-state kinetic assays (*114*). Both the *(Z)*- and *(E)*-isomers of the hydroxylated products [N^6-(4-hydroxyisopentenyl)-adenoside (io^6A); 2-methylthiol-N^6-(4-hydroxyisopentenyl)-adenoside (ms^2io^6A), 2-chloro-N^6-(4-hydroxyisopentenyl)-adenoside (Cl^2io^6A)] were synthesized for standards in HPLC enzymatic assays and confirmation of MiaE product stereochemistry. Remarkably, for all synthetic nucleosides, MiaE was capable of chemo- and stereoselective *E*-hydroxylation at the terminal C4-position of the isopentenyl-group. Moreover, the results obtained from kinetic experiments suggest that, even in the absence of macromolecular tRNA:MiaE interactions, the C2-position greatly effects the second order reaction rate. Perhaps coincidentally, the observed initial rate is proportional to positive substituent effects at the C2-position (-SMe > -H > -Cl). This observation is consistent with the observation that MiaE preferential hydroxylates ms^2i^6A- over i^6A-tRNA *in vivo* (*95*).

Materials and methods

Cloning. The *miaE* gene was isolated from *Salmonella enterica* strain LT2 genomic DNA [ATCC 700720] using primers purchased from Integrated DNA Technologies (https://www.idtdna.com). A two-step PCR amplification was used to isolate the ORF from genomic DNA and incorporate restriction sites (Sgf I/Pme I) for Flexi-vector cloning (Promega, Madison, WI), followed by insertion of a recognition site for tobacco etch virus protease (TEV). First, (miaE specific) PCR reaction primers: forward 5'- (AAC CTG TAC TTC CAG TCC AAT TAC CCG CAA ATA CTC TCT CCG G)-3'; reverse 5'-(GCT CGA ATT CGT TTA AAC TAT CCG GCG GCT GGC ACG CCG CTA TG)-3'. Second (TEV site insertion) primers: forward: 5'-(GGT TGC GAT CGC CGA AAA CCT GTA CTT CCA GTC C)-3'; reverse: 5'-(GTG TGA GCT CGA ATT CGT TTA AAC)-3'. The DNA produced by this two-step PCR amplification was cloned into an isopropyl β-D-1-thiogalactopyranoside (IPTG) inducible T7 vector (designated pVP80K) obtained from the University of Wisconsin, Center for Eukaryotic Structural Genomics (UW CESG). Sequence verification of *miaE* was performed in the life sciences department at UTA by the Genomics Core Facility (http://gcf.uta.edu/Core_Facility/Core_Facility.html). The resulting plasmid (pMIAE80K) expresses an N-terminal fusion of maltose binding protein (MBP) and MiaE.

The two proteins are separated by a recognition sequence for tobacco etch virus (TEV) protease such that cleavage of the two proteins can be performed following purification. (NOTE: Within the ORF for the miaE gene, two possible start codons are present (*77*). However, only constructs generated from the second start codon resulted in a soluble (29 kDa) protein product.)

For *in vivo* MiaE activity assays, a second '*untagged*' MiaE construct (pMIAEK) was cloned into the commercially available pF1K flexi-vector (Promega). PCR primers: *Sfg I*-forward; 5'-(TTT AAC AGC GAT CGC ATG AAT TAC CCG CAA ATA)-3'; *Pme I*-reverse; 5'-(GTG GTG TTT AAA CTT ATC CGG CGG CTG GCA CGC CGC)-3'. Forward and reverse restriction sites are underlined for clarity. Sequence verification was performed as described above. Expression of soluble protein (29 kDa) was confirmed by SDS PAGE. *NOTE: BL21(DE3) E. coli* cells transformed with the 'untagged' MiaE vector (pMIAEK) have a significantly lower growth rate (~2-fold) in LB-media as compared to cells transformed with the MBP-tagged vector (pMIAE80K). Moreover, cells transformed with pMIAEK showed a significant decrease in cell growth upon induction. This was partly remedied by decreasing the induction temperature from 25 to 17 °C and increasing the time before harvesting cells. We speculate that the N-terminal MBP-tag attenuates promiscuous activity of MiaE within *E. coli* during basal expression. For this reason, the pMIAEK vector was used only for in vivo activity confirmation whereas the pMIAE80K vector was used for over expression, purification, and in vitro enzymatic assays.

Media and growth conditions. The pMIAE80K vector was transformed into chemically competent BL21(DE3) *E. coli* (Novagen) by heat-shock and grown overnight at 37 ^{o}C on a lysogeny broth (LB) (*66*) agar plate in the presence of 25 µg/mL Kanamycin (Kan). The following day, a single colony was selected for growth in liquid LB (Kan) media for training on antibiotic prior to inoculation of 10-L BF-110 fermentor (New Brunswick Scientific) at 37

^oC. Cell growth was followed by optical density at 600 nm (OD_{600}). Induction was initiated by addition of 0.5 mM IPTG, 1 mM ferrous ammonium sulfate, and 20 g casamino acids at an OD_{600} ~4. Additionally, upon induction the temperature of the bioreactor was decreased from 37 ^oC to 25 ^oC and agitation was set to maintain an O_2 concentration of 20% relative to air-saturated media. After 4 hours of induction, the cells were pelleted by centrifugation (Beckman-Coulter Avanti J-E, JA 10.5 rotor) at 18,600 × g for 15 min, and the paste was stored at -80 °C. Confirmation of MiaE expression was performed by SDS-PAGE of lysed cells before and after IPTG induction.

Protein purification. Approximately 25 g of cell paste was suspended in 50 mL of lysis buffer (20 mM HEPES, 40mM NaCl, pH 8.0), and thawed in an ice bath with 10 μg/mL each of lysozyme, deoxyribonuclease I, and ribonuclease with gentle stirring for 30 min. The cell suspension was sonicated in a 30 second on/off pulse cycle for a total of 10 min. The resulting cell free extract was centrifuged (JA 20 rotor) at 48,000 × g for 60 min at 4 ^oC. The supernatant was loaded onto a fast flow DEAE column pre-equilibrated in lysis buffer, and the protein was eluted on a linear NaCl gradient (40 mM to 350 mM NaCl in 20 mM HEPES, 0.3 mM Tris[2-carboxyethyl] phosphine (TCEP), pH 8.0). The fractions containing the MBP-MiaE protein, determined by SDS-PAGE, were concentrated via Amicon N_2 stir cell equipped with an YM 30 ultrafiltration membrane. TEV protease was used to cleave the fusion protein by overnight storage at 4 ^oC. The cleaved fusion protein was desalted by dialysis (Spectra/por, Spectrum Laboratories Inc.) in lysis buffer. To separate MBP from MiaE enzyme, the desalted protein was re-loaded through the DEAE Sepharose column equilibrated in lysis buffer. The protein was eluted on a linear NaCl gradient (0 mM to 350 mM NaCl in 20 mM HEPES, pH 8.0) and fractions containing only MiaE were identified by SDS PAGE and UV-visible spectroscopy. Stoichiometric iron incorporation in purified MiaE was verified by UV-visible spectroscopy on the basis of the

Fe-associated bands typically observed between 320 and 380 nm. Only fractions with A_{280}/A_{370} ~7.8 ± 0.3 were pooled and concentrated (YM 10 ultra-membrane) for use in experiments. For the purified MiaE enzyme, the published extinction coefficient at 280 nm (60,000 M^{-1} cm^{-1}) was used to quantify protein samples (*77*). Within experimental error (5-10%), determination of protein concentration by UV-visible spectroscopy and standard Bio-Rad protein assay (Bio-Rad Laboratories Inc.) were equivalent.

TEV purification and cleavage conditions. The TEV expression vector (pMHTΔ238) was a generous gift from Dr. Russell Wrobel and Professor Brian G. Fox (UW CESG). Expression and cell growth was performed as described for pMIAE80K. Approximately 10 g of TEV cell paste was thawed in 20 mL of IMAC buffer A (20 mM NaH_2PO_4, 500 mM NaCl, 1 mM β-mercaptoethanol, pH 7.5) in an ice bath for 30 min. The suspension containing 10 μg/mL each of lysozyme, deoxyribonuclease I, and ribonuclease was pulse sonicated for 10 min, and centrifuged in a 48,000 × g (JA 20 rotor) for 60 min. The supernatant was collected and loaded onto a 5-mL Hi-Trap immobilized metal affinity chromatography (IMAC) column (GE Healthcare) pre-equilibrated in IMAC buffer A. The column was washed with 5 column volumes (25 mL) of IMAC buffer A prior to elution of TEV enzyme with 2 column volumes of IMAC buffer B (350 mM imidazole in IMAC A, pH 7.5). Excess imidazole was removed by dialysis (Spectra/por, Spectrum Laboratories Inc.) in IMAC buffer A. An Amicon N_2 stir cell equipped with YM-10 ultrafiltration membrane was used to concentrate the TEV protease. Aliquots (1 mL) of TEV were stored at 1 mg/mL in 50% glycerol at -20 ^{o}C. For a typical cleavage reaction, 1 OD_{280} of TEV protease was used per 5 OD_{280} of MBP-MiaE fusion protein.

Iron quantitation. The total iron present in the protein sample was quantitated by using UV-visible spectrophotometer according to published method (*37*). Typically, a 500 μL protein sample was denatured with 250 μl each of hydrochloric acid (2N) and trichloroacetic acid (20%). All iron released from the denatured protein was reduced to ferrous iron by addition of 100 μl hydroxylamine hydrochloride (10% w/v). 200 μl of 2,4,6-tripyridyl-S-triazine (TPTZ) (4 mM) was added as a chromophore along with 100 μl of ammonium acetate solution (50% w/v). A UV-visible spectrophotometer was used to measure the intense color produced by coordination of ferrous iron by TPTZ (ε_{596} = 22,600 $M^{-1}cm^{-1}$). The concentration of adventitious ferric iron (S = 5/2) was determined by X-band (9 GHz) Bruker EPR spectrometer (*74*) by double integration of the observed signal at g = 4.3 ($B_1 \perp B$) and comparison to a known Cu^{II}-standard.

Analytical ultracentrifugation. The native molecular weight, oligomeric state, and sedimentation coefficient of purified MiaE was determined by Virgil Schirf (schirfv@biochem.uthscsa.edu) and Borries Demeler (demeler@biochem.uthscsa.edu) at the UT Health Science Center (San Antonio, TX), Center for Analytical Ultracentrifugation of Macromolecular Assemblies (CAUMA, http://www.cauma.uthscsa.edu/). Three samples (500 μL) of purified MiaE were prepared at 4.7, 9.3, and 15.5 μM within 20 mM HEPES, 100 mM NaCl, pH 8.0 for sedimentation analysis. The monomeric state of MiaE was confirmed by both genetic algorithm and Monte Carlo analysis (*115, 116*).

Calibration of sodium dithionite solutions. All anaerobic samples were prepared in a glove box (Coy Laboratory Products Inc., Grass City, MI) with the O_2 concentration maintained below 1 ppm. Solutions utilized for reductive titration were prepared in the standard MiaE buffer (20 mM HEPES, 40mM NaCl, pH 8.0) degassed on a Schlenk line prior to transferring into the anaerobic chamber. Analytical grade argon was passed through a copper catalyst (Kontes, Vineland, N.J.) to remove trace O_2 impurities and then sparged through distilled water to hydrate the gas. Sodium dithionite is highly sensitive to degradation due to atmospheric moisture and oxygen. Therefore, the amount of '*reducing equivalents*' within each stock solution must be analytically determined by titration with potassium ferricyanide prior to use. The 1-electron reduction of the ferricyanide anion can be followed spectrophotometrically at 420 nm [$\varepsilon_{(420)}$ = 1,050 $M^{-1}cm^{-1}$] as described in *Supporting Information*. Therefore, in reductive titrations the value of '*reducing equivalents*' is reported as opposed to the concentration of sodium dithionite.

Catalase activity. An oxygen electrode was used to measure the rate of oxygen produced upon H_2O_2 addition to enzyme solutions to measure the low-level catalase activity of MiaE (*77, 117*). Dioxygen concentration was determined polarographically using a standard Clark electrode (Hansatech Instruments, Norfolk, England) within a jacketed 2.5-mL cell at 25 ± 2 °C. The electrode was bathed in a saturated solution of KCl and separated from the buffer using a gas-permeable membrane. The electrode was calibrated by measuring the deflection in the voltage upon adding ~500 units of catalase (Sigma-Aldrich, St. Louis) to a buffer with a known concentration of H_2O_2 [$\varepsilon_{(250)}$ = 16.7 M^{-1} cm^{-1}]. Confirmation of initial hydrogen peroxide concentration in buffered solutions was performed using the amplex red hydrogen peroxide/peroxidase kit for spectrophotometric determination (λ = 560 nm) of H_2O_2 (Invitrogen, cat. No. A22188). Once the reaction reached completion, the amplitude for the change in voltage was used to determine a response factor for the electrode. The reaction was initiated by injection of MiaE resulting in final enzyme concentration of 5 μM.

Spectroscopy. All UV-visible measurements were performed on an Agilent 8453 photo diode array spectrometer (Santa Clara, CA). Sample temperature was held constant by a 13 L circulating water bath and a thermostatable cell holder (89054A) with magnetic stirrer.

All measurements were made in ES Quartz cuvettes (NSG Precision Cells, Farmingdale, NY).

X-band (9 GHz) EPR spectra were recorded on a Bruker (Billerica, MA) EMX Plus spectrometer equipped with a bimodal resonator (Bruker model 4116DM). Low-temperature measurements were made using an Oxford ESR900 cryostat and an Oxford ITC 503 temperature controller. A modulation frequency of 100 kHz was used for all EPR spectra. All experimental data used for spin-quantitation were collected under non-saturating conditions.

For simulations of the reduced diiron cluster, it was assumed that the exchange coupling constant (*J*) is comparable in energy to (*or larger*) than the zero-field splitting (*D*) of the diferrous cluster. Under this constraint, the *S* = 4 Hamiltonian takes the form illustrated in Equation 1.

Equation 1 $$\widehat{H} = D\left(\hat{S}_Z^2 - \frac{S(S+1)}{3}\right) + E\left(\hat{S}_X^2 + \hat{S}_Y^2\right) + \beta \mathrm{B} \cdot g \cdot S$$

where *D* and *E* are the axial and rhombic zero-field splitting (*zfs*) parameters and *g* is the *g*-tensor (*118*). EPR spectra were simulated and quantified using Spin Count (ver. 3.1.2), written by Professor M. P. Hendrich at Carnegie Mellon University. The simulations were generated with consideration of all intensity factors, both theoretical and experimental, to allow for determination of species concentration. The only unknown factor relating the spin concentration to signal intensity was an instrumental factor that is specific to the microwave detection system. However, this was determined by the spin standard, Cu(EDTA), prepared from a copper atomic absorption standard solution purchased from Sigma-Aldrich.

Qualitative TLC activity assays. For initial substrate screening, TLC (thin layer chromatography) was utilized to analyze product formation. At selected time points, 10 µL of sample aliquots were removed, heat denatured, and cooled to 0 °C. The reaction mixture (1 µL) was spotted onto a silica gel 60 F_{254} TLC plate (VWR) alongside 5.8 mM of the appropriate standard. After spotting the sample on the TLC plate, a heat-gun was used to completely dry the plate prior to elution. The TLC plate was eluted in 15% methanol in dichloromethane, dried with a heat gun, and stained in potassium permanganate for assay analysis.

In vivo activitiy assay. In a typical experiment, duplicate cultures (1 L each) of *E. coli* BL21(DE3) transformed with the untagged MiaE expression vector (pMIAEK) were grown in LB (25 µg/mL kanamycin) at 37 °C as described above. As a control, a separate culture of *E. coli* BL21(DE3) transformed with the TEV expression vector (pMHTΔ238) was prepared for comparison. Upon reaching OD_{600} ~0.8, one culture was harvested and the cells collected by centrifugation; this 'pre-induction' control sample was prepared for comparison cultures following IPTG-induction. The remaining two cultures transformed with pMIAEK and pMHTΔ238 were induced by addition of 0.5 mM IPTG, 2 g/L casamino acids, 1x Fe-solution (50 µM), and allowed to express for an additional 4 hours at 25 °C prior to harvesting by centrifugation.

Total RNA was recovered by phenol extraction and ethanol precipitation as described previously (*77, 119*). Briefly, RNA was extracted from the cell free extract solution by addition of an equal volume of phenol:chloroform (5:1). Following vortex-mixing, the aqueous phase containing RNA was recovered. This process was repeated 3 times. The pooled aqueous extracts were then mixed with 2.5-volumes of ethanol and stored on ice to precipitate RNA. After 2 hours on ice, the RNA pellet was recovered, dried, and reconstituted in autoclaved MQ H_2O. Since both ms^2i^6A and ms^2io^6A are relatively hydrophobic, LiCl washes were not utilized to fractionate tRNA from rRNA (*120*). From each culture (pre-induced, IPTG induced MiaE, and IPTG induced TEV), samples of total RNA were hydrolyzed by nuclease P1 (Sigma Aldrich, Cat. No. N8630) and then dephosphorylated using bacterial alkaline phosphatase, (Invitrogen, Cat. No. 18011-015) according to published methods (*77, 121*). The resulting samples were analyzed by reverse phase HPLC using the method developed by Gehrke *et al*. (*121*). HPLC instrumentation: Shimadzu quaternary pump LC (LC-20AD XR/LC 30AD) equipped with a diode array photodiode array detector (SPD-M20A); Column, Phenomenex, Gemini-NH 3 μm C18 110 Å; 150 cm × 4.6 mm; Mobile phase, (A) 2.5% methanol in 0.01 M $NH_4H_2PO_4$; pH 5.1, (B) 20% methanol in 0.01 M $NH_4H_2PO_4$; pH 5.3, (C) 35% acetonitrile in 0.01 M $NH_4H_2PO_4$; pH 4.9; Injection volume, 50 μL; Flow rate, 1 mL/min; Column temperature, 25 °C; UV-visible detection wavelength (254 nm).

In vitro HPLC activity assays. Given the decreased number of nucleoside analytes present in peroxide-shunt enzymatic assays, the reverse-phase HPLC method and column was modified from that used in whole cell *in vivo* assays to decrease the retention times (*77, 89, 121*). Therefore, attention was turned towards the use of a hydrophilic interaction liquid chromatography (HILIC) column (AZYP Frulic-N). It was found that with an isocratic elution of 98% acetonitrile and 2% aqueous buffer comprised of 2% triethylamine, 3% acetic acid at a rate of 2 mL/min, the HILIC column gave much shorter retention times, while maintaining baseline separation. Numerous samples were injected without any sign of column degradation or clogging. Substrate retention times ranged from 4 to 6 minutes, while product retention times ranged from 10 to 16 minutes. The reliability of the HILIC column was tested for in vitro assays, giving results within 5% of those obtained by C18 column. Therefore, this method provided equivalent resolution of peaks with a significantly shorter run time.

LC-MS/MS and data analysis. Verification of enzymatic product was performed by multiple reaction monitoring (MRM) using a triple quadrupole LC-MS/MS [Shimadzu Scientific Instruments, LCMS 8040] (*122*). The molecular ions (M^+) of the enzyme substrate (370 m/z) and product (386 m/z) were selected for secondary fragmentation. MRM optimization was then employed to maximize transition intensity and sensitivity for each fragment allowing for quantitation of product ions. The optimized MRM method was used to verify both substrate and product by direct injection of enzymatic assays. These results were compared to direct injection of synthetic standards.

Synthesis of nucleoside analogues. Three ribonucleosides were prepared as shown in Scheme 2.2.

Scheme 2.2 Synthetic route of MiaE analogs.

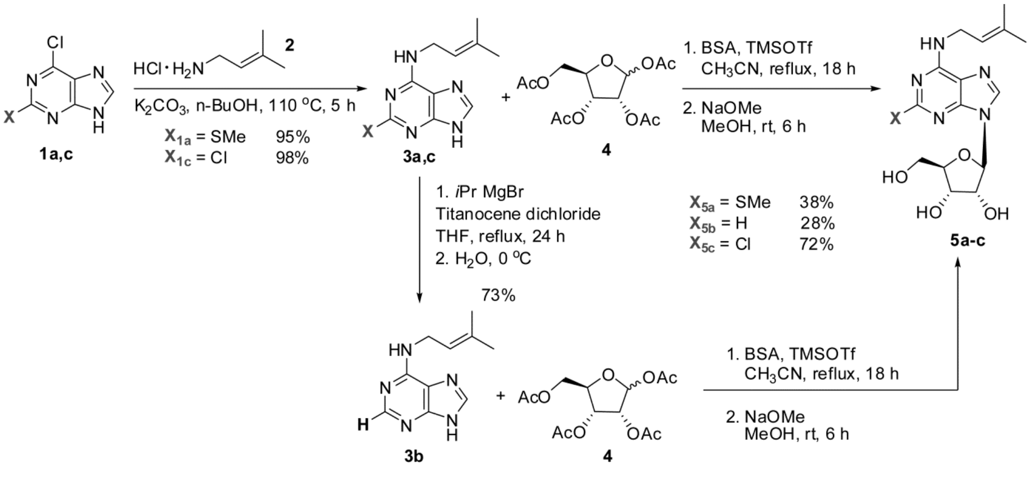

Briefly, 2-methylthio-N^6-isopentenyl-adenosine (5a), $ms^2i^6A_{37}$, was prepared from commercially available thioxanthine. Selective S-methylation of thioxanthine was achieved by adding dimethyl sulfate while maintaining a temperature below 30 °C (*123*). The corresponding product was then chlorinated by addition of phosphorus oxychloride and N,N-dimethylaniline, producing 2-methylthio-N^6-chloropurine (1a) (*123*). Isopentenylamine hydrochloride (2), was synthesized via Gabriel synthesis (*124, 125*), and conveniently isolated as the HCl salt (*126*). Isopentenylamine hydrochloride (2) was added by chemoselective nucleophilic aromatic substitution at the C6-position (*127, 128*). Freshly prepared 1,2,3,5-tetra-O-acetyl-*D*-ribofuranose (4) (*129*) was then coupled to the purine via modified Vorbrüggen coupling (*130, 131*) and subsequently deprotected by saponification to provide the desired product, 5a. Analogues 5b-c were synthesized in a similar manner from commercially available xanthine, which was converted to 2,6-dichloropurine (*132*). 2-chloro-N^6-isopentenyl-purine was accessed by chemoselective nucleophilic aromatic substitution at the C6-position (*133*). N^6-isopentenyl-adenosine (5b) was prepared by utilizing Grignard conditions for hydrodehalogenation at the C2-position (3c to 3b) (*134*).

Hydroxylated 8a-c, expected MiaE oxidation products, were constructed as illustrated in Scheme III, using (*E*)-4-hydroxyisopentenylamine hydrochloride (6) in place of amine 2. *N*-Boc glycine methyl ester (9) could be converted to aldehyde (10) directly by reduction with diisobutylaluminumhydride (DIBAL) or by conversion to *N*-Boc ethanolamine then selective oxidation (not shown) (*135*). Aldehyde 10 was converted to either (*Z*)- (11) or (*E*)-4-amino-2-methylbut-2-enoic acid ethyl ester-4-carboxylic acid-tert-butyl ester (12) by Horner-Wadsworth-Emmons olefination. For clarity, *Z*-stereoisomers in synthetic schemes are designated by a prime (‘). *E*/*Z* selectivity was employed by altering the base from DBU to *n*-BuLi, and adjusting the temperature of the reaction, allowing for the production of the kinetic *Z*-diastereomer in a 4:1 ratio. DIBAL or lithium aluminum hydride treatment reduced the ester to the alcohol, which was then N-Boc deprotection with hydrochloric acid, to afford (*Z*)-(6') or (*E*)-4-hydroxyisopentenylamine hydrochloride (6) respectively (Scheme IV). For further synthetic details, refer to supplemental information.

Scheme 2.3 Synthetic route of MiaE modified analogs.

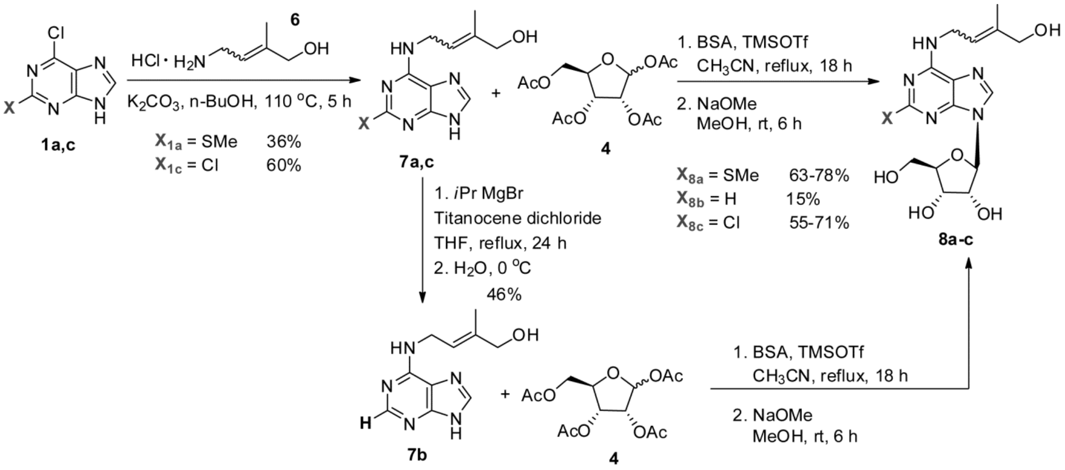

Scheme 2.4 Synthesis of (Z/*E*)-4-amino-2-methylbut-2-en-1-ol hydrochloride (6, 6').

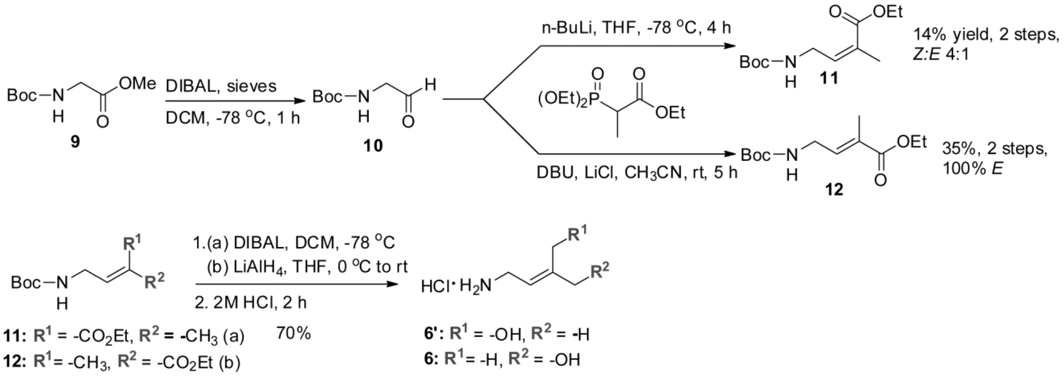

Steady-state kinetic assays. Hydroxylation of substrate surrogates 5a-c by MiaE were assayed utilizing the peroxide-shunt pathway (*97, 98*) frequently observed with heme and non-heme iron oxygenase enzymes. The standard assay conditions included the addition of 25 µL of 400 µM purified MiaE, 25 µL of 23 mM substrate [3:2 DMSO:HEPES buffer (20 mM HEPES, 50 mM sodium chloride buffer, pH 8)], 25 µL of 120 mM hydrogen peroxide in HEPES buffer, and 25 µL HEPES buffer to bring the final volume to 100 µL. The reactions were carried out at 27 °C, and followed for up to one hour. At selected time points, the sample was heat inactivated at 95 °C for 1 minute, and then cooled to 0 °C in an ice bath. The sample was centrifuged at 14,000 rpm for 15 minutes, transferred into a Costar® Spin-X® centrifuge tube filter, and filtered at 11,500 rpm for 3 minutes. For samples analyzed via HILIC (Frulic-N) HPLC method, 100 µL of eluent was added prior to initial centrifugation. Since peak distortion can be caused by variable aqueous content in HILIC separations (*136*), an additional 1300 µL of eluent was added to each sample, resulting in an overall 15-fold dilution in the mobile phase. The results were then analyzed by thin layer chromatography (TLC), HPLC (273 nm), and LC-MS/MS in MRM mode as described previously.

Results

Purification. Recombinant MiaE from *Salmonella typhimurium* was purified and assayed for Fe-content as described in *Materials and Methods*. As indicated by Figure 2.1, the IPTG-inducible MBP-MiaE fusion protein exhibits an apparent molecular weight of ~70 kDa as observed by SDS PAGE. Overnight cleavage with TEV protease resulted in two protein bands ~40 kDa and ~25 kDa, for MBP and MiaE, respectively (Figure 2.1, lane 6). Following buffer exchange by dialysis, MiaE and MBP were easily resolved by a secondary DEAE anion exchange column as shown in (Figure 2.1, lane 7). The molecular weight of MiaE observed by SDS PAGE (~25 kDa) is slightly lower than the value expected based on its amino acid sequence (29 kDa) (*77*). Therefore, both size exclusion chromatography and analytical ultracentrifugation were utilized to confirm that purified MiaE has a monomeric (α) protein configuration in solution. Indeed, in all samples analyzed, no detectable mass action effect were observed and the predicted molecular weight (29,360 Da) was consistent with the monomeric molecular weight of MiaE. These findings were within 1% of the molecular weight calculated from the amino acid sequence (29,013.5 Da) and are consistent with those previously published for this enzyme (*77*).

The stoichiometry of iron per MiaE protein was determined by TPTZ, Bradford assay, and UV-visible spectroscopy as described previously (*37*). In multiple preparations of MiaE, the total iron quantification was measured at 2.1 ± 0.4 iron per MiaE protein. Moreover, the amount of Fe(III) observed by X-band EPR spectroscopy at 10 K (*data not shown*) did not exceed ~6 % of the total iron within the sample; thus adventitious iron does not appear to be present in significant amounts within batches of purified MiaE.

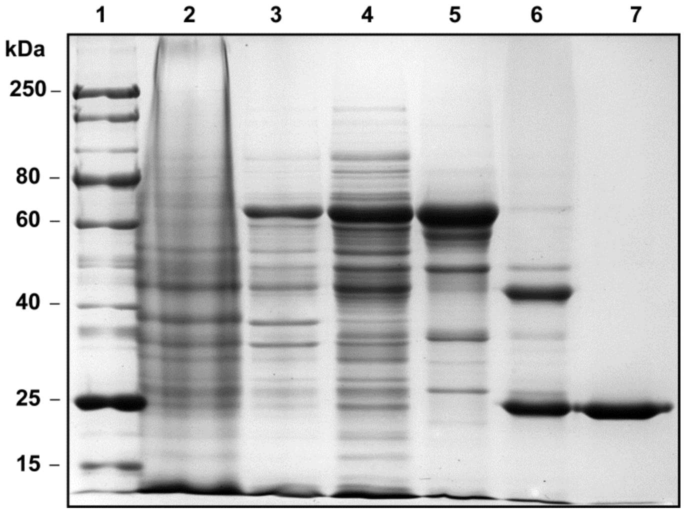

Figure 2.1 SDS PAGE (12 %) of sequential MiaE purification steps. Lane: 1, protein markers; 2, pre-IPTG induced; 3, post-IPTG induced; 4, cell free extract; 5, MBP-MiaE fusion isolated from DEAE AX column A; 6, TEV cleaved fusion protein; 7, isolated MiaE following anion exchange DEAE column B.

UV-visible and EPR spectroscopy. As illustrated in Figure 2.2A, the as-isolated (diferric) MiaE has a yellow color due to its UV-visible absorption features ranging from ~320-400 nm. Such Fe-associated ligand to metal charge transfer bands are typical of non-heme diiron enzyme containing a bridging µ-oxo ligand (*77, 104*). The molar extinction coefficient for this MiaE diferric cluster was determined by two independent methods. First, the absorbance at 370 nm was measured by UV-visible spectroscopy for multiple samples of purified MiaE. Iron content was determined for each sample (*as described above*) and the concentration of diferric sites was taken as half the total ferric iron concentration. On the basis of this analysis, the molar extinction coefficient at 370 nm for the diferric cluster within resting MiaE was determined to be $\varepsilon_{(370)}$ = 4,900 ± 600 M^{-1} cm^{-1} (n = 5 replicates).

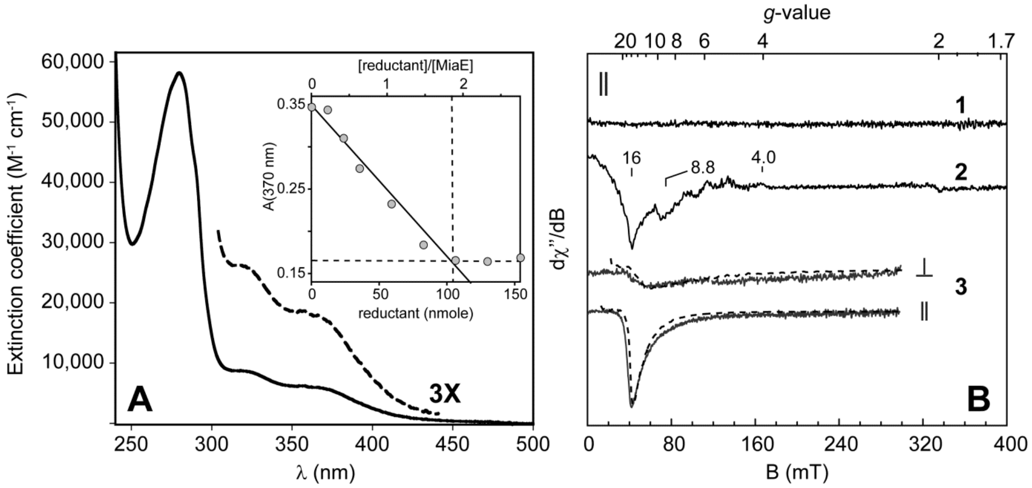

Figure 2.2 UV-visible and EPR spectra of MiaE. A. Optical spectra of as-isolated diferric MiaE (Inset absorbance at 370 nm upon titration with sodium dithionite and catalytic methyl viologen). B. 4.2 K perpendicular (⊥) and parallel mode (‖) X-band EPR spectra of pMIAE80K expression in BL21(DE3) cell suspension (~1 mg/μL). (1) pre-induction (‖); (2) 4-hours IPTG induction (‖); (3) perpendicular and parallel mode X-band EPR of purified MiaE (0.25 mM) chemically reduced with excess sodium dithionite and catalytic methyl viologen.

However, this determination assumes that all optical absorbance at 370 nm is solely attributed to the oxidized enzyme. Moreover, it assumes that all of the iron present in the sample is bound within the active site of MiaE, and thus does not account for the presence of adventitiously bound iron (6% as determined above). Since the absorbance at 370 nm is attributed to diferric cluster within MiaE and not adventitious iron, UV-visible spectroscopy can be used to analytically observe the fraction of oxidized diferric enzyme present during reductive titrations with a calibrated solution of sodium dithionite mediated by methyl viologen. Although, reduced methyl viologen exhibits several absorption features in the visible region, at the concentrations of mediator utilized in these experiments (~0.4 μM) its absorbance (A ~0.005) is negligible and thus can be ignored. Additionally, as shown in *Supporting Information* (Figure S4), due to the proximity of the large protein derived peak at 280 nm, the baseline of the reduced MiaE spectra at 370 nm is non-zero, and thus must be corrected for in the determination of the molar extinction coefficient for the resting enzyme.

In a typical experiment, a stock solution of sodium dithionite was prepared and calibrated by titration with potassium ferricyanide as described in *Materials and Methods* and *Supporting Information*, (Figure S3). Aliquots (~4 μL) of calibrated dithionite solution (5.9 mM reducing equivalents) were added under constant mixing to 1.4 mL of anaerobic MiaE (40 μM) using a 10 μL Hamilton gas-tight syringe. Following each addition of reductant, the UV-visible spectrum was monitored for ~5 min to ensure that reduction had gone to completion prior to adding more dithionite solution. As observed in the inset of Figure 2.2A, addition of sodium dithionite solution results in a steady decrease in the absorbance at 370 nm consistent with reduction of the diferric cluster. From the inflection point at which the absorbance at 370 nm no longer decreases with added reductant, the total concentration of MiaE diferric clusters can be obtained. For clarity, this inflection point is designated by the crossing of the dashed lines within the inset of Figure 2.2A.

Based on the assumption that 2 reducing equivalents are required for each diiferric cluster, the molar extinction coefficient at 370 nm can be determined for the oxidized enzyme from the difference in the absorbance observed between the oxidized and reduced MiaE (A ~ 0.188 AU) and dividing this value by half the moles of reductant added (53 nmol) [$\varepsilon_{(370)}$ = 4,970 M^{-1} cm^{-1}]. The average value obtained over (n = 3) replicate measurements was $\varepsilon_{(370)}$ = 5,100 ± 700 M^{-1} (mean ± std.dev.). From the reducing equivalents added and the protein content within the each sample, an average stoichiometry of 1.9 ± 0.1 moles of Fe are observed per MiaE protein. This value is quite similar to reported ε-values for other non-heme diiron enzymes exhibiting a bridging μ-oxo ligand (*137-139*).

Of particular note, the intensity of the 370 nm Fe-associated features demonstrates a clear pH dependence within the range of 7.5 to 8.5. As illustrated in *Supporting Information* (Figure S5), at fixed protein concentration, the relative absorbance at 370 nm shows a maximal value at pH ~ 8.4 (~35% higher as compared to pH 7.6) and an apparent midpoint at pH ~ 8.1. Similar behavior has been reported for non-heme diiron enzymes where the μ-oxo bridging ligand separating the diiron cluster is in equilibrium with the protonated μ-hydroxo species (*77, 140, 141*). As enzymes containing a μ-hydroxy bridged diiron cluster typically lack Fe-associated absorption features (*142*), the molar extinction coefficient constant determined above is likely underestimated. Therefore, additional experiments involving Mössbauer spectroscopy are necessary to more accurately refine these measurements.

In parallel mode X-band EPR spectroscopy, many non-heme diiron enzymes exhibit a low field signal with a distinct valley at *g* ~ 16 in the fully reduced, diferrous oxidation state (*75, 143-145*). Among non-heme diiron enzymes, this feature is attributed to the weak ferromagnetic exchange coupling between two high-spin ferrous sites ($S_1 = S_2 = 2$), resulting in a ground state $S = 4$ spin-manifold. In non-heme diiron model complexes and bacterial multicomponent monoxygenases (MMOH and T4MOH), the observed *g* ~ 16 signal can be remarkably intense and observed at very low concentrations (≥ 30 μM at 4K). This is also the case for reduced MiaE. As illustrated in Figure 2B, a *g* ~ 16 signal (spectra 2) can be observed within a suspension of BL21(DE3) *E. coli* cells following 4 hour IPTG-induction. In these experiments, samples were prepared by adding ~0.3 g cell paste in 0.3 mL 50 mM potassium phosphate, 20% glycerol, pH 7. The suspension was then transferred to an EPR tube and frozen in liquid N_2. The additional signal observed at *g* ~ 8.8 is consistent with high-spin ferrous iron (*75*). For comparison, the parallel mode EPR spectra of BL21(DE3) *E. coli* cells prior to induction and the purified fully reduced MiaE are shown in spectra 1 and 3, respectively. The temperature dependence of the MiaE *g* ~ 16 signal deviates from Curie law behavior in that the temperature-normalized signal intensity (S×T) decreases with increasing temperature. Maximal intensity for this signal is observed at 4.2 K and completely vanishes by 25 K (*data not shown*). Therefore, this transition must originate from a ground doublet within the lowest-lying spin-manifold of a non-Kramers system. The EPR resonance condition for a non-Kramer's doublet is given by $(h\nu)^2 = \Delta^2 + (\tilde{g}\beta B)^2$, where Δ represents the zero-field splitting separating the quasi-degenerate EPR active doublet and $\tilde{g}$ is the angle dependent effective *g*-value (*143, 146*).

Provided $\Delta < 0.3$ cm^{-1} (X-band $h\nu$ ~ 0.3 cm^{-1}), simulations of the reduced diiron cluster can be generated with the assumption that ferromagnetic exchange coupling constant (*J*) is comparable or larger in magnitude than the zero field splitting term (*D)* (i.e. $|J| \geq D$). Under such constraints, the *S* = 4 spin-Hamiltonian (Equation 1) can be utilized to calculate correct EPR transition probabilities, and thus sample concentrations can be calculated (*141, 143, 146*). Comparison of the simulated diferrous site concentration to the expected value determined by UV-visible spectroscopy can then be used as an additional means to validate EPR spectroscopic simulations. Using this procedure, X-band EPR spectral simulations (*dashed lines*) were calculated for both perpendicular and parallel mode and overlaid on the observed spectra. As observed in Figure 2.2B (spectra 3), both X-band perpendicular and parallel mode EPR spectra can be simulated for D = 1.0 cm^{-1}, E/D = 0.087, and $g_x = g_y = g_z = 2.0$. Distribution in the value of E/D ($\sigma_{E/D}$ = 0.05) provides good agreement to spectral data in both field polarization modes. The spin concentration determined from EPR simulations [S] = 108 μM (43% of theoretical value). The observed deviation between the concentration theoretically calculated by EPR spectroscopic simulation and that expected on the basis of UV-visible spectroscopy suggests that the simplified assumptions made in simulations of the reduced diiron center may not be fully justified. The fact that the g ~ 16 signal can be observed during *in vivo* expression demonstrates that a significant fraction of expressed MiaE is reduced at physiologically relevant potentials. Collectively, the observed Fe-stoichiometry [2 Fe per MiaE α-monomer], Fe-associated LMCT bands for the diferric enzyme, and the parallel mode g ~ 16 EPR signal for the fully reduced MiaE clearly demonstrates the integrity of the non-heme diiron site within the recombinantly expressed MiaE.

In vivo MiaE activity. The activity of recombinant MiaE was confirmed in whole cell assays following a similar protocol as described previously (*77, 112*). In these experiments, *E. coli* BL21(DE3) was transformed with either the '*untagged MiaE*' or TEV vector (pMIAEK and pMHTΔ238, respectively) for comparison of total nucleoside extracts. Samples were prepared as described in *Materials and Methods*. Both pMIAEK (*untagged MiaE*) and pMHTΔ238 (TEV) vectors have the same Promega flexi-vector backbone and antibiotic resistance, therefore RNA extracts isolated from cells transformed with pMHTΔ238 offer a reasonable baseline for nucleoside distribution in the absence of MiaE. The chromatograms shown in Figure 2.3 represents the nucleosides obtained from *E.coli* post-IPTG induction (4-hours) of TEV (A) and untagged MiaE (B).

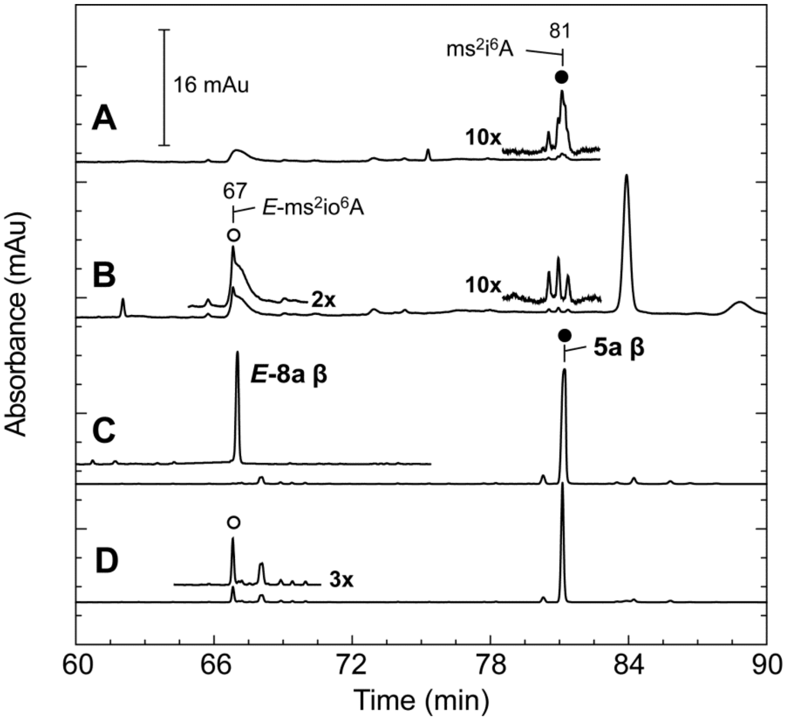

Figure 2.3 *In vivo* assay of MiaE. Reverse phase C18 HPLC chromatogram of hydrolyzed tRNA nucleosides extracted from IPTG-induced *E.coli* BL21(DE3) transformed with (A) pMHTΔ238 and (B) pMIAEK. Assignment of (*E)*-ms^{2}io^{6}A (67 min) and ms^{2}i^{6}A (81 min) β-epimers were confirmed by comparison of retention times and UV-visible spectra to synthetic standards (C). For clarity, a selected time point (30 min) is shown in trace D for the MiaE peroxide-shunt catalyzed hydroxylation of 5a.

Of particular note are the peaks observed at 67 and 81 minutes designated by (○ and ●, respectively). The peak at 81 minutes (●) is observed in all nucleoside samples collected for pre- and post-IPTG induction of pMIAEK, as well as cells transformed with pMHTΔ238. On the basis of its retention time, UV-visible spectra, and coelution with synthetic standards (trace C; 5a, β-epimer), this peak is assigned to ms^2i^6A. Alternatively, the 67 min. peak (○) is only observed following IPTG-induction of pMIAEK, and coelutes with *E*-8a, β-epimer. On the basis of these experiments, it is clear that recombinant MiaE is catalytically active in whole cells. Moreover, as illustrated in Figure 2.3 (trace D), the 5a-hydroxylated product generated by MiaE peroxide-shunt nicely overlaps with the *E*-ms^2io^6A-product observed in whole cell assays. Thus, the native stereoselectivity of MiaE appears unperturbed in peroxide-shunt assays.

Catalase activity. Many non-heme diiron oxygenase enzymes exhibit limited catalase activity as a result of the peroxide-shunt pathway (*117*). While this activity is several orders of magnitude less than that of a 'true' catalase enzyme, this assay can be diagnostic of the specific activity of purified MiaE in the absence of the native ($ms^2i^6A_{37}$) substrate. In these experiments, a standard Clarke-type oxygen electrode was used to monitor the amount and initial rate of O_2-evolved upon addition of as-isolated MiaE to a buffered solution (20 mM HEPES, 100 mM NaCl, and pH 8) containing hydrogen peroxide. The volume of each reaction was fixed at 1.5 mL with a final MiaE Fe_2-site concentration of 5 μM. For analysis, initial rates were normalized for enzyme concentration (v_0/[E]) and H_2O_2 concentrations were varied between 15 and 80 μM at 25 °C. As shown in *Supporting Information* (Figure S6), full enzymatic saturation kinetics was not observed within the range of H_2O_2 utilized (0-80 μM). However, from the linear portion of the curve, the pseudo-second order rate constant was determined ($k_{obs} \sim 1{,}480\ M^{-1}\cdot s^{-1}$). The stoichiometry of H_2O_2 consumed per O_2 generated was determined by addition of (120 μM) H_2O_2 to a buffered solution containing 10 μM MiaE. Upon completion of the reaction (2 min), the O_2 concentration within the solution increased by 62 μM. In multiple replicates, formation of 1.1 ± 0.2 (n = 5) mol of O_2 is observed upon addition of 2 mol H_2O_2.

Hydroxylation of substrate-surrogates by peroxide shunt. Non-heme diiron monooxygenases often exhibit a peroxide shunt pathway, which can be exploited to bypass the native electron transport chain necessary for *in vivo* catalysis. For initial screening of synthetic substrate-surrogates, TLC was used to qualitatively observe the formation of hydroxylated products and decay of the starting material. Using this method, preliminary assays were performed to determine if the $ms^2i^6A_{37}$ substrate-analogues [isopentenylamine hydrochloride (2), 2-chloro-N^6-isopentenyl-purine (3c), 2-chloro-N^6-isopentenyl-adenosine (5c)] were hydroxylated by MiaE in the presence of hydrogen peroxide (20 mM). As a control, duplicate samples were prepared in the absence of MiaE to verify that the observed products were not the result of direct oxidation by H_2O_2. An additional control sample was prepared using heat-denatued MiaE. In these preliminary assays, complex 2 showed no obvious sign of decay with MiaE over the course of the experiment (1 hour), and the limited solubility of complex 3c made analysis impossible. However, complex 5c showed an obvious decay with time and concomitant formation of a new spot (*Supplementary Information*, Figure S1). Moreover, the R_f-value (0.18) for this new spot correlates with that of the synthesized 2-chloro-N^6-((*E*)-4-hydroxyisopentenyl)-adenosine (8c). Preparatory TLC and high resolution mass spectral analysis indicated a mass equivalent to expected product [HRMS (EI) found 386.1231 *m/z*; calculated 386.1153 Da]. No products were observed in control samples within the time scale of these reactions.

To confirm that the MiaE hydroxylated product corresponds to the synthetic (8c) product, spike assays were performed in which the synthetic product was added into samples taken from the *in vitro* MiaE assay. As with the experiments described above, control experiments performed in the absence of MiaE or utilizing heat-denatured MiaE showed no detectable peaks corresponding to 8c formation. Figure 2.4A (*bottom,* ●) shows a representative chromatogram obtained from the MiaE assay. The larger peak observed at a retention time of 4.32 min corresponds to the enantiomerically pure β-substrate (5c) whereas the MiaE hydroxylated product is observed at 9.70 minutes. For clarity, these peaks are designated I and II, respectively.

The two remaining chromatograms in Figure 2.4A represent the same MiaE assay sample in which a diasteriomeric mixture of α/β *E*-8c (*middle,* ▲) and *Z*-8c (*top,* ■) was added to the sample. In addition to the peak corresponding to substrate (5c), two additional peaks are observed in the middle (▲) chromatogram at 9.70 and 11.69 min corresponding to the β- and α-diasteriomers of *E*-8c, respectively. The peak corresponding to the β-epimer of the synthetic *E*-8c is designated by III. For comparison, addition of the diasteriomeric mixture of *Z*-8c (α-epimer, 10.16; and β-epimer, 8.64 minutes) is shown in the top (■) chromatogram of Figure 2.4A. Given that an enantiomerically pure substrate was utilized in enzymatic reactions, the observed increase in peak area of the *E*-8c β-enantiomer with spike addition, along with the overlapping retention time (*dashed line*), strongly supports assignment of the MiaE product (β-8c) and *E*-stereochemistry. Representative chromatograms of product standards *E*-8c and *Z*-8c, along with selected enzymatic assays utilizing substrate 5c, are provided in *Supporting Information*, Figure S2. For all substrates assayed (5a-c), no more than 3% of the hydroxylated *Z*-product was ever observed within the time scale of peroxide-shunt assays.

As final verification of *MiaE* hydroxylated product, LC-MS/MS was performed on the peaks designated I, II, and III using MRM transitions of respective product ions as described in *Materials and Methods*. The top panel (I) Figure 2.4B represents the substrate 5c mass spectrum (370 m/z molecular ion), whereas the middle and bottom panels represents the mass spectrum obtained from the enzymatic product (II) and synthetic *E*-8c standard (III), respectively. The molecular ion (M^+) is observed in each, with an increase of 16 (hydroxyl ion) in both the enzymatic product (II) and product standard (III) [$M^+ = 386.1$ m/z]. The m/z 238 of 5c, along with the m/z 254 of enzymatic product and *E*-8c is the result of the ribose cleavage and thus also exhibit an increase in mass by 16 m/z consistent with hydroxylation. The m/z 170 fragment is a result of isopentenyl cleavage, followed by m/z 134 representing a loss of HCl. In light of the matching fragmentation patterns and relative intensities obtained for MiaE product (II) and the synthetic product standard *E*-8c (III), the increase in molecular ion by 16 m/z, and overlapping retention times obtained in spike assays described above, it appears that the MiaE hydroxylated product generated by peroxide shunt assays can be attributed to *E*-Cl^2io^6A.

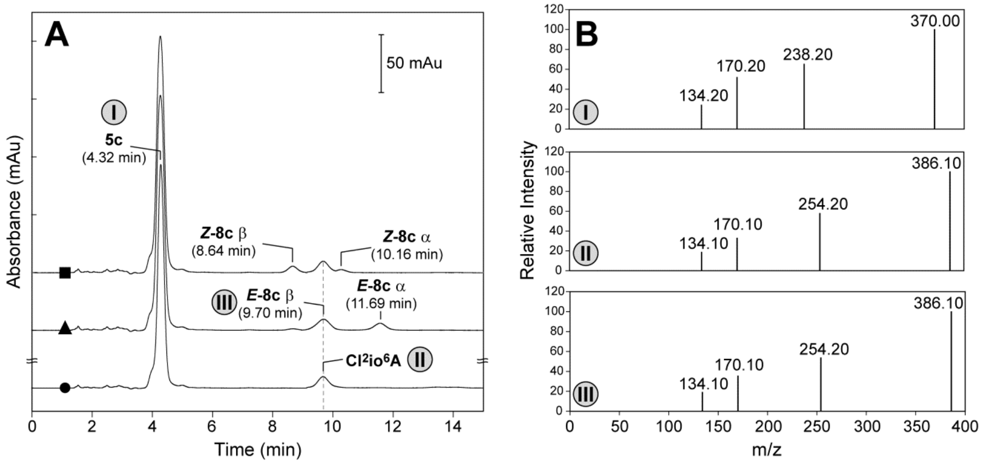

Figure 2.4 HPLC and MS analysis of *in vitro* assay. (A) HILIC chromatogram of product formation. (B) LC-MS/MS spectra of MRM transitions of designated product ions.

Optimal concentration of H_2O_2 for MiaE peroxide-shunt assays was determined by the method of isolation. In these experiments, the concentration of substrate 5c was fixed (5.8 mM) while H_2O_2 concentrations were varied from 5 to 50 mM. The reaction was initiated by addition of 100 μM MiaE (Fe_2-sites) at 27 °C. At selected time points (1-9 min), sample aliquots were removed for heat inactivation (95 °C for 1 minute) and spin-filtered to remove denatured protein as described in *Materials and Methods*. Figure 2.5 shows the initial rate (v_0/[E]) of product (Cl^2io^6A) produced as a function of initial hydrogen peroxide concentration. As with the catalase assays (*Supporting Information*, Figure S6), full saturation of MiaE is never observed within the concentration range utilized for these experiments (1-50 mM). Since visible signs of protein denaturation were observed at H_2O_2 concentrations ~40 mM, the decrease in v_0/[E] observed is likely due to enzymatic degradation and not substrate saturation. Therefore, 30 mM H_2O_2 was used for subsequent assays.

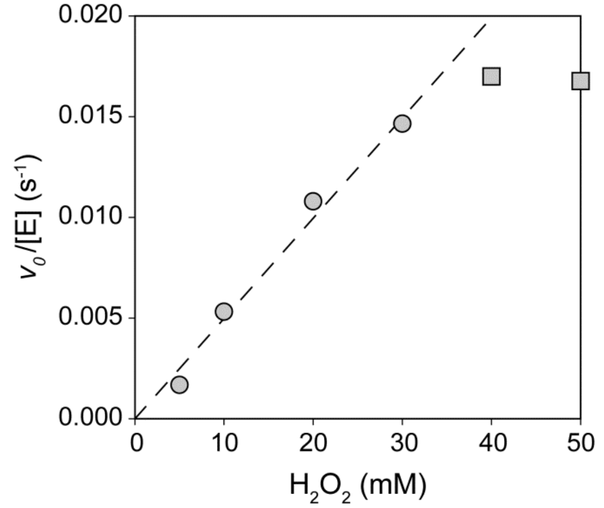

Figure 2.5 Rate of product formation. Enzyme normalized initial rate (v_0/[E]) of product formation (Cl^2io^6A) with increasing H_2O_2 concentration.

As illustrated in Figure 2.6, the rate of substrate (5c) degradation (●) at 30 mM H_2O_2 is kinetically matched to the rate of product (Cl^2io^6A) formation (■). Moreover, in the absence of MiaE (Figure 2.6, ◊), no decay of 5c (or formation of Cl^2io^6A) can be observed within the time scale of these experiments. This observation indicates that H_2O_2 cannot (by itself) specifically oxidize the substrate and that product decay and substrate formation are coupled (1:1 stoichiometry) within the MiaE peroxide-shunt assay. By contrast, given the low-level catalase activity of MiaE it is unlikely that the stoichiometry of H_2O_2 consumed per mol of product is closely matched.

Substrate-Analogue Study. MiaE specificity for synthetic substrate-analogues (5a-c) was determined using the method of isolation as described above. However, in these experiments the hydrogen peroxide concentration was fixed at 30 mM while varying the concentration of nucleosides (5a-c). Given the low solubility of synthetic nucleosides (5b in particular), dimethyl sulfoxide (DMSO) was added to the enzymatic reactions to increase the upper limit of substrate concentration. Control reactions containing up to 20% (v/v) DMSO showed no effect on the rate of Cl^2io^6A formation by MiaE peroxide shunt. Only at DMSO concentrations exceeding 25% (v/v) was a noticeable decrease observed in the rate of peroxide-shunt product hydrolysis. Therefore, all of the enzymatic assays described below were carried out in the standard HEPES buffer with 20% DMSO (v/v).

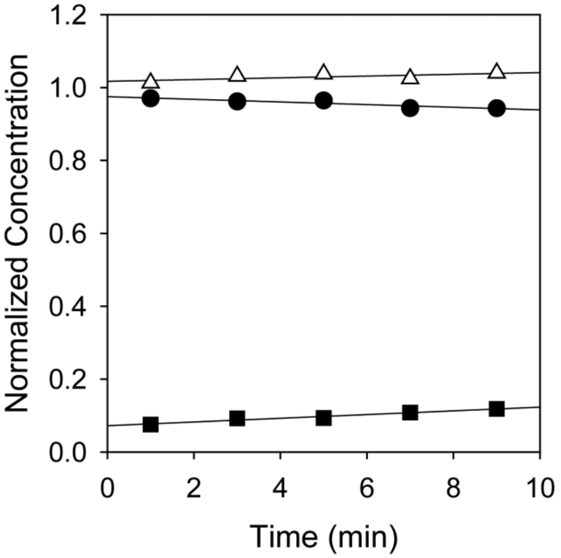

Figure 2.6 Stoichiometry of loss of reactant vs product formation. Stoichiometric coupling of 5c decay (●) and Cl^2io^6A formation (■) in Mia peroxide shunt pathway. Within error, the rate of substrate decay and product formation is kinetically matched (0.01 min^{-1}).

For each assay, the concentration of substrate analogue was varied from 0.5-4 mM (depending on solubility) at fixed H_2O_2 concentration (30 mM). As previously stated, reactions were initiated by addition of 100 μM MiaE (Fe_2-sites) at 27 °C and sample aliquots were taken at times ranging from 1-9 minutes. HPLC sample preparation was carried out as described previously. Figure 2.7 shows the initial rate of product formation (ms^2io^6A, io^6A, and Cl^2io^6A) plotted against the starting concentration of each substrate (5a-c) analogue. Each substrate saturation kinetic experiments were performed in duplicate. For clarity, only the error observed in the initial rate of 8c formation is indicted in Figure 2.7.

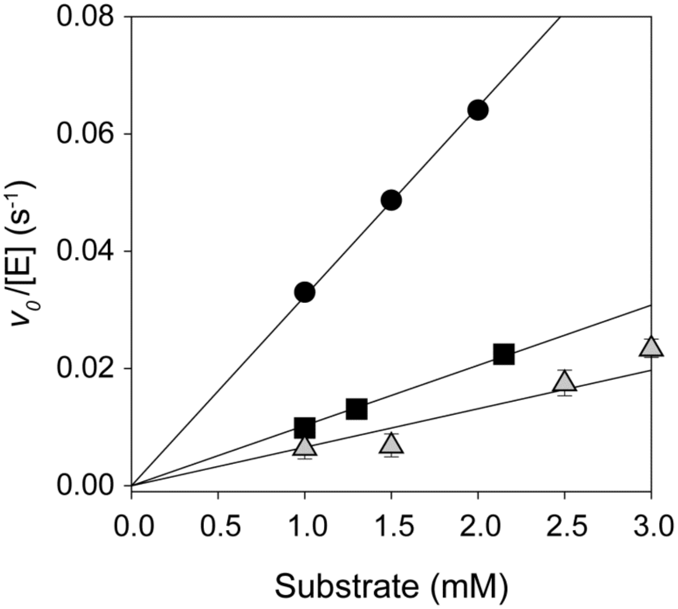

Figure 2.7 Rate of substrate-analogue hydroxylation. Rate of substrate-analogue (5a-c) hydroxylation by MiaE peroxide shunt Enzyme normalized initial rate (v_0/[E]) of product (ms^2io^6A, io^6A, and Cl^2io^6A) formation with increasing substrate concentration [5a (●, -SMe), 5b (■,-H), and 5c (Δ,-Cl)] .

As expected, the initial rate of product formation increases to a maximal value with increasing substrate concentration. However, at elevated concentrations, the rate of product formation decreases significantly for each nucleoside suggesting something analogous to substrate-inhibition or decreased enzyme activity near the solubility limit of the synthetic nucleosides (5a-c). Given the complexity of this system, development of a full kinetic model is complicated and prone to over-interpretation. However, as with H_2O_2 saturation experiments, comparison of initial rates within the linear range (1-3 mM) can be made. Shown in Figure 2.7 is a plot of the initial rate of product formation (8a-c) versus substrate concentration. As in H_2O_2-saturation experiments (Figure 2.5), all initial rates are normalized for enzyme concentration (v_0/[E]). At fixed H_2O_2 concentration (30 mM), the slope of the line can be interpreted as the pseudo-second order rate constant (approximately k_{cat}/K_m). On the basis of this interpretation, the rate of MiaE catalyzed H_2O_2-shunt hydroxylation for 5a (2-SMe), 5b (2-H), and 5c (2-Cl) can be estimated as 32.3, 10.3, and 6.6 $M^{-1} \cdot s^{-1}$, respectively.

Discussion

Nucleoside substrate synthesis. A divergent synthetic strategy led to the preparation of three nucleoside mimics with varied functionalization at the C2-position, 2-SMe (ms^2i^6A), 2-H (i^6A), and 2-Cl (Cl^2i^6A). Additionally, two diastereomers of each expected oxidized product were prepared, giving rise to six additional nucleosides (*E*/*Z*)-ms^2io^6A, (*E*/*Z*)-io^6A, and (*E*/*Z*)-Cl^2io^6A). The Vorbrüggen coupling of the purine derivatives to tetraacetylribose provided a metal-free preparation, and resulted in comparable yields (*147-149*). The nucleosides were synthesized in eleven or fewer steps from commercially available materials and with 10-15% overall yield. As discussed below, the synthesis of these nucleosides allowed for the stereochemical determination of the MiaE modified product (*E*-ms^2io^6A), along with the overall effect of the C2-functionalization on rate of product formation.

Characteristics of S. typhimurium MiaE. In general, the physical properties of MiaE are consistent with those for other members of the non-heme diiron class of metalloenzymes. The optical features in the 320-380 nm range [5,100 ± 700 M^{-1} cm^{-1}] observed for resting MiaE are reminiscent of those observed for the μ-oxo bridged diiron clusters within other non-heme diiron metalloproteins such as the small subunit of ribonucleotide reductase (R2) [$\varepsilon_{(370)}$ = 4,350 M^{-1} cm^{-1}] (*109, 150*), stearoyl-acyl carrier protein Δ^9-desaturase (Δ9D) [$\varepsilon_{(340)}$ = 4,200 M^{-1} cm^{-1}] (*151*), myohemerythrin (Hr) [$\varepsilon_{(330)}$ = 6,500 M^{-1} cm^{-1}] (*152*), and phenol hydroxylase (DpmLNO) [$\varepsilon_{(350)}$ = 4,800 - 6,000 M^{-1} cm^{-1}] (*141*). By contrast, the oxidized diiron cluster within the hydroxylase components of bacterial methane and toluene monooxygenases (MMOH and T4MOH) are believed to have a hydroxo-bridged diiron clusters and thus lack such optical features as a consequence (*153*).

The dual mode EPR spectroscopy of reduced MiaE exhibits similar temperature-dependent signal intensity, linewidth, and *g*-values as compared to the reduced diiron sites within several other bacterial non-heme monoxogenase enzymes (DpmLNO, T4MOH, MMOH) (*142*). As previously mentioned, spin quantitation of reduced MiaE by simulation only accounts for [0.11 mM] 44% of the total iron within the sample. This may indicate that the assumptions made in simulating the reduced diiron cluster ($|J| \geq D$) were not fully justified. However, previous Mössbauer analysis of oxidized MiaE suggests the presence of a major (54%) μ-hydroxo bridged [δ = 0.49 mm·s^{-1} ΔE_Q = 0.51 mm·s^{-1}] and minor μ-oxo bridged [δ = 0.52 mm·s^{-1} ΔE_Q = 1.49 mm·s^{-1}] population within the as-isolated MiaE (*77*). Indeed, similar (μ-oxo/μ-hydroxo) speciation has been reported from Mössbauer analysis of as-isolated and reduced Δ9D (*140*), T4MOH (*142*), and DpmLNO (*141*). In the case of reduced DpmLNO, this same (μ-oxo/μ-hydroxo) speciation could be observed upon reduction of the resting diferric enzyme. Moreover, it was reported that only the μ-hydroxo bridged diferrous cluster was EPR active (*141*). Therefore, the low spin-quantitation [44% relative to the total iron] determined by EPR simulations could also be explained if reduced MiaE exhibits similar (μ-oxo/μ-hydroxo) speciation as previously reported for the oxidized enzyme and that only the μ-hydroxo fraction is EPR active. Under these assumptions, the concentration of μ-hydroxo bridged fraction is within 10% of the simulated spin-quantitation. Given the observed pH dependence of the Fe-associated bands, it is clear that some (μ-oxo/μ-hydroxo) speciation is present in resting MiaE. However, it is not known if this speciation remains upon reduction of the diiron center. This observation also implies that the extinction coefficient determined here for the resting diferric enzyme is likely underestimated. Investigation of the oxidized and reduced MiaE by Mössbauer spectroscopy is currently in progress to validate EPR spectroscopic simulations and refine UV-visible molar extinction coefficient determinations for this enzyme.

The monomeric (α) configuration of MiaE reported here is in agreement with previous reports (*77*). This trait is quite unusual for non-heme diiron enzymes and, to our knowledge, has only been reported for the non-enzymatic member of this family, hemerythrin (Hr) (*152, 154, 155*). Typically, the quaternary structures of non-heme diiron enzymes are multimeric in their native form (*156*). In fact, the most common quaternary structure observed for this family of enzymes is homodimeric (α_2). Whereas, the most common structural motif observed among the hydroxylase components within the BMM class of non-heme diiron monooxygenases is a heterotrimeric dimer ($(\alpha\beta\gamma)_2$) configuration (*66*). Interestingly, both R2 and Δ9D have been reported to exhibit 'half-sites' reactivity, implying that the two protomers of these (α_2)-enzymes do not act independently during catalysis (*69, 71, 72, 157*). Historically, both the structural complexity and the potential for '*half-sites*' reactivity within this class of enzymes have significantly complicated the spectroscopic and mechanistic characterization of non-heme diiron enzymes. Therefore the monomeric (α) protein configuration of MiaE represents a minimalist enzymatic structure which could potentially provide a unique point of comparison to other enzymes within this class.

MiaE substrate specificity influenced by C2-position substitution of nucleoside. Initial attempts to demonstrate MiaE hydroxylation of the free purine (substrates 3a-c) were not successful given the insolubility of the base in the absence of ribose. Interestingly, within error both α- and β-epimers (5a-c) were hydroxylated at comparable rates (Table S1). This observation indicates that the ribose ring does not represent a significant enzyme-substrate point of interaction. Furthermore, since the C2-position of the nucleoside is quite distant from the point of enzymatic hydroxylation, given the observed difference in the second order reaction rate [5a (2-SMe) > 5b (2-H) > 5c (2-Cl)], it is reasonable to speculate that the nucleosides C2-substituent significantly influences the MiaE-binding affinity. For example, at a fixed substrate concentration (2.0 mM), the rate of 5a-hydroxylation is over three-fold that of 5b-hydroxylation. Interestingly, a similar substrate preference has also been observed for ms^2i^6A- and i^6A-bearing tRNA substrates (*112*). Therefore it is possible that the enzymatic substrate specificity is largely a function of the nucleoside base and not due to conformational difference within the global tRNA tertiary structure.

(E/Z)-stereochemistry of MiaE hydroxylated products (io^6A, Cl^2io^6A, and ms^2io^6A). The peroxide-shunt pathway is a common feature among non-heme diiron (and heme) oxygenase enzymes (*97, 98, 119, 141*). The use of a peroxide-shunt simplifies the enzymatic catalysis by removing the need for an enzymatic electron-transfer pathway. However, peroxide-shunt enzymatic activities are significantly lower than native catalysis due to the competing catalase-activity, and the potential for promiscuous Fenton-type

reactions leading to enzymatic degradation. Therefore, peroxide-shunt experiments should be considered diagnostic of native MiaE catalysis, but are less useful for the development of a kinetic mechanism. Additionally, relative to reactions catalyzed in the presence of their electron-transfer chain, many non-heme oxygenases exhibit decreased stereo- and chemioselectivity by peroxide-shunt (*67, 97, 98*). For instance, it was found that, in the presence of protein B, MMOH demonstrates a 3-fold greater selectivity in the presence of dioxygen relative to peroxide-shunt induction (*67*). By contrast, MiaE peroxide-shunt demonstrates a clear stereospecificity in that only the (*E*)-isomer of the hydroxylated nucleosides (8a-c) are observed. Indeed, for all substrate analyses, < 3% of the (*Z*)-isomer was ever identified in peroxide-shunt reactions. Moreover, as illustrated in Figure 3, *in vivo* product formation during MiaE IPTG-induction is also consistent with the (*E*)-isomer of ms^2io^6A. Thus the peroxide-shunt MiaE product is consistent with native catalysis. This result was not readily anticipated given discrepancies within the literature regarding the stereochemistry of $ms^2io^6A_{37}$ isolated across phylogenic domains. For example, early on it was reported that $ms^2io^6A_{37}$ isolated from plants exhibited (*Z)*-stereochemistry. Interestingly, in this same report it was observed that the (*E)*-isomer of io^6A_{37} could be isolated as a free-base (*153*). Thus, suggesting the possibility of an independent pathway for cytokinin synthesis independent of MiaE. Alternatively, this observation may simply be the result of light induced *E*/*Z*-isomeriztion. Regardless, this hypothesis was never explored further. Among bacterial enzymes, it was reported that *Z*-$ms^2io^6A_{37}$ was the MiaE-product observed from various plant-associated bacteria (*Rhizobium leguminosarum*, *Agrobacterium tumefaciens*, and *Corynebacterium fascians*) (*158*). The first instance of *E*-$ms^2io^6A_{37}$ was reported by Ajitkumar and Cherayil for the non-plant associated *γ-proteobacteria, Azotobacter vinelandii* (*82*). Based on this observation it was proposed that other non-plant associated bacteria (such as *Salmonella* *typhimurium*) may also produce the (*E*) - instead *of the* (*Z*)-isomer. This is perhaps a tenuous hypothesis given only 58% identity between *S. typhimurium* and *A. vinelandii* MiaE*.* To our knowledge, this work represents the first direct confirmation of the *S. typhimurium* MiaE stereospecificity.

Chapter 3

Steady-state kinetics and spectroscopic characterization of enzyme-tRNA interactions for the non-heme diiron tRNA-monooxygenase, MiaE

Bishnu P. Subedi, Andra L. Corder, Siai Zhang, Frank W. Foss, Jr., and Brad S. Pierce, Department of Chemistry and Biochemistry, College of Sciences, The University of Texas at Arlington, Arlington, Texas 76019 (Published in *Biochemistry,* 2015, *54* (2): 363-376)

Abstract

MiaE (2-methylthio-N^6-isopentenyl-adenosine(37)-tRNA monooxygenase) isolated from S*almonella typhimurium* is a unique non-heme diiron enzyme which catalyzes the O_2-dependent post-transcriptional allylic hydroxylation of a hypermodified nucleotide ($ms^2i^6A_{37}$) at position 37 of selected tRNA molecules to produce 2-methylthio-N^6-(4-hydroxyisopentenyl)-adenosine(37). In this work, isopentenylated tRNA-substrates for MiaE were produced from small RNA oligomers corresponding to the anticodon stem loop (ACSL) region of $tRNA^{Trp}$ using recombinant MiaA and dimethylallyl pyrophosphate (DMAPP). Steady-state rates for MiaE catalyzed substrate-hydroxylation were determined using recombinant ferredoxin (Fd) and ferredoxin reductase (FdR) to provide a catalytic electron transport chain (ETC) using NADPH as the sole electron source. As with previously reported peroxide-shunt assays, steady-state product formation retains nearly stoichiometric (> 98%) *E*-stereoselectivity. MiaE-catalyzed i^6A-$ACSL^{Trp}$ hydroxylation follows Michaelis-Menten saturation kinetics with k_{cat}, K_M, and V/K determined to be $0.10 \pm 0.01\ s^{-1}$, $9.1 \pm 1.5\ \mu M$, and $\sim 11{,}000\ M^{-1}s^{-1}$, respectively. While vastly slower, MiaE-catalyzed hydroxylation of free i^6A nucleoside could also be observed using the (Fd/FdR)-ETC assay. By comparison to the *V*/*K* determined for i^6A-ACSL substrates, a ~6,000-fold

increase in enzymatic efficiency is imparted by ACSL^{Trp}-MiaE interactions. The impact of substrate tRNA-MiaE interactions on protein secondary structure and active site electronic configuration was investigated using Circular Dichroism (CD), dual mode X-band EPR, and Mössbauer spectroscopies. These studies demonstrate that tRNA-binding to MiaE induces a protein conformational change which influences the electronic structure of the diiron site analogous to what has been observed for various bacterial multicomponent diiron monooxygenases upon titration with their corresponding effector-proteins. These observations suggest that substrate-enzyme interactions may play a pivotal role in modulating the reactivity of the MiaE diiron active site. Moreover, the simplified monomeric (α) protein configurations exhibited by MiaE provides an unparalleled opportunity to study the impact of protein-effector interactions on non-heme diiron site geometry and reactivity.

Introduction

To date, nearly 90 post-transcriptional modifications of transfer RNA (tRNA) have been identified across all phylogenic domains of life (Archaea, Bacteria, and Eucarya)(*159, 160*). These modifications are made to structurally diversify tRNA, resulting in altered function and interactions with amino acids and the ribosomal machinery (*161*). In many instances, the physiologic role of such modifications is unclear; however, several examples have been identified to suggest that the presence of modified nucleotides in tRNA can impact aminoacyl-tRNA selection, decrease translational frame-shifting, regulate central metabolism (*citric acid cycle and thiamine biosynthesis*), as well as initiate genes involved in bacterial virulence (*159, 162*). As the ribosomal machinery has historically proven to be an effective target for the development of anticancer, antibiotic, and antiviral agents, the characterization of enzymes involved in nucleotide transformations represent a rich area of mechanistic study with high potential impact on human health (*163-166*).

Scheme 3.1 Hypermodification enzyme pathway for 2-methylthio-*N*^{6}-(4-hydroxy isopentenyl) adenosine (ms^{2}io^{6}A$_{37}$) synthesis

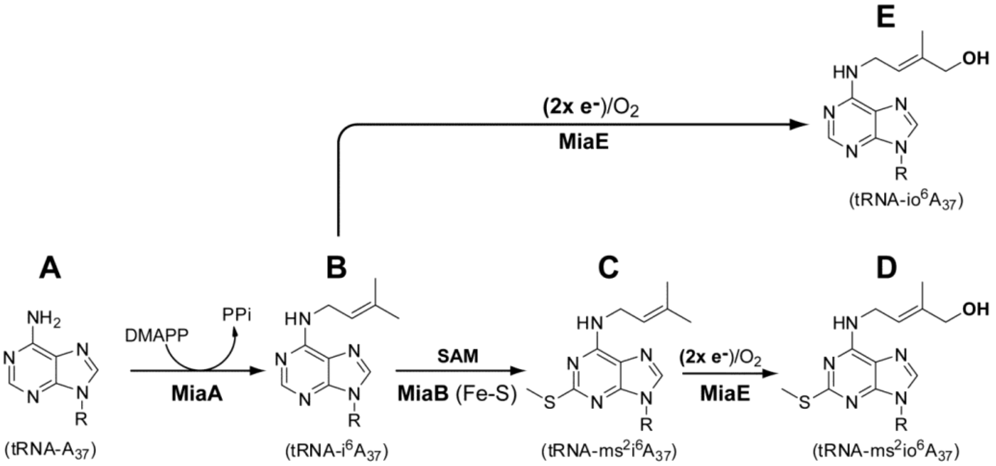

Within the anticodon stem loop (ACSL) of tRNA, nucleotide modifications are frequently observed at position 34 (the wobble position) or position 37 (3' adjacent to anticodon)(*167, 168*). In some instances, modifications employ multiple enzymes within a complex biochemical pathway to produce hypermodified nucleotides. For instance, nearly all eukaryotic and bacterial tRNAs that read codons starting with U are modified by the enzymes MiaA and MiaB as illustrated in Scheme 3.1. In the first step, dimethylallyl (Δ^2-isopentenyl) diphosphate-tRNA transferase [E.C. 2.5.1.8] (designated MiaA) catalyzes the nucleophilic substitution of the dimethylallyl group from dimethylallyl pyrophosphate (DMAPP) to the exocyclic 6-amino nitrogen of A$_{37}$ (N^6) to yield *N*^{6}-isopentenyl-adenosine (i^{6}A$_{37}$) with release of inorganic pyrophosphate(*89*). The second enzymatic transformation involves the formal methylthiolation of i^{6}A$_{37}$ at the C2-position to produce 2-methylthio-*N*^{6}-isopentenyl-adenosine (ms^{2}i^{6}A$_{37}$). The enzyme that catalyzes this remarkable transformation (2-methylthio-*N*^{6}-isopentenyl-adenosine synthase, designated MiaB) requires S-adenosylmethionine as a co-substrate and is a member of the radical *S*-

adenosylmethionine (SAM) methylthiotransferase family of enzymes(*90-92*). With the notable exception of $tRNA_{I,V}^{Ser(GGA)}$, nearly all eukaryotic and bacterial tRNAs that read codons starting with U contain the ms^2i^6A-modification(*79, 160*). While absent in eukaryotes, some facultative bacteria use a non-heme diiron enzyme (MiaE, 2-methylthio-*N*^{6}-isopentenyl-adenosine(37)-tRNA monooxygenase) to catalyze the O_2-dependent hydroxylation of $ms^2i^6A_{37}$ to produce 2-methylthio-*N*^{6}-(4-hydroxyisopentenyl)-adenosine ($ms^2io^6A_{37}$)(*87*). While MiaE can utilize i^6A_{37} as a substrate, whole cell assays suggest a preference for $ms^2i^6A_{37}$(*94-96*). As previously mentioned, MiaA and MiaB are common in both eukaryotes and prokaryotes; by contrast, MiaE is only found within a small subset of facultative anaerobic bacteria such as S*almonella typhimurium* (*82*). It has been postulated that within these bacteria the extent of A_{37}-hydroxylation is involved in regulating aromatic amino acid uptake, enterochelin synthesis, iron transport, and aerobiosis (*79, 80, 82, 83, 162*).

MiaE is a member of the non-heme diiron family of enzymes (*78, 83, 87*). Other members of this family include the hydroxylase components of the bacterial multicomponent monooxygenases (BMM) [methane monooxygenase (MMOH), toluene-monooxygenases (ToMOH)], the small subunit of ribonucleotide reductase (R2), and stearoyl-acyl carrier protein Δ^9-desaturase (Δ9D)(*57, 60, 67*). This incredibly diverse family of enzymes has been identified all throughout the biological kingdom and are capable of catalyzing an impressive array of chemical oxidations (mono- and dioxygenations, aliphatic desaturation)(*57*). Remarkably, despite accommodating a broad spectrum of substrates, the first-coordination sphere of the diiron active site is essentially conserved among non-heme diiron oxidase/oxygenase enzymes.

The typical quaternary protein structure observed in non-heme diiron enzymes is multimeric (*65*). Indeed, among the hydroxylase components of bacterial multicomponent monooxygenase (BMM) enzymes, a non-covalent heterotrimeric dimer complex $(\alpha\beta\gamma)_2$ is the most frequently observed protein configuration (*66*). By contrast, the simplest quaternary structure reported for non-heme diiron enzymes is homodimeric (α_2). For instance, both the small subunit of ribonucleotide reductase (R2) and stearoyl-acyl carrier protein (18:0-ACP) Δ^9-desaturase (Δ9D) exhibit a homodimeric protein configuration in which each protomer contains a diiron active site (*57, 60, 67*). Perhaps coincidentally, it has been reported that both Δ9D and R2 exhibit properties consistent with "half-sites" reactivity, implying that the two protomers of these homodimeric enzymes do not act independently during catalysis (*70-72, 169*). For example, rapid-mix/chemical quench experiments with Δ9D demonstrate the most compelling evidence for "half-sites" reactivity within a non-heme diiron enzyme. In these reactions, the prereduced enzyme-substrate complex (Δ9D:18:0-ACP) was rapidly mixed with O_2-saturated buffer prior to chemical quenching at selected time points. Formation of the observed product (18:1-ACP) followed two distinct kinetic phases, an initial "burst phase" (k_{burst} ~ 95 s^{-1}) followed by a second linear phase (k_{linear} ~ 4 s^{-1})(*170*). As Δ9D is a homodimer, each protomer has an equivalent diiron site capable of generating product, and thus, the expected amplitude of this burst phase should be twice the protein concentration. Remarkably, the observed amplitude in these experiments was roughly equivalent to one product (18:1-ACP) generated per Δ9D homodirmer. On the basis of these experiments, it was concluded that the two active sites within Δ9D are not simultaneously catalytically active.

In stark contrast to the multimeric protein configuration exhibited by all other non-heme diiron monooxygenases, MiaE exhibits a monomeric (α) protein configuration (*one active site within a single protomer*) as indicated by size exclusion chromatography(*87*) and analytical ultracentrifugation(*78*). To the best of our knowledge, this is the first example of a monomeric non-heme diiron oxygenase/oxidase. Therefore, this enzyme provides an unprecedented opportunity to study a minimal non-heme diiron enzyme in the absence of any potential for inter-protomer cooperativity.

In this work, the steady-state kinetics of MiaE-catalyzed tRNA hydroxylation and the impact of protein-tRNA interactions on kinetics, protein secondary structure, and active site electronic configuration were characterized using Circular Dichroism (CD), parallel mode Electron Paramagnetic Resonance (EPR), and Mössbauer spectroscopy. Remarkably, the g ~ 16 parallel mode EPR signal of the reduced enzyme shifts upon binding RNA oligomers corresponding to the ACSL-region of MiaE tRNA-substrates. This spectroscopic shift is remarkably similar to what has been previously reported for the reduced bacterial multicomponent diiron monooxygenases upon titration with their corresponding effector-proteins (*97, 98, 104, 105, 171, 172*). These spectroscopic results provide scaffolding for more in-depth investigation of this enzyme. Furthermore, given the simplified monomeric (α) protein configurations exhibited by MiaE, characterization of this enzyme represents an unprecedented opportunity to study the impact of protein-effector interactions on non-heme diiron site geometry and reactivity.

Materials and methods

Cloning of MiaA. The *miaA* gene was isolated from *Salmonella enterica* strain LT2 genomic DNA [ATCC 700720] using primers purchased from Integrated DNA Technologies (https://www.idtdna.com). A two-step PCR amplification was used to isolate the ORF from genomic DNA and incorporate restriction sites (Sgf I/Pme I) for Flexi-vector cloning (Promega, Madison, WI), followed by insertion of a recognition site for tobacco etch virus protease (TEV). First, (miaA specific) PCR reaction primers: forward 5'-(AAC CTG TAC TTC CAG TCC AAT GAT GTA AGC AAG GCG AGC CTG)-3'; reverse 5'-(GCT CGA ATT CGT TTA AAC TAG TCT GCG ATA GCA CCA ACA ACC)-3'. Second, (TEV site insertion) primers: forward: 5'-(GGT TGC GAT CGC CGA AAA CCT GTA CTT CCA GTC C)-3'; reverse: 5'-(GTG TGA GCT CGA ATT CGT TTA AAC)-3'. The DNA produced by this two-step PCR amplification was cloned into an IPTG-inducible T7 vector (designated pVP80K) as described previously for the MiaE-expression vector.(*78*) Sequence verification of *miaA* was performed by Sequetech (Mountain View, CA, http://sequetech.com/). The resulting plasmid expresses an N-terminal fusion of maltose binding protein (MBP) and MiaA.

Enzyme Purification.

MiaA expression and purification. The MiaA expression vector (pMIAAK) was transformed into competent BL21(DE3) *E. coli* cells (Novagen) by heat shock and was grown overnight on a LB media agar plate containing 25 μg/mL Kanamycin (Kan) at 37 °C. The following day, a single colony was selected for growth in liquid LB (Kan) media for training on antibiotic prior to inoculation of 10-L BF-110 fermentor (New Brunswick Scientific) at 37 °C. Cell growth was followed by optical density at 600 nm (OD_{600}). Induction was initiated by addition of 0.5 mM IPTG and 20 g casamino acids at an OD_{600} ~4. Upon induction the temperature of the bioreactor was decreased from 37 °C to 25 °C and agitation was set to maintain an O_2 concentration of 20% relative to air-saturated media. After 4 hours of induction, the cells were pelleted by centrifugation (Beckman-Coulter Avanti J-E, JA 10.5 rotor) at 18,600 × g for 15 min, and the paste was stored at -80 °C. Confirmation of MiaA expression was performed by SDS-PAGE of lysed cells before and after IPTG induction. In a typical MiaA purification, ~10 g of frozen cell paste was thawed on ice in a lysis buffer (20 mM HEPES, 100 mM NaCl, pH 8.0) along with 10 μg/mL each of lysozyme, deoxyribonuclease I, and ribonuclease. Once thawed, the cell suspension was sonicated for 30 sec on/off pulse cycle for a total time of 10 min. The resulting slurry was then centrifuged at 4 °C (48,000 × g) for 1 hour. Following centrifugation, the supernatant was decanted from the pellet and then loaded onto a pre-equlibrated amylose column (NEB, 13.0 cm × 3.5 cm). Unbound protein and impurities were washed from the column by addition of 100 mL of the pre-equilibration/wash buffer (20 mM HEPES, 300 mM NaCl, 0.3 mM Tris[2-carboxyethyl] phosphine (TCEP), pH 8.0). Elution of MBP-MiaA fusion protein was performed by addition of 3 column volumes maltose buffer (20 mM HEPES, 300 mM NaCl, 20 mM maltose, 0.3 mM TCEP, pH 8.0). Recovered protein was concentrated by Amicon/N_2 stir cell equipped with an Ultracel 30 KDa ultra-filtration membrane (Millipore). The MBP-affinity tag was removed by overnight TEV protease cleavage as described elsewhere (*78*). Protein purity and concentration was confirmed by SDS-PAGE and Bradford protein assay, respectively.

TEV protease purification and reaction conditions*.* Tobacco Etch Virus (TEV) protease was purified through Ni-IMAC column as described previously (*78*). MBP-fusion proteins were cleaved at 4 °C with TEV protease (5:1 equivalent based on absorbance at 280 nm) in HEPES buffer (20 mM HEPES, 100 mM NaCl, 0.3 mM TCEP, pH 8.0).

MiaE expression and purification*.* Protocols for MiaE expression, purification, and cleavage from MBP-fusion protein are described in detail elsewhere (*78*). The ^{57}Fe enriched MiaE protein was prepared for Mössbauer study by growing MiaE vector in M9 media where iron-57 was used as only iron source during growth and expression of bacteria. The purity and concentration of MiaE protein was determined by UV-visible spectroscopy (A_{280}/A_{370} ~7.8).

Ferredoxin (Fd). *Anabaena* vegetative [2Fe-2S] ferredoxin was expressed and purified as described elsewhere (*173, 174*). Briefly, cell free extract was loaded onto a DEAE anion exchange column pre-equilibrated in 20 mM HEPES, 50 mM NaCl, pH 8.0. Protein was eluted using a NaCl gradient (50 - 400 mM NaCl) at pH 8. The purity of protein was confirmed both through SDS-PAGE analysis and UV-visible spectroscopy. Protein concentration was determined using the known molar extinction coefficient ($\varepsilon_{420\ nm}$ = 9,700

$M^{-1}cm^{-1}$). The ferredoxin expressing T7 IPTG inducible vector was a generous gift from Professor Brian G. Fox (University of Wisconsin, Department of Biochemistry).

Ferredoxn NADP+ reductase (FdR). Spinach FdR was purchased from Sigma Aldrich (CAS No. 9029-33-8) and reconstituted to desire concentration in 20 mM Tris buffer (pH 8.0) before use.

Anticodon stem loop (ACSL) of tRNA. Small 17 nucleotide RNA oligomers corresponding to the anticodon stem loop of *Salmonella typhimurium* were purchased from Integrated DNA Technology (idtdna.com). Sequence and designation for each RNA oligomers used in these experiments: $ACSL^{Trp}$ $[^{27}$CCGGUCUCCAAAACCG^{43}G]; $ACSL^{Leu}$; ^{28}GUUGAUUCAAAAUCAA^{44}C]; $ACSL^{Met}$; $[^{28}$CAUCACUCAUAAUGAU^{44}G]. For clarity, the A targeted for MiaA and MiaE modification (A_{37}) is designated by bold/underline. For control experiments, a single stranded 10 nucleotide RNA oligo sequence [GGCUACGUAG] was employed (*termed ssRNA*). This sequence lacks the ability to form a hairpin loop and thus represents a control for adventitious binding of single stranded RNA. All lyophilized RNA oligomers were reconstituted in buffer (30 mM HEPES, 100 mM KCl, 2 mM $MgCl_2$, and 50 mM ammonium acetate, pH 7.0). The final concentrations for each RNA solution was based on the exact mass of RNA oligomer reported by IDT quality assurance and separately confirmed by NanoDrop UV-visible spectrophotometer (Thermo Scientific). To ensure homogeneous RNA folding into a stable hairpin loop, solutions of RNA oligomers were temperature annealed as described previously(*175*). Briefly, a PCR thermal cycler (MJ mini gradient/Bio-Rad) was utilized to raise the temperature of RNA solutions (25-50 μL) to 95 °C over the course of 2 min. After 1 sec at 95 °C, solutions were then cooled to 4 °C over the course of 35 min. RNA secondary structure was confirmed by CD, J-715 spectropolarimeter (JASCO Inc., Easton, MD, USA).

MiaA activity assay. Approximately 6 μM ACSL^{Trp} was annealed and treated with 200 nM of MiaA, 100 μM dimethyl allyl pyrophosphate (DMAPP), and 100 μg bovine serum albumin (BSA) in a 1 mL TMD buffer (60 mM Tris HCl, 20 mM $MgCl_2$, and 2 mM DTT, pH 7.5) at ambient temperature (22 ± 2 °C) to isopentenylate the A37 within the ACSL^{Trp} sequence. For kinetic studies, sample aliquots were removed at selected time points (1 - 60 min), heat denatured at 95 °C for 2 min, and stored on ice prior to analysis by HPLC.

MiaE activity assay. For the MiaE enzyme assays using an *in vitro* electron transport chain (ETC), solutions of i^{6}A-ACSL^{Trp} were prepared following MiaA reaction at selected concentrations (3 - 60 μM) for steady-state experiments. To each solution, MiaE, Fd, FdR, were added to obtain a final concentration of 0.5 μM, 4 μM, and 4 μM, respectively. Reactions were initiated by addition of 500 μM NADPH. Sample aliquots were collected at different time period (1 - 5 min), heat denatured at 95 °C for 2 min, and then placed in ice prior to analysis by HPLC. For free nucleoside substrate kinetics, samples of the synthetic isopentenylated adenosine (i^{6}A) were prepared (0.5 – 5.0 mM) under identical conditions as described above for i^{6}A-ACSL reactions.

HPLC sample preparation. Free nucleosides were generated from modified RNA oligonucleotides for HPLC analysis following methods previously published (*78, 121*). Sample aliquots (60 μL) containing RNA oligomers were treated with 5 μL 10 mM $ZnSO_4$, 10 μL of nuclease P1 (200 units/mL, in 30 mM sodium acetate buffer, pH 5.4), and incubated for 16 hours at 37 °C to cleave the RNA oligomer into its constitutive nucleotides. Following cleavage, 10 μL of 0.5 M Tris buffer, pH 8.3 and 10 μl of bacterial alkaline phosphatase (BAP) (100 units/mL, in 2.5 M ammonium sulfate) were added and allowed to incubate for an additional 2 hours at 37 °C to remove the nucleotide 5'-phosphate group. The resulting nucleoside solutions were then filtered through a 0.22 μM Spin-X centrifuge tube (Costar®) prior to HPLC analysis.

HPLC analysis. Shimadzu quaternary pump LC (LC-20AD XR/LC 30AD) equipped with a photodiode array detector (SPD-M20A); Column, Phenomenex, Gemini-NH 3 μm C18 110 Å; 150 cm × 4.6 mm; Mobile phase, (A) 2.5% methanol in 0.01 M $NH_4H_2PO_4$; pH 5.3, (B) 20% methanol in 0.01 M $NH_4H_2PO_4$; pH 5.1, (C) 35% acetonitrile in 0.01 M $NH_4H_2PO_4$; pH 4.9; Injection volume, 20 μL; Flow rate, 1 mL/min; Column temperature, 25 °C; UV-visible detection was monitored at 266 nm (λ_{max} of i^6A) and 272 nm (λ_{max} of io^6A). The concentrations of i^6A (retention time, 67.3 min) and *E*-io^6A (retention time, 55.5 min) were determined by comparison to standard calibration curves (0.01-5 mM) produced from synthetic standards (*78*).

LC-MS/MS and data analysis. Verification of enzymatic product was performed by multiple reaction monitoring (MRM) using a triple-quadruple LC-MS/MS [Shimadzu Scientific Instruments, LCMS 8040](*122*). The molecular ions (M^+) of the enzyme substrate (i^6A, 336 m/z) and product (io^6A, 352 m/z) were selected for secondary fragmentation. MRM optimization was then employed to maximize transition intensity and sensitivity for each fragment allowing for quantitation of product ions. The optimized MRM method was used to verify both substrate and product by direct injection of enzymatic assays. These results were compared to direct injection of synthetic standards.

EPR/Mössbauer sample preparation. Reduced EPR samples were prepared inside the anaerobic glove box (Coy Laboratory Products Inc.) by addition of stoichiometric sodium dithionite solution (30 mM) mediated with methyl viologen. Dithionite solutions were prepared fresh and calibrated as described elsewhere(*78*). For ACSL-titrations, a 1 mM stock solution of ACSL^{Trp} was added (0 to 95 μL) via a Hamilton 100 μL gas-tight syringe to 180 μL 350 μM reduced MiaE in a 1.0 mL Eppendorf microfuge tube. Following ACSL^{Trp}-additions, anaerobic buffer was used to dilute samples to a final volume of 275 μL resulting in a final MiaE concentration of 230 μM. EPR samples were then allowed to equilibrate on ice for 15 minutes prior to transferring the sample into a 4 mm Quartz EPR tube (707-SQ-250MM; Wilmad-Lab Glass) by 250 μL Hamilton gas-tight syringe equipped with a 6'' needle. Finally, EPR tubes were frozen slowly in liquid N_2 under anaerobic conditions prior to analysis. Mössbauer samples were prepared under identical anaerobic conditions and reduced (*if necessary*) as described for EPR samples. All samples were prepared from a stock solution of 1.9 mM of ^{57}Fe enriched enzyme. Aliquots were taken from the enzyme stock (250 μL), reduced (if necessary), and then diluted with anaerobic buffer to obtain equivalent 500 μL samples of 960 μM ^{57}Fe-MiaE (*oxidized* and *reduced*). Samples of the (ACSL^{Trp}/MiaE)-complex were prepared by mixing 240 μL 1.9 mM ^{57}Fe-MiaE with 260 μL 2.6 mM ACSL^{Trp} stock solution to obtain a final ACSL^{Trp} to MiaE molar ratio of 1.5 to 1.0.

Spectroscopy.

UV-visible spectroscopy. All UV-visible measurements were performed on an Agilent 8453 photo diode array spectrometer (Santa Clara, CA). Measurements were made in ES Quartz cuvettes (NSG Precision Cells, Farmingdale, NY).

Circular Dichroism (CD). All CD experiments were performed on JASCO 715 UV-visible circular dichroism spectrometer with xenon arc light source. Unless otherwise stated, protein samples analyzed by CD were prepared in 10 mM sodium phosphate buffer (pH

8.0) filtered through a 0.22 μm polypropylene membrane filter (VWR international). Equine heart myoglobin (100684-32-0), chicken egg white lysozyme (12650-88-3), and poly-L-lysine (25988-63-0) purchased from Sigma-Aldrich were used as standards for secondary structure determination as described elsewhere.(*176*) CD results were also interpreted using the freely available online software K2D3 (http://k2d3.ogic.ca/). Far-UV (185-300 nm) CD spectra of protein were recorded in a quartz cuvette of 0.1 cm path length and ~0.45 mL volume at a scan speed of 40 nm/min at ambient temperature. In a typical CD experiment, 5 μL 450 μM MiaE enzyme was added to 445 μL buffer to obtain a final concentration of 5 μM in the cuvette. In RNA-binding experiments, MiaE (5 μM) was titrated with increasing concentration of ACSL RNA oligomers (0 to 2 molar equivalents). Stock solutions of RNA oligomer were prepared at 500 μM such that RNA additions did not significantly dilute the sample or alter the buffer composition. All spectra were signal averaged (n = 3) for noise reduction.

Analysis of CD titration data. The normalized change in ellipticity ($\Delta\theta$) were fit using a single site equilibrium binding model (eq. 1), which assumes reversible binding of substrate (A) and enzyme (E) to produce a substrate-bound complex (EA). The concentration of each species can be described by eq. 2 and 3, and solved for EA in terms of E_t, A_t, and K to yield eq. 4. Since both E_t and A_t are known, the concentration of EA is dependent only on K, which is determined by non-linear least squares fitting to eq. 4. For simplicity, the binding constant (K_D) is substituted for $1/K$ in eq. 4.

Equation 1. $$K = [EA]/([E_f] \cdot [A_f])$$

Equation 2. $$E_t = E_f + EA$$

Equation 3. $$A_t = A_f + EA$$

Equation 4. $$[EA] = \frac{([A_t]+[E_t]+{}^{1}/_{K})\pm\sqrt{([A_t]+[E_t\}+{}^{1}/_{K})^2-4[A_t]\cdot[E_t\}}}{2}$$

EPR spectroscopy. X-band (9 GHz) EPR spectra were recorded on a Bruker (Billerica, MA) EMX Plus spectrometer equipped with a bimodal resonator (Bruker model 4116DM). Low-temperature measurements were made using an Oxford ESR900 cryostat and an Oxford ITC 503 temperature controller. A modulation frequency of 100 kHz was used for all EPR spectra. All experimental data used for spin-quantitation were collected under non-saturating conditions as verified by half-power microwave saturation ($P_{1/2}$). EPR spectra of reduced MiaE were simulated by diagonalization of the spin-Hamiltonian (eq. 5) using SpinCount ver. 5.3.5190.24657 software (created by Professor M.P. Hendrich, Carnegie Mellon University). Here, J is the exchange coupling constant between the two ferrous iron sites (S_1 = S_2 = 2), g is the g-tensor, and the axial and rhombic zero-field splitting parameters are represented by D and E, respectively.(*177*)

Equation 5. $$\widehat{H} = -2J(\mathrm{S}_1\cdot\mathrm{S}_2) + \sum_{i=1}^{2}[D_i(\hat{S}_{zi}^2-2) + E_i\,(\hat{S}_{xi}^2-\hat{S}_{yi}^2) + \beta_e S_i\cdot g_i\cdot\mathrm{B}]$$

This equation simplifies under the assumption that the exchange coupling constant (J) is comparable in energy to (*or larger*) than the zero-field splitting (D) of the diferrous cluster. Under this constraint, the S = 4 Hamiltonian takes the form illustrated in eq. 6.

Equation 6. $$D(\hat{S}_z^2-\frac{\hat{S}^2}{3}) + E(\hat{S}_x^2-\hat{S}_y^2) + \beta_e S\cdot g\cdot\mathrm{B}]$$

This program computes the powder pattern for a uniform spherical distribution of the magnetic field vector B, and the transition intensities are calculated using ‘Fermi’s golden rule’ (*178*). The simulations are generated with consideration of all intensity factors, both theoretical and experimental. The concentration of species can be used as a constraint during spectral simulation, which allows quantitative determination of the concentration by comparison of the experimental and simulated signal intensities (*179*). The only unknown factor relating the spin concentration to signal intensity is an instrumental factor that depends on the microwave detection system. This factor is determined using a Cu(II)EDTA spin standard (*180*), (*78*).

The half-power microwave saturation $P_{1/2}$ for reduced MiaE as a function of ACSL^{Trp} concentration was determined using the SpinCount software package according to eq. 7.

Equation 7. $$S/\sqrt{P} = \frac{A}{\left(1+P/P_{1/2}\right)^{b/2}}$$

The software performs least-squares fitting of the normalized derivative signal intensity (S) as a function of microwave power (P). The A-term represents the normalized maximum signal amplitude. The variable b is a spectroscopic inhomogeneity factor which is characteristic of the spin packet of the observed resonance. Generally, the signal packet derived from frozen solutions and powders exhibit inhomogeneous line broadening behavior (b = 1).

Mössbauer spectroscopy. Mössbauer spectra for ^{57}Fe-incorporated resting and reduced MiaE were collected at 4 K on a model MS4 WRC spectrometer equipped with a closed-loop cryostat system (SEE Co., Edina, MN) as described elsewhere (*181*). Spectral fitting was performed using SpinCount.

Results

Enzymatic Assays. To evaluate the steady-state kinetics of MiaE i^6A-hydroxylation, isopentenylated RNA oligomers were first enzymatically synthesized using recombinant MiaA. It has been reported that the minimal substrate for bacterial MiaA is the anticodon stem loop (ACSL) of targeted tRNA molecules,(*175*) therefore a 17 nucleotide oligomer corresponding to the ACSL region of $tRNA^{Trp}$ [^{27}CCGGUCUCCAAAACCG^{43}G, designated $ACSL^{Trp}$ henceforth] was selected as a starting substrate for enzymatic assays. The activities of recombinant *Salmonella typhimurium* MiaA and MiaE were monitored using the reverse phase HPLC method. As illustrated in the HPLC chromatogram (Figure 3.1, trace 1), addition of 200 nM MiaA to a buffered solution containing $ACSL^{Trp}$ (5.6 μM) and excess DMAPP (100 μM) results in formation of a peak at 67.3 min (*open circle*). This new peak matches the retention time, UV-visible absorption features, and mass spectra (*described below*) of the synthetic i^6A nucleoside standard. Figure 3.2 (A) shows the rate of i^6A-$ACSL^{Trp}$ production for duplicate MiaA-catalyzed reactions over 1 hour. The amplitude of i^6A product formation upon completion of the reaction ($A = 4.94 \pm 0.03$ μM) and the pseudo-first order rate constant [$k_{obs} = (1.1 \pm 0.1) \times 10^{-3}$ s^{-1}] were determined from the best fit. Along with the rate of i^6A-$ACSL^{Trp}$ formation observed at 67.3 min (Figure 3.1), a concomitant decrease in the adenosine peak area (*filled triangle*, 26 min) can be observed (*data not shown*). The initial rate of this reaction can be obtained from the product amplitude and the pseudo-first order rate constant ($v_0 = k_{obs} \cdot A$), thus the enzyme (MiaA) normalized initial rate (v_0/[E]) for i^6A-ACSL formation is 0.028 ± 0.004 s^{-1}. The observed change in amplitude of i^6A formation of the single-exponential phase accounts for ~ 88% of the expected stoichiometry for MiaA catalyzed ACSL-isopentenylation. Therefore, under these conditions, nearly complete formation of i^6-$ACSL^{Trp}$ is observed within 1 hour at ambient temperature.

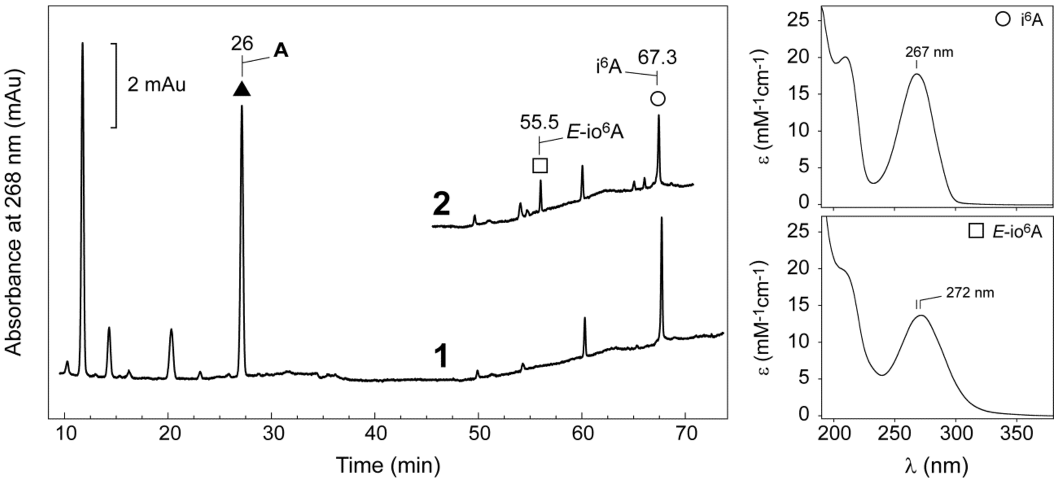

Figure 3.1 HPLC Assay. (*Left*) Representative HPLC chromatograms of i^{6}A and io^{6}A nucleosides, chromatogram 1 shows i^{6}A peak (circle, at 67.3 min) produced by the reaction of ACSL with enzyme MiaA in the presence of excess DMAPP, chromatogram 2 shows the product of i^{6}A-ACSL reaction with MiaE (square, *E*-io^{6}A produced at 55.5 min). (*Right*) UV-Vis absorption spectra of synthetic i^{6}A and *E*-io^{6}A standards.

Confirmation of MiaA product identity was verified using LC-MS/MS by multiple reactions monitoring (MRM). As illustrated in Figure 2 (panels B and C), direct injection of the i^{6}A synthetic standard and enzymatic assay produced identical fragmentation patterns. The top panel (Figure 3.2B) represents MRM mass spectrum (336 m/z molecular ion) observed for the i^{6}A nucleoside. For comparison, panel (C) shows the mass spectrum obtained by direct injection of MiaA enzymatic assays. Given the matching fragmentation pattern and relative intensities obtained for the MiaA product, it can be concluded that the product generated within MiaA is indeed the i^{6}A-ACSL^{Trp}.

Previously, the peroxide-shunt catalyzed rates of hydroxylation were reported for MiaE using three synthetic β-nucleoside substrates [2-thiomethyl-*N*^{6}-(3-methyl-2-butenylamino) adenosine (ms^{2}i^{6}A); *N*^{6}-(3-methyl-2-butenylamino) adenosine (i^{6}A); and 2-chloro-*N*^{6}-(3-methyl-2-butenylamino) adenosine (Cl^{2}i^{6}A)].(*78*) While the peroxide-shunt pathway removes the need for an external electron source, such reactions are frequently slower and exhibit decreased chemo- and stereo-selectivity as compared to reactions utilizing a functional electron transport chain. Therefore, in order to better understand the physiologically relevant MiaE catalytic system, a functional electron transport chain was constructed on the basis of what has worked previously with the soluble stearoyl-ACP Δ^9-desaturase (*169, 170, 182*). In these reactions, NADPH serves as the electron source, and ferredoxin reductase (FdR) and ferredoxin (Fd) provide an electron transport chain (ETC) to shuttle electrons from NADPH to the diiron active site of MiaE. In a typical reaction, the i^6A-ACSL^{Trp} substrate is generated using recombinant MiaA as described above. Prior to initiating the MiaE reaction, the concentration of i^6A-ACSL^{Trp} produced is verified by HPLC as described within *Materials and Methods*. Substrate i^6A-ACSL solutions are generated in concentrations ranging from 0 to 60 μM. To these solutions were added purified MiaE, Fd, and FdR, and reactions were initiated by addition of 500 μM NADPH. At selected time points, aliquots are quenched by heat denaturation and worked up for HPLC analysis. A representative HPLC chromatogram for illustrating the *E*-io^{6}A peak (55.5 min) is shown in Figure 3.1 (trace 2). Confirmation of MiaE product and stereochemistry was performed as previously described (*78*).

As with peroxide-shunt assays reported previously, the product of (Fd/FdR-ETC) steady-state assays retains nearly stoichiometric (>98%) *E*-stereoselectivity. In contrast to what was previously observed in peroxide-shunt assays,(*78*) the initial rate of MiaE catalyzed i^6A-ACSL^{Trp} hydroxylation utilizing the *in vitro* (Fd/FdR-ETC) follows typical saturation kinetics as illustrated in Figure 3.3. The Michaelis-Menten parameters, k_{cat}, K_M, and V/K determined by best fit are 0.10 ± 0.01 s^{-1}, 9.1 ± 1.5 μM, and ~ 11,000 M^{-1}s^{-1}, respectively. LC-MS/MS (MRM transitions) of the *E*-io^{6}A standard and MiaE product are shown in Figure 3 (B and C), respectively. As expected for a monooxygenase reaction, the molecular ion [M^+ = *m/z* 352.2] observed for the MiaE-hydroxylated product is increased by 16 m/z relative to the i^6A-substrate [Figure 2, M^+ = *m/z* 336.2]. Secondary fragmentation of the parent ion produces peaks at *m/z* 136.2, 202.2 and 220.2. The *m/z* 220.2 peak is assigned to an *N*^{6}-(4-hydroxyisopentenyl)adenine ion on the basis of the *m/z* +16 shift observed relative to i^6A, whereas the *m/z* 136.2 and 202.2 peaks are assigned to adenine and *N*^{6}-(4-methylbutadiene)adenine fragmentation ions respectively (*183*). To the best of our knowledge, this represents the first instance of steady-state kinetic values reported for any MiaE enzyme.

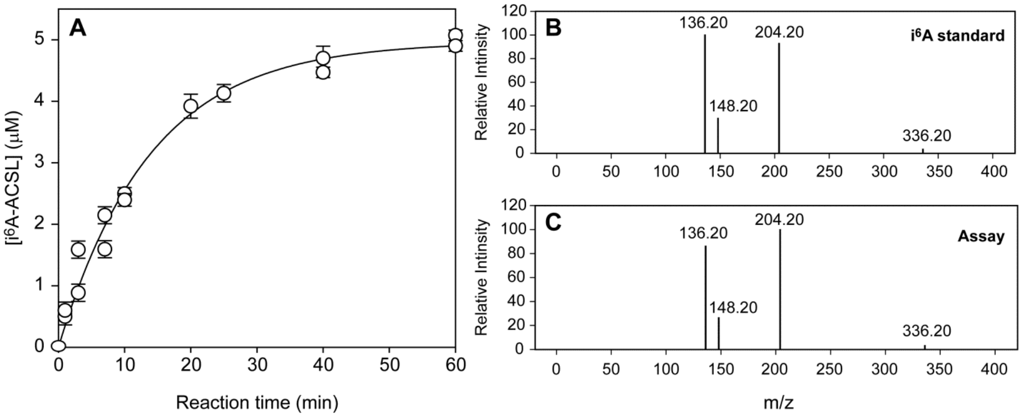

Figure 3.2 MiaA catalysis. (A) Rate of MiaA-catalyzed *N*^{6}-isopentenyl-adenosine ACSL formation (i^6A_{37}-ACSL). LC-MS/MS spectra of MRM transitions of designated i^6A product ions are shown within the right panels; (B) corresponds to the i^6A synthetic standard and (C) illustrates the direct injection of enzymatic product.

While vastly slower, the MiaE catalyzed hydroxylation of free i^6A nucleoside can also be observed using the (Fd/FdR-ETC) steady state assay. As shown in the inset of Figure 3.3A, full substrate saturation of MiaE is never observed within the solubility limit of the nucleoside (~5 mM). This same behavior was observed in peroxide-shunt assays as well (*78*). From the slope of the line, the pseudo-second order rate constant (approximately

k_{cat}/K_m) can be determined (1.9 ± 0.1 $M^{-1}s^{-1}$). By comparison to the *V*/*K* determined for i^6A-$ACSL^{Trp}$ substrates, a nearly 6,000-fold increase in enzymatic efficiency is imparted by reactions containing the 17 nucleotide i^6A-$ACSL^{Trp}$ as compared to the free i^6A nucleoside.

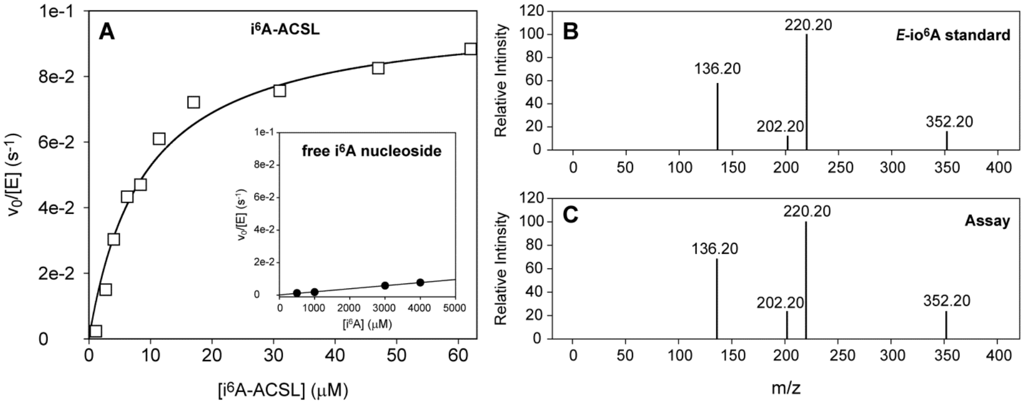

Figure 3.3 Steady state kinetics of MiaE assays. (A) Steady state kinetics for MiaE-catalyzed hydroxylation of i^6A-$ACSL^{Trp}$ as compared to the free i^6A nucleoside (*inset*). The top panel (B) corresponds to the *E*-io^6A synthetic standard and the lower panel (C) illustrates the direct injection of enzymatic product.

CD Spectroscopy. The impact of substrate tRNA-MiaE interactions on secondary structure was investigated by CD spectroscopy. Since the RNA oligomers utilized lack the i^6A-modificaiton, these experiments are designed to investigate to what extent the RNA secondary structure influences enzyme recognition. As illustrated in Figure 3.4A, (spectrum 1), the UV CD spectra [185 - 260 nm] of resting MiaE shows a maximum at 193 nm and two minima at 208 and 222 nm. These features are fairly typical of proteins with high α-helical content. Analysis of the MiaE secondary structure was made by comparison to known protein standards (myoglobin, poly-L-lysine, and lysozyme) as described in *Materials and Methods*. From this analysis, it was determined that resting MiaE α-helical content was 78 ± 5%.

At an equivalent molar concentration relative to MiaE (5 μM) the RNA helical and hairpin loop secondary structure of ACSL^{Trp} (Figure 3.4A, trace 2) contributes to the CD response within this spectral window. While these features are small relative to the protein response, additional controls are needed to ensure that any spectral changes observed are not simply due to non-specific interactions or contributions from the RNA CD spectra.

In the absence of any interactions between the ACSL^{Trp} RNA oligomer and resting MiaE, the expected CD spectra for an equimolar mixture of MiaE and ACSL^{Trp} would be the sum of each spectral contribution (1 + 2). As illustrated in Figure 3.4A (*inset*), the observed spectrum for the MiaE/RNA-complex (trace 3) is significantly different from either initial resting MiaE (trace 1) or the sum of CD spectra (1 + 2; *dashed line*). This result indicates that RNA-binding induces a change in the secondary structure within the MiaE/RNA-complex. To be clear, it is not possible to resolve if the spectral shift observed is solely due to protein- or RNA-conformational changes. In all likelihood it reflects a change in the secondary structure of both molecules upon complexation.

Native tRNA molecules all exhibit a defined hairpin loop secondary structure within the ACSL-region. It is therefore reasonable to speculate that this structural motif may be important for MiaE substrate recognition. To test this hypothesis a 10-nucleotide RNA oligomer incapable of forming a hairpin loop (*referred to as ssRNA*) was added to samples of resting MiaE. While this oligomer is shorter in length than the 17 nucleotide ACSL^{Trp} sequence, it is important to recognize that formation of the hairpin loop decreases the head-tail length of ACSL^{Trp} by nearly two-fold. Thus, the ssRNA sequence lacking this structural motif should be similar in length to ACSL^{Trp}. Indeed, CD spectroscopy confirms the absence of any secondary structure within the ssRNA oligomer. Regardless, no change in the MiaE/RNA-secondary structure is observed by CD (or EPR) spectroscopy in these experiments (*Supporting Information*, Figure S3). This observation suggests that the conformational change induced by complexation of MiaE with ACSL^{Trp} cannot be attributed to non-specific interactions with single stranded RNA. The synthetic nucleosides (ms^{2}i^{6}A, i^{6}A, and Cl^{2}i^{6}A) represent the simplest possible substrates for MiaE in both peroxide shunt and biological electron transfer (Fd/FdR-ETC) assays. As these substrates are unable to elicit a similar conformational change upon addition to resting MiaE (*Supporting Information*, Figure S3), the observed conformational change within the MiaE active site cannot be triggered by a single protein-nucleoside interaction either. On the basis of these experiments, it is reasonable to conclude that the tRNA hairpin loop is a critical point of interaction between MiaE and its tRNA-substrates.

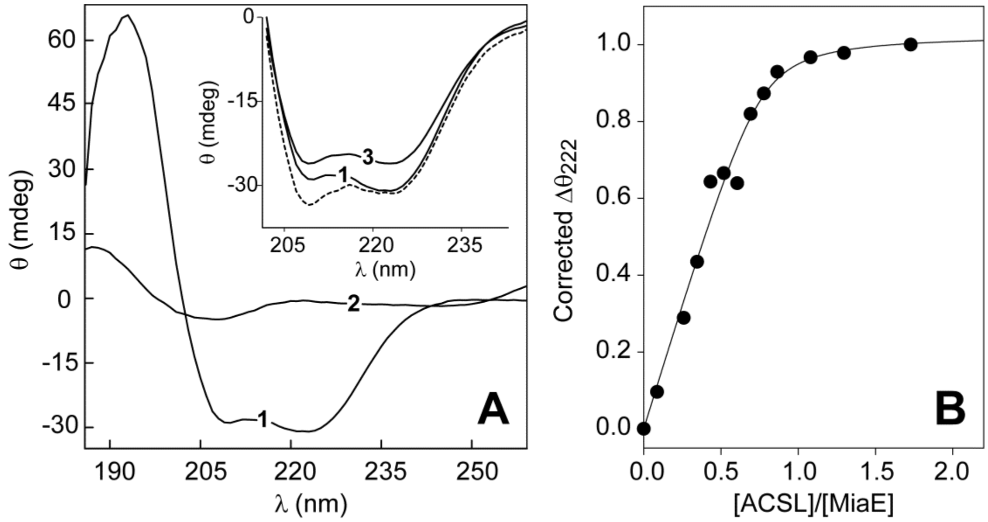

Figure 3.4 CD spectra of MiaE titrated with ACSL^{Trp} A. CD spectra of 5 μM as-isolated MiaE (trace 1) and 5 μM ACSL^{Trp} (trace 2). Within the inset is a replot of the observed CD spectra for an equimolar complex of oxidized MiaE and ACSL^{Trp} (trace 3) as compared to the resting enzyme. Panel B shows the results obtained from titration of the RNA oligomer into a sample of the as-isolated MiaE.

As noted earlier, the RNA secondary structure contributes to the observed CD spectra within the UV-region. These contributions become significant at elevated RNA oligomer concentrations, and thus, they need to be subtracted from the collected data.

Figure S1A of the Supporting Information shows a series of stacked CD spectra for resting MiaE (5 μM) titrated with increasing molar equivalents of ACSLTrp. For each spectrum collected, the signal attributed to free ACSLTrp (trace 2) was scaled for molar concentration and then subtracted from each spectrum collected. The resulting difference spectra shown in Figure S1B were then used to follow formation of the MiaE/ACSLTrp-complex in titration experiments. Within the difference spectra, the absence of the broad absorptive feature (λ = 270 nm) unique to RNA spectra is consistent with the removal of signals associated with unbound ACSLTrp.

As shown in Figure S1B, addition of ACSLTrp into a sample of resting MiaE results in a small but detectible positive shift in the ellipticity at 222 nm ($\Delta\theta222$). At one molar equivalent (ACSLTrp:MiaE), this signal shift is small relative to the total protein signal (~ 4 mdeg at 5 μM MiaE) but is readily detectable. No further changes are observed at this wavelength at titration points beyond one molar equivalent. Figure 3.4B illustrates the normalized $\Delta\theta222$ plotted as a function of ACSLTrp molar equivalents. These results indicate that a single mole of ACSLTrp binds to MiaE to yield a 1:1 stoichiometric complex. Assuming reversible binding of ACSLTrp to that MiaE, the normalized change in ellipticity can be fit using equation 4 to determine an apparent binding constant for ACSLTrp (K_d= 0.3 ± 0.03 μM). It should be noted that the value of binding constant determined from these fits is dependent on the concentration of enzyme utilized in CD titrations. Unfortunately, instrumental signal noise becomes increasingly problematic at protein concentrations below ~3 μM, and thus, these CD experiments are unable to resolve binding affinities below this value ($K_d \leq 3$ μM). As a result, the Kd values determined from CD data fits are likely significantly overestimated. Thus, while CD spectroscopy is ideally suited to observe a conformational change in the MiaE-tRNA complex, more sensitive techniques are needed to accurately evaluate the actual substrate binding affinities for MiaE.

An additional point to consider is whether the oxidation state of MiaE diiron site influences the protein secondary structure or RNA-binding affinity. As indicated by Figure S2 (*Supporting Information*), no difference is observed in the secondary structure of MiaE upon reduction. Furthermore, addition of one molar equivalent ACSLTrp to either form results in identical changes in ellipticity. Titration experiments performed using anaerobic reduced enzyme reveal no significant deviation in the apparent ACSL^{Trp}-binding affinity. While it is likely that the binding affinities differ somewhat between oxidized and reduced enzyme, CD spectroscopy does not have the sensitivity to detect such differences.

EPR Spectroscopy. The diferric (III) active site center of MiaE can be probed by parallel-mode X-band EPR spectroscopy. AS previously reported, the temperature dependence, intensity, line width, and g values of this signal are similar to what has been reported for the reduced diiron sites within several other bacterial non-heme monooxygenase enzymes (DpmLNO, T4MOH, MMOH).(*78*),(*184*) This feature is attributed to the weak ferromagnetic exchange coupling between two high-spin ferrous sites ($S_1 = S_2 = 2$), resulting in a ground state $S = 4$ spin-manifold. The reduced MiaE signal deviates from Curie law behavior in that the temperature dependence of the $g \sim 16$ temperature-normalized signal intensity (S×T) decreases with increasing temperature (*Supporting Information*, Figure S5). The maximal intensity for this signal is observed at 4.2 K and completely vanishes by 25 K. This indicates that this transition must originate from a ground doublet within the lowest-lying spin-manifold of a non-Kramer's system.

Similar ACSL-titrations as described above for CD experiments were performed on reduced diferrous MiaE and followed by dual-mode X-band EPR spectroscopy. As indicated in Figure 3.5A, the line shape for the reduced MiaE (1) *g* ~ 16 signal is significantly altered when pre-complexed with 1.5 molar equivalents of ACSL^{Trp}. Furthermore, Figure 3.5B demonstrates that the extent of change observed in the *g* ~ 16 signal is directly proportional to the amount of ACSL^{Trp} added up to one molar equivalent. Addition of ACSL^{Trp} beyond one molar equivalent has no further effect on the observed *g* ~ 16 EPR spectra of reduced MiaE. In addition to the obvious spectral changes illustrated, ACSL^{Trp}-binding also significantly increases the microwave power needed for half-saturation ($P_{1/2}$) of the *g* ~ 16 signal (Figure 3.5B). As with CD-experiments, addition of the ssRNA sequence had no effect on the observed EPR spectrum for reduced MiaE (*Supporting Information*, Figure S3). This shift in the *g* ~ 16 parallel mode EPR signal upon tRNA-binding to reduced MiaE is very reminiscent to what has been reported for bacterial multicomponent diiron monooxygenases upon titration with their corresponding effector-proteins (26-27, 29, 33, 41-42). This also suggests that MiaE may be an excellent model system to study protein-effector interactions and their impact on diiron site geometry and reactivity.

As described in *Materials and Methods*, EPR simulations (Figure 3.5, *dashed lines*) of the reduced diiron cluster can be generated with the assumption that the magnitude of the ferromagnetic exchange coupling constant (*J*) is comparable or larger in magnitude than the zero-field splitting term (*D*) ($|J| \geq D$).(*78*) Under this constraint, the temperature dependence of the *g* ~ 16 EPR signal becomes solely a function of the axial zero-field splitting term (*D*). This value can be determined experimentally by fitting the temperature-normalized signal area (S × T) to a Boltzmann population distribution for an isolated $S = 4$ manifold. Once the *D*-value is obtained for each signal, the general spin-Hamiltonian can be used to calculate correct EPR transition probabilities (*78, 141, 143*). As illustrated in Figure S5 (*Supporting Information*), both reduced MiaE and MiaE pre-complexed with 1.5

molar equivalents of ACSL$^{\text{Trp}}$ exhibit nearly identical temperature dependence. Both data sets are fit assuming a transition within the ground doublet (levels 1-2) of an $S = 4$ spin-manifold to obtain an axial zero-field splitting of $D = 1.0 \pm 0.2$ cm^{-1}.

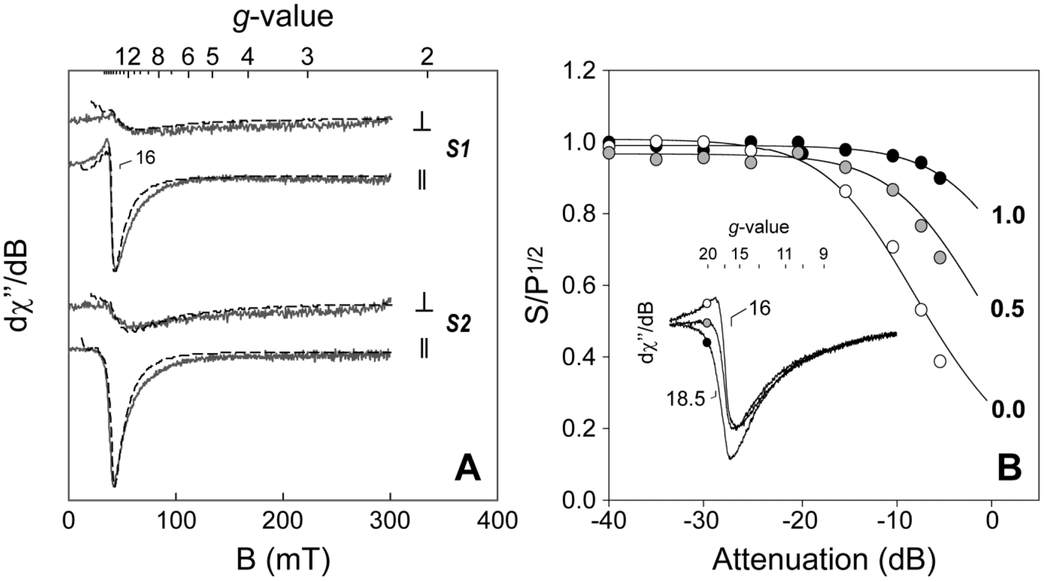

Figure 3.5 X-band perpendicular (⊥) and parallel mode (∥) EPR spectra of reduced MiaE (1) and MiaE pre-complexed with 1.5 molar equivalent of ACSL$^{\text{Trp}}$ (2). EPR simulations (*dashed lines*) are overlaid on the spectra for comparison. (B) Parallel mode g ~16 signal half-saturation microwave power ($P_{1/2}$) for reduced MiaE pre-complexed with 0- ($P_{1/2}$ = 15 mW), 0.5- ($P_{1/2}$ = 76 mW), and 1.0-molar equivalents ($P_{1/2}$ = 300 mW) of ACSL$^{\text{Trp}}$.

X-band EPR spectral simulations were calculated using the experimentally derived zero-field splitting term for both perpendicular and parallel mode frequency polarizations and overlaid on the observed spectra. As shown in Figure 5, both X-band perpendicular and parallel mode EPR spectra for reduced MiaE (1) and MiaE pre-complexed with 1.5 molar equivalent of ACSL$^{\text{Trp}}$ (2) can be reasonably simulated using the parameters described in the caption of Figure 3.5. From these simulations, the spin concentration determined for [*S1*] and [*S2*] are 222 μM (97%) and 240 μM (105%), respectively.

In the previous EPR spectroscopic characterization of reduced MiaE, the spin-quantitation determined by EPR simulation of reduced MiaE was low relative to the expected value (44% relative to the total iron)(*78*). For simplicity, these initial calculations did not account for any intrinsic anisotropy of the diiron *g*-tensor ($g_{x,y,z}$ ~ 2.0). However, parallel mode signals are largely influenced by a single *g*-value within the spin-system (g_y- in this instance). This value was allowed to vary over a reasonable limit for ferrous iron ($2.00 < g_y < 2.15$) while fitting the observed spectra. Essentially stoichiometric quantitation of the reduced MiaE active site is calculated in the overlaid simulation (*S1*) which utilizes the zero-field splitting parameters (D = + 1.0 cm^{-1}; E/D = 0.19). Line width and sigal intensity for this signal is dominated by distributions in D and E/D (σ_D and $\sigma_{E/D}$, resptively). By comparison, the ACSL-bound MiaE simulation (*S2*) suggests that substrate-binding alters the coordination geometry of the reduced active site. While the value of the axial zero-field splitting term remains constant, significant decrease is observed in the rhombicity (E/D = 0.11) calculated for the reduced diiron cluster. For clarity, all spectroscopic parameters used for *S1* and *S2* simulations are provided in the caption of Figure 3.5.

The dual mode EPR simulations accurately reflect signal intensity (*and thus concentration*) of each species (1) and (2) in both perpendicular and parallel mode; however, significant approximations ($|J| \geq D$) were made to limit the number of independent variables necessary for calculations. Complete validation of simulations would require additional dual mode EPR characterization at additional frequencies. In lieu of this, Mössbauer spectroscopy was used to independently corroborate results obtained in EPR spectroscopic experiments and refine UV-visible molar extinction coefficient determinations for this enzyme.

Mössbauer Spectroscopy. As illustrated in Figure 3.6, the Mössbauer spectra (A) for the resting diferric enzyme exhibits three sets of quadrupole doublets designated [1], [2], and [3]. The two nested doublets [2] (δ_2 = 0.53(1) and ΔE_Q = 1.57(2) mm/s) and [3] (δ_3 = 0.49(1) and ΔE_Q = 2.20(2) mm/s) are in equal concentration and collectively represent 84(2)% of the total Fe in the sample. This observation suggests two possibilities: (i.) the majority of the resting MiaE cluster is composed of a single binuclear species containing inequivalent iron sites, or (ii.) two distinct populations of diferric clusters with equivalent iron centers are present within resting MiaE.

Unlike most non-heme diiron proteins, MiaE exhibits a monomeric protein configuration. Thus only one diiron cluster is present per enzyme. As the relative proportion of major doublets [2] and [3] are always equivalent (1:1) across multiple preparations (*oxidized* and *reduced*), it is highly unlikely that these doublets represent two distinct populations of the resting MiaE cluster in chemical equilibrium. Similar behavior has been reported for the diferric active site of hemerythrin, as well as a variety of non-heme diiron model complexes(*140, 185, 186*). The larger ΔE_Q values observed for species [2] and [3] are quite similar to those reported for the μ-oxo bridged diferric clusters in Δ9D and the small subunit of ribonucleotide reductase (R2)(*187, 188*). For comparison, Mössbauer parameters reported for a variety of enzymatic and model diiron site is shown in Table S1. The remaining doublet [1] (δ_1 = 0.50(1) and ΔE_Q = 0.65(1) mm/s) contributes ~15(3)% to the total Fe. The smaller quadrupole splitting observed for [1] is consistent with what has been observed for μ-hydroxo bridged diferric sites within MMOH and T4MOH(*184, 189*). It is therefore reasonable that this doublet originates from a small fraction of MiaE containing a diferric iron site bridged by a μ-hydroxo ligand.

Table 3.1 Observed Mössbauer parameters for MiaE and the ACSL^{Trp}/MiaE complex

Description	Site	δ (mm/s)	ΔEq (mm/s)	Γ	(%)
($Fe^{II}Fe^{II}$)-MiaE					
	1	1.19	2.86	0.57	48
	2	1.32	3.12	0.40	48
($Fe^{II}Fe^{II}$)-MiaE w/ACSL					
	1	1.19	2.79	0.54	46
	2	1.33	3.07	0.40	46
($Fe^{III}Fe^{III}$)-MiaE					
	1	0.50	0.65	0.30	15
	2	0.53	1.57	0.30	42
	3	0.49	2.20	0.30	42
($Fe^{III}Fe^{III}$)-MiaE w/ACSL					
	1	0.51	0.66	0.35	22
	2	0.53	1.55	0.30	39
	3	0.48	2.20	0.30	39

While the relative proportions of these species ([1], [2], and [3]) differ, the Mössbauer parameters observed here are consistent with what has been previously reported for the resting MiaE enzyme with one exception(*87*). In the previous characterization EPR, Mössbauer, and HYSCORE spectroscopic measurements involving resting MiaE, an appreciable fraction (~30%) of the MiaE diiron site was observed as a mixed valent Fe^{II}-Fe^{III} cluster(*87*). In contrast to this observation, no mixed valent species could be detected by either EPR or Mössbauer spectroscopy in the samples prepared here.

The Mössbauer spectrum for MiaE reduced by sodium dithionite and methyl viologen is shown in Figure 3.6B. This spectra is best fit to two unresolved quadrupole doublets [1] (δ_1 = 1.19(3) and ΔE_Q = 2.86(3) mm/s) and [2] (δ_2 = 1.32(3) and ΔE_Q = 3.12(3) mm/s). As with the oxidized doublets, reduced doublets [1] and [2] contribute an equal proportion to the overall spectrum, collectively accounting for 96(4)% of the total Fe in the sample. Both the isomer shift and quadrupole splitting observed for reduced MiaE are similar to those reported for a variety of reduced non-heme diiron centers (*Supporting*

Information, Table S1). The equal contribution of each ferrous doublet [1] and [2] suggests that the individual Fe-sites within the cluster remain inequivalent following reduction of the enzyme.

As indicated by Figure 3.6C, no significant variance is observed in the isomer shift of the two doublets [1] and [2] upon addition of a 1.5-molar excess ACSL^{Trp} to reduced MiaE. This result is expected as isomer shifts are dominated by oxidation state of the Fe-sites. By contrast, the quadruple splitting for each doublet is noticeably decreased (ΔE_Q of 2.79(2) and 3.07(2) mm/s, respectively) upon ACSL^{Trp} addition. This effect is demonstrated by the difference spectra (B-C) illustrated in Figure 3.6D. This observation agrees well with the change in the zero-field splitting parameters (*D* and *E*/*D*) demonstrated by EPR spectroscopy. The effect of ACSL^{Trp} addition was also measured in the resting diferric enzyme, but other than a slight deviation (~+5%) in the composition of the μ-hydroxo doublet [1], both δ and ΔE_Q observed for doubles [2] and [3] were unaffected upon addition of ACSL^{Trp}.

Discussion

As with peroxide-shunt assays (*78*) the product of steady-state assays utilizing the Fd/FdR electron transport chain retains essentially stoichiometric (98%) *E*-stereoselectivity. In contrast to peroxide-shunt and (Fd/FdR-ETC) assays utilizing a single nucleoside, substrate saturation kinetics is only observed for the i^{6}A-ACSL^{Trp}-substrate [k_{cat}, = 0.10 ± 0.01 s^{-1}, K_M = 9.1 ± 1.5 μM]. To our knowledge, this represents the first instance of steady-state kinetic values reported for any tRNA-monooxygenase. While the k_{cat} of MiaE is slow as compared to typical metabolic enzymes (1-10^6 s^{-1}), this value is similar to what has been observed for enzymes involved in modifying genomic DNA (0.1-1.0 s^{-1})(*190*). In such enzymes it has been postulated that the slow reaction rates impart greater accuracy. The experiments described here demonstrate a protein conformational change upon tRNA-binding to MiaE that influences the electronic structure of the diiron site. Moreover, a ~6000-fold increase in catalytic efficiency is observed for RNA i^6A-$ACSL^{Trp}$ substrate as compared to the free i^6A nucleoside. While much of this increased activity can be attributed to increased binding affinity, spectroscopic results suggests that tRNA-binding may provide an activating event in this, and perhaps related, enzymes.

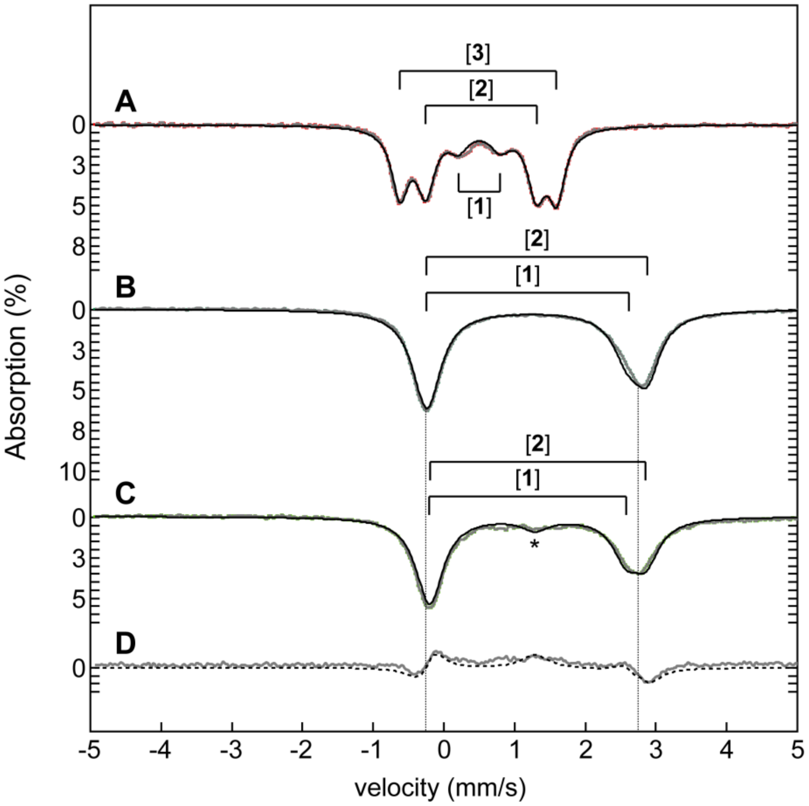

Figure 3.6 Mössbauer spectra of resting diferric (A) and reduced MiaE enzyme (B). Sample conditions: 500 μL 960 μM ^{57}Fe-incorporated MiaE, 20 mM HEPES, 100 mM NaCl, pH 8.0. (C) Reduced MiaE pre-complexed with 1.5 molar equivalents of $ACSL^{Trp}$. The difference spectrum (B-C) and difference fit (*dashed line*) is provided in trace D. The feature designated by (*) is attributed to a trace amount of oxidized MiaE (~10 ± 5%).

Although synthetic nucleosides (ms^2i^6A, i^6A, and Cl^2i^6A) are the simplest substrates for MiaE in both peroxide shunt and (Fd/FdR)-ETC assays(*78*), they do not elicit the same conformational change upon addition to MiaE as observed by CD spectroscopy.

Furthermore, the single stranded RNA oligomer lacking the ability to form a hairpin loop also had no observable effect on either CD or EPR spectra. Taken together, it is reasonable to conclude that the tRNA hairpin loop is a critical point of interaction between MiaE and its tRNA-substrates. Assuming a similar protein structure as observed for other non-heme diiron enzymes, the diiron cluster of MiaE is likely buried within the interior of a four-helix bundle (22, (*191*). Therefore, the spectroscopic perturbations witnessed by both EPR and Mössbauer upon ACSL^{Trp}-addition are unlikely to reflect direct coordination of RNA oligomer to the active site. Instead, tRNA-binding likely results in a protein conformational change in the MiaE structure, which imparts a shift in the diiron active site geometry.

To first-order, validation of EPR spectral simulations can be taken from the accuracy of active site spin quantitation for the reduced MiaE (*S1*) and the reduced MiaE:ACSL^{Trp}-complex (*S2*). On the basis of these calculations, the MiaE protein-conformational change observed by CD spectroscopy is conferred to the MiaE active site resulting in a perturbation to the zero-field splitting parameter (E/D) of the reduced diiron cluster. Another possibility is that ACSL^{Trp}-binding alters the exchange coupling (J) of the cluster. The simulations provided here assume an isolated S = 4 spin-manifold and thus are insensitive to this parameter. The increased half-saturation microwave power observed for *S2* ($P_{1/2}$ = 300 mW) as compared to *S1* ($P_{1/2}$ = 15 mW) indicates faster electronic relaxation rates for *S2*. Potentially, this could be the result of increased m_s-eigenstate mixing within the spin-manifold, however it is not immediately clear if this effect is attributed to changes in the magnitude of the exchange coupling (J) or rhombicity (E/D); potentially it could be a mixture of all both. Regardless, the observed substrate-gated conformational change in the reduced diiron active site alters the geometric configuration of the diiron site, which may in turn alter the Fe$^{II/III}$ redox potential and/or the O_2-reactivity of the substrate-bound enzyme. As the simulations provided here utilize a very simplistic model of the reduced diiron site, the zero-field splitting values reported by simulation should not be considered analytical determinations of these values. Further investigation is necessary to analytically determine the exact impact of this interaction on the active site electronic structure.

On the basis of the small quadrupole splitting ($\Delta E_Q = 0.65$), the ferric doublet [1] shown in Figure 6 (spectra A) is assigned as a set of equivalent Fe-sites bridged by a μ-hydroxo ligand. Similar (μ-hydroxo) doublets have been reported from Mössbauer analysis of as-isolated and reduced Δ9D(*189*), T4MOH(*184*), and DpmLNO (*141*). All known non-heme diiron enzymes containing a μ-hydroxy bridged diiron cluster lack Fe-associated absorption bands(*184*). By this reasoning, the population of MiaE protein containing a μ-hydroxy bridged diferric cluster is not expected to contribute to the observed Fe-associated ligand to metal charge transfer bands within the UV-visible spectrum. Since the molar extinction coefficient previously reported [$\varepsilon_{(370)} = 5{,}100 \pm 700\ M^{-1}\ cm^{-1}$] for resting MiaE was determined on the basis of total iron content, this value is under reported (*78*). By subtracting the fraction of μ-hydroxo bridged MiaE determined by Mössbauer from the concentration of resting MiaE, a corrected molar extinction coefficient can be obtained which is specific to the resting Fe-oxo LMCT at pH 8.0 [$\varepsilon_{(370)} = 5{,}800 \pm 700\ M^{-1}\ cm^{-1}$].

The larger ΔE_Q observed for resting MiaE doublets [1] and [2] (spectra A) is more consistent with μ-oxo bridged diferric clusters (*Supporting Information*, Table S1). The (1:1) contribution of doublets [2] and [3] within the resting MiaE cluster implies that the iron coordination environment for each site is inequivalent. A number of structural factors could give rise to this behavior. For example, an asymmetric coordination of carboxylate or histidine ligands surrounding each iron site, or potentially a terminal hydroxo ligand at one

Fe-site. At this point the exact structural factors giving rise to this inequivalence have yet to be determined.

In agreement with EPR experiments, addition of excess ACSL^{Trp} RNA oligomer to samples of reduced MiaE yields a small but detectable shift (0.05 -0.07 mm/s) in the observed ΔE_Q for doublets [2] and [3] relative to the free reduced enzyme. No effect was observed on the isomer shift (δ) of either the oxidized or reduced enzyme. While the ACSL-induced active site perturbation is not as pronounced in Mössbauer experiments, EPR signal intensity and line shape of integer spin signals are largely dependent on the rhombicity (*E*/*D*) of the system (*143*). Therefore, EPR can frequently be more sensitive to subtle geometric perturbations at the active site as compared to Mössbauer spectroscopy. Regardless, both techniques demonstrate that ACSL^{Trp}-binding imparts a conformational change within the reduced MiaE active site.

CD experiments indicate that protein/RNA conformational changes within the MiaE/ACSL-complex are unaffected by diiron site oxidation state. In apparent contrast to this observation, Mössbauer spectral perturbations are observed only for ACSL^{Trp}-binding to the reduced enzyme. This may suggest that active site conformational changes occur only in the reduced cluster. However, since ΔE_Q-values are 1.4 - 1.8 fold larger in magnitude for the reduced iron sites as compared to the ferric iron sites, a more likely explanation is that these subtle shifts are simply unresolved within the oxidized enzyme.

Nearly all non-heme diiron monooxygenase enzymes exhibit a multimeric quaternary structure. This raises the possibility for inter-protomer communication and potential for '*half-sites*' reactivity(*70-72, 169*). Such factors significantly complicate functional characterization for this class of enzymes. A more practical consideration when dealing with multimeric enzymes is that the active site located within one protomer is spectroscopically indistinguishable from an active site on an adjacent protomer. This generates an inherent ambiguity in assigning spectroscopic features. Thus, despite a wealth of mechanistic and structural studies on non-heme diiron enzymes, to date our fundamental understanding of how the protein environment modulates the reactivity of the diiron cluster remains somewhat superficial. In this respect, MiaE represents an unprecedented opportunity to study a minimal non-heme diiron catalytic system in the absence of any potential for inter-protomer cooperativity. This work provides an important first step in the identification of key intermolecular interactions involved in MiaE catalyzed tRNA hydroxylation. Nevertheless, additional studies are needed to fully model the structural factors influencing enzymatic reactivity, tRNA-specificity, and impact of tRNA-binding on the active site reactivity and electronic structure of MiaE.

The spectroscopic shifts observed for MiaE upon ACSL^{Trp}-binding are reminiscent of the effects reported for bacterial multicomponent diiron monooxygenases upon addition of their corresponding effector-proteins. As the changes observed in the integer-spin EPR signal of the reduced diiron active site are not observed upon addition of the free nucleoside substrate (i^{6}A) or ssRNA sequences, it can be inferred that tRNA-substrate behave as their own effector-molecules for MiaE. To date, this has not been previously reported for any other member of the non-heme diiron monooxygenase family. These observations also imply that substrate-enzyme interactions could play a pivotal role in modulating the reactivity of the MiaE diiron active site. Indeed, beyond the obvious increase in the expected binding affinity for ACSL-substrates relative to free nucleoside substrates, it is tempting to speculate that the vastly increased activity toward RNA-substrates is due to an activating event within the MiaE active site upon substrate-binding.

Chapter 4

Characterization of the ‘Gln-type’ cysteine diooxygenase (Av CDO) from Azotobacter vinelandii: steady-state kinetics and EPR spectroscopy of the substrate-bound iron-nitrosyl active site

Bishnu P. Subedi, Sinjinee Sardar, and Brad S. Pierce, The University of Texas at Arlington

Abstract

Cysteine dioxygenase (CDO) is a non-heme iron enzyme that catalyzes the O_2-dependent oxidation of L-cysteine (L-Cys) to produce cysteine sulfinic acid (CSA). In the mammalian *Mus musculus* enzyme (*Mm* CDO), bidentate coordination of L-cysteine to the mononuclear ferrous iron is stabilized by outer-sphere interactions with a covalently cross-linked cysteine-tyrosine pair (C93–Y157) and a conserved arginine residue (R60) within the active site pocket. By contrast, all known bacterial CDO enzymes lack the Cys-Tyr post-translational modification. Bacterial CDO enzymes are further subdivided as either ‘Arg-‘ or ‘Gln-type’ based on the identity of conserved residues within the active site used for substrate stabilization. In this context, the ‘Arg-type’ bacterial CDO enzymes are most analogous to the mammalian enzymes. As the ‘Gln-type’ CDO enzymes remain mechanistically, kinetically, and spectroscopically uncharacterized, this subset of CDO enzymes offer a unique point of comparison to better understand the role of outer-sphere interactions in thiol dioxygense chemistry. In this work, the annotated ‘Gln-type’ CDO enzyme cloned from the soil bacteria *Azotobacter vinelandii* was purified to homogeneity and was characterized kinetically and by EPR spectroscopy for comparison to the *Mm* CDO enzyme. In steady-state assays using 3-mercaptopropionic acid (3-mpa), L-cysteine

(cys), and cyteamine (ca), the maximal velocity ($k_{cat} = v_0$/[E]) of *Av* CDO is closely matched for each substrate (ranging from 0.2 to 1.0 s^{-1}). However, the observed specificity (k_{cat}/K_M = 18,200 $M^{-1}s^{-1}$) of *Av* CDO is over two orders of magnitude higher for 3-mpa as compared to equivalent reactions with cys (120 $M^{-1}s^{-1}$) and ca (20 $M^{-1}s^{-1}$). These observations suggest that the 'Gln-type' *Av* CDO enzyme has been misannotated as a cysteine dioxygenase and is, in fact, a 3-mercaptopropionic acid dioxygenase (MPDO). Complementary X-band EPR experiments were performed on *Av* CDO using nitric oxide as a surrogate for O_2-binding. As with most non-heme mononuclear iron oxidase/oxygenase enzymes, *Av* CDO exhibits an obligate ordered addition of substrate (3-mpa, cys, and ca) prior to NO. Previously published results demonstrate that the electronic structure of the substrate-bound iron-nitrosyl produced in *Mm* CDO (*Mm* ES-NO) exhibits an unusual $\{FeNO\}^7$ ($S = 1/2$) electronic ground state. In stark contrast to this, the *Av* ES-NO exhibits a $\{FeNO\}^7$ ($S = 3/2$) species (designated *1a'*) with near axial magnetic symmetry ($E/D = 0.009$). The magnitude of the axial zero field splitting term for the iron-nitrosyl species produced within *Av CDO* ($D = 5.0 \pm 0.6$ cm^{-1}), microwave power saturation at 10 K ($P_{1/2} = 11 \pm 3$ mW), and reversibility of NO-binding is similar to what has been reported for other mononuclear non-heme iron $\{FeNO\}^7$ sites. Interestingly, samples of *Av* ES-NO prepared either with cys or ca exhibit a mixture of $\{FeNO\}^7$ ($S = 3/2$) species. One of which is spectroscopically equivalent to *1a'*, whereas the second species (*1b'*) exhibits greater rhombitiy ($E/D = 0.02$). The observed speciation of iron-nitrosyl sites produced using cys and ca suggests that an equilibrium between two substrate-bound structural configurations. Taken together both kinetic and EPR results are consistent with 3-mpa being the native substrate for this 'Gln-type' thiol dioxygenase enzyme.

Introduction

Cysteine dioxygenase (CDO) is a non-heme mononuclear iron enzyme that catalyzes the O_2-dependent oxidation of L-cysteine (Cys) to produce cysteine sulfinic acid (CSA) as shown in Scheme 4.1 (*18, 19*). This enzyme catalyzes the first committed step in Cys catabolism, thus it is central to sulfur metabolism and redox homeostasis. Enzymes involved in sulfur-oxidation and transfer are increasingly being recognized as potential drug targets for development of antimicrobials, therapies for cancer, and inflammatory disease(*192-195*). For instance, patients suffering from neurological disorders such as autism and Down syndrome have significantly lower plasma concentration of transsulfuration pathway and methionine cycle products [cysteine (Cys), homocysteine (Hcy), glutathione (GSH), and S-adenosylmethionine (SAM)](*196, 197*). In fact, imbalances in Cys metabolism have also been identified in a variety of other neurological disorders (motor neuron disease, Parkinsons, and Alzheimers)(*19, 198, 199*). These observations suggest a potential correlation between impaired sulfur metabolism, oxidative stress, and neurodegenerative disease(*196*).

Scheme 4.1 Oxygen dependent formation of cysteine sulfinic acid (CSA) catalyzed by cysteine dioxygenase (CDO)

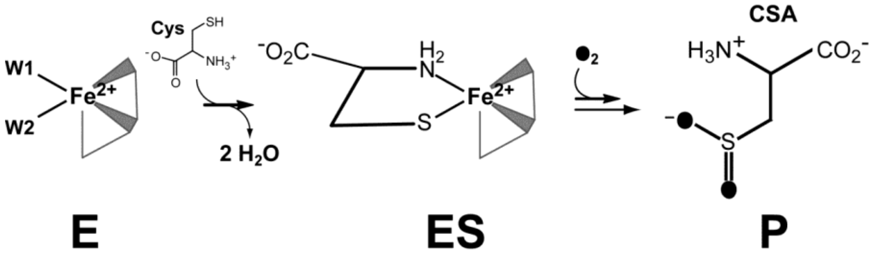

In contrast to the canonical 2-His-1-carboxylate facial triad motif exhibited by nearly all non-heme mononuclear iron enzymes, the active site of mammalian CDO is comprised of a neutral 3-His facial triad. Multiple high-resolution crystal structures of the resting and substrate-bound enzyme have been solved which highlight the atypical mononuclear iron coordination for the mammalian CDO active site(*21-25*). As illustrated in Figure 4.1A, the active site coordination of the *Rattus norvegicus* CDO (pdb code 4IEV) is comprised of iron ligated by the N_ε-atoms of His86, His88, and His140, representing a new 3-His variant on the classic 2-His-1-carboxylate facial triad observed in mononuclear non-heme iron enzymes(*26*). To date only 2 enzymes with a 3-His facial triad motif (CDO and diketone dioxygenase, Dke1) have been crystallographically(*200*) and spectroscopically characterized(*28, 29*). On the basis of sequence homology, it has been proposed that the active site of mammalian cysteamine (2-aminoethanethiol) dioxygenase (ADO) also contains a 3-His facial triad(*30*). Another unusual feature within the mature eukaryotic CDO active site is a post-translational modification 3.3 Å from the Fe-center in which spatially adjacent Cys93 and Tyr157 residues are covalently crosslinked to produce a C93-Y157 pair. Among CDO enzymes identified, Y157 is conserved across phylogenic domains, whereas the C93-Y157 pair is unique only to eukaryotes. It has been proposed that that the C93-Y157 pair facilitates appropriate substrate orientation and stereoselectivity. The bidentate substrate coordination provides two points of simultaneous interaction. A third point of interaction is produced by hydrogen bonding between the Cys-carboxylate group and the C93-Y157 pair (2.94 Å). This third interaction is also stabilized electrostatically by interaction with R60 (separated by 2.91 - 3.16 Å). Collectively, these interactions satisfy the "*three point interaction rule*" for chiral selection(*38, 201*). The exact mechanism of C93-Y157 formation remains unresolved.

By contrast, all known bacterial CDO enzymes lack the Cys-Tyr post-translational modification. Furthermore, sequence homology suggests an additional subset of CDO enzymes, which lack the conserved R60 residue. To illustrate, the crystal structure for the putative CDO isolated from *Ralstonia eutropha* (pdb code 4QMA) is shown in Figure 4.1B. Of note, the 3-His facial triad motif is conserved, however the outer-sphere Arg-residue involved in substrate stabilization is replaced by Gln (Q67). All other conserved residues (Figure 4.1A; H155, Y157, Y58) within the active site are essentially conserved, thus bacterial CDO enzymes have been subdivided as either ‘Arg-‘ or ‘Gln-type’ depending on which residue is involved in substrate stabilization(*202*). In this context, the ‘Arg-type’ bacterial CDO enzymes are most analogous to the mammalian enzymes. Interestingly, it has been noted that the recently characterized 3-mercaptopropionate dioxygenase (MPDO) isolated from *Variovorax paradoxus* shares higher sequence homology with the so-called ‘Gln-type’ CDO enzymes(*31*). Thus calling into question the accuracy these annotated ‘Gln-type’ CDO enzymes. As the ‘Gln-type’ CDO enzymes remain mechanistically, kinetically, and spectroscopically uncharacterized, this subset of enzymes offer a unique point of comparison to better understand the role of outer-sphere interactions in thiol dioxygense chemistry.

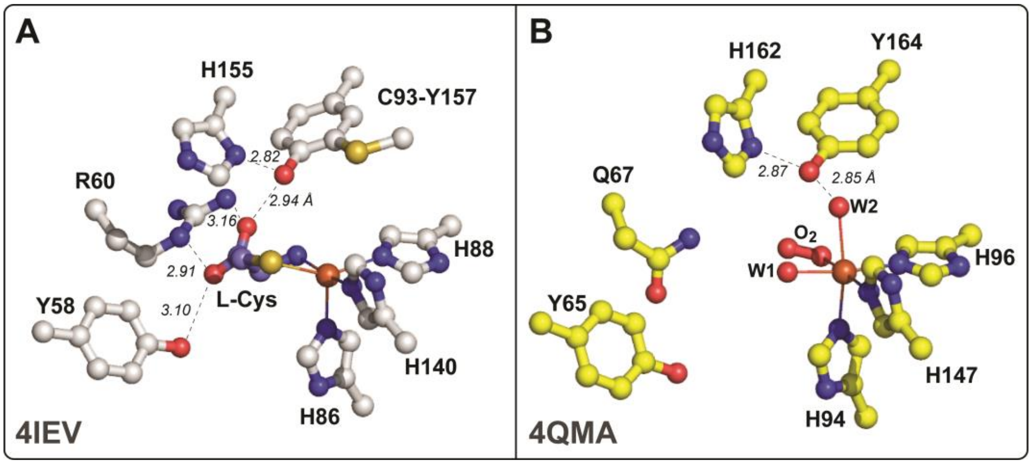

Figure 4.1 Crystal structure of the substrate-bound *Rattus norvegicus* CDO active site (A, pdb code 4IEV) as compared to the annotated ‘Gln-type’ CDO

In this work, the initial characterization of a putative 'Gln-type' CDO cloned from the gram-negative soil bacteria *Azotobacter vinelandii* (*Av* CDO) is presented. The pH-dependent Michaelis-Menten kinetics was monitored in reactions using 3-mercaptopropionic acid (3-mpa), L-cysteine (cys), and cyteamine (ca) as a substrate. Curiously, in equivalent reactions using cys, both k_{cat}, k_{cat}/K_M of *Av* CDO are closely matched to values obtained for *Mm* CDO suggesting that this enzyme may indeed function physiologically as a cysteine dioxygenase enzyme. However, the observed specificity is over two orders of magnitude higher for 3-mpa (18,200 $M^{-1}s^{-1}$) as compared to equivalent reactions with cys (120 $M^{-1}s^{-1}$) and ca (20 $M^{-1}s^{-1}$). These results suggest that the so-called 'Gln-type' *Av* CDO is misannotated, is more accurately described as a 3-mercaptopropionic acid dioxygenase (MPDO) enzyme.

Complementary X-band EPR experiments using nitric oxide as a surrogate for O_2-binding also support this conclusion. As with most non-heme mononuclear iron oxidase/oxygenase enzymes, *Av* CDO exhibits an obligate ordered addition of substrate (3-mpa, cys, and ca) prior to NO. However, only with 3-mpa is a single iron-nitrosyl species produced upon addition of nitric oxide to the substrate-bound enzyme. Equivalent samples prepared using either cys or ca yield a mixture of $\{FeNO\}^7$-species, suggesting an equilibrium between two substrate-bound configurations. Moreover, the spin state observed for the substrate-bound $\{FeNO\}^7$-species produced in *Av* CDO (designated *Av* ES-NO) is completely divergent from what is observed for *Mm* CDO. Previously published results demonstrate that the *Mm* ES-NO exhibits an unusual {FeNO}7 (S = 1/2) electronic ground state whereas the *Av* ES-NO is the more common observed intermediate spin (S = 3/2) $\{FeNO\}^7$ configuration. Collectively, these results suggest significant deviations in substrate-coordination, substrate-specificity, and electronic structure of the substrate-bound iron-nitrosyl produced in *Mm* CDO and 'Gln-type' thiol dioxygenase enzymes.

Materials and methods

Expression of Av CDO. The isopropyl β-D-1-thiogalactopyranoside (IPTG) inducible T7 vector (designated pRP42) was a generous gift from Professor Tim Larson (Virginia Tech, Department of Biochemistry). This vector expresses *Av* CDO with a C-terminal $(His)_6$-affinity tag and a recognition sequence for thrombin protease such that the affinity tag can be removed following purification. Sequence verification of *Av CDO* was performed by Sequetech (Mountain View, CA, http://sequetech.com/). The pRP42 vector was transformed into into competent BL21(DE3) *E. coli* cells (Novagen cat. no. 70236-4) by heat shock and plated for overnight growth at 37 °C on an LB-agar plate containing 100 mg/L ampicilin (Amp). The following day, a single colony was selected for growth in liquid LB (Amp) media for training on antibiotic prior to inoculation of a 10-L BF-110 fermentor (New Brunswick Scientific) at 37 °C. Cell growth was followed by optical density at 600 nm (OD_{600}). Cells were induced by addition of 0.5 mM IPTG, 20 g casamino acids, and 40 μM ferrous sulfate at an OD_{600} ~4. At the time of induction the temperature of the bioreactor was decreased from 37 °C to 25 °C and agitation was set to maintain an O_2 concentration of 20% relative to air-saturated media. After 4 hours the cells were harvested by centrifugation (Beckman-Coulter Avanti J-E, JA 10.5 rotor) at 18,600 × g for 15 min, and the paste was stored at -80 °C. Confirmation of *A*v CDO expression was performed by SDS-PAGE of lysed cells before and after induction.

Enzyme purification. In a typical preparaton, 20 g of frozen pelleted cells was thawed by slowly on ice by addition of 30 mL of HEPES buffer (20 mM HEPES, 50 mM NaCl, pH 8.0). To this suspension, lysozyme, deoxyribonuclease, and ribonucease I was added to a final concentration of 10 μg/mL each and allowed to react for 30 min. Following enzymatic digestion, the suspension was sonicated for 15 sec on/off pulse cycle for a total time of 10 min. Insoluble cell debris was removed from by centrifugation for 1 hour at 4 °C (48,000 x g). The cell free extract was loaded into DEAE fast flow anion exchange column [7 cm D x 20 cm L] pre-equilibrated in 20 mM HEPES, 50 mM NaCl, pH 8.0. The column was washed with three column volumes of the HEPES buffer prior to elution by NaCl gradient (50-350 mM) at pH 8.0. Fractions (10 mL) were collected overnight and pooled based on CDO activity as described elsewhere(*203*) and the presence of the recombinant protein (~24 kDa) as determined by SDS PAGE. Broad range protein molecular weight markers utilized in SDS PAGE experiments were purchased from Promega (Madison, WI) Cat. No. V8491. The pooled fractions were concentrated to approximately 5-10 mL using an Amicon stir cell equipped with an YM-10 ultrafiltration membrane. Thrombin protease (Biopharma Laboratories) was added to cleave the C-terminal His-tag from *Av* CDO. In a typical reaction, ~0.3 molar equivalents of thrombin per *Av* CDO (based on UV-visible absorbance at 280 nm) was added to batches of purified protein for overnight cleavage at 4 °C in HEPES buffer. Remaining thrombin and free $(His)_6$-tag was removed from *Av* CDO by size exclusion chromatography using a sephacryl S100 column. The ferrous and ferric iron content within *Av* CDO was assayed spectrophotometrically for all batches of enzyme used in these experiments as described previously.(*204*) (*205*) For clarity, the concentrations reported in enzymatic assays reflect the concentration of ferrous iron within samples of *Av* CDO (Fe^{II}-CDO). Protein content was determined by Bio-Rad protein assay.

Enzyme assays. Cysteine sulfinic acid (CSA) was assayed using the HPLC method described previously(*21, 25*). Instrumental conditions: Column, Phenomenex C18 (100 mm x 4.6 mm); Mobile phase, 20 mM sodium acetate, 0.6 % methanol, 1 % heptaflurobutyric acid, pH 2.0. Analytes were detected spectrophotometrically at 218 nm. Reactions (1 mL) were prepared in a buffered solution at the desired pH to obtain a final concentration from 0.1 to 60 mM L-cysteine. The composition of reaction buffers for all pH-profile experiments consisted of 20 mM Good's buffer and 50 mM NaCl. 2-(*N*-

morpholino)ethanesulfonic acid (MES) was used to buffer reactions over the pH range of 6.0 - 6.9 and 2-[4-(2-hydroxyethyl)piperazin-1-yl]ethanesulfonic acid (HEPES) was used to buffer reactions over the pH range of 7.0 - 8.5. 2-(Cyclohexylamino)ethanesulfonic acid (CHES) was used to buffer reactions over the pH range of 8.5 – 10. Each reaction was initiated by addition of 0.5 mM Av CDO at 25 ± 2 °C. Sample aliquots (250 µL) were removed from the reaction vial at selected time points (1, 2, and 3 minutes) and quenched by addition of 10 µL 1 N HCl (final pH 2.0) followed by spin-filtration (0.22 µm cellulose acetate membrane; Corning, Spin-X (0.22 µM)) prior to HPLC analysis. The concentration of CSA produced was determined by comparison to calibration curves as described elsewhere. The rate of dioxygen consumption in CDO activity assays was determined polarographically using a standard Clark electrode (Hansatech Instruments, Norfolk, England) in a jacketed 2.5 mL cell. Calibration of O_2-electrode is described in detail elsewhere.(*40, 206*) As with HPLC assays, all reactions were initiated by addition of 0.5 mM *Av* CDO under identical buffer conditions as described for HPLC assays. Reaction temperatures were maintained at 25 ± 2 °C by circulating water bath (ThermoFlex 900, Thermo Scientific).

Data Analysis. Steady-state kinetic parameters for CDO were determined by fitting data to the Michaelis-Menten equation using the program SigmaPlot ver. 11.0 (Systat Software Inc., Chicago, IL). The pH-dependences of steady state kinetic parameters (k_{cat} or k_{cat}/K_M) for *Av* CDO is '*bell shaped*' in that they decreases at both low and high pH values. Therefore the data were fit to equation (1).(*207, 208*) Here, [H], K_1, and K_2 represent the hydrogen ion concentration and the two observable dissociation constants for ionizable groups involved in catalysis, respectively. This expression is scaled by a constant scalar quantity (C) which represent the maximum kinetic rate (k_{cat} or k_{cat}/K_M).

Equation 1. $$\log Y = log\left(\frac{C}{1+\frac{K_2}{[H]}+\frac{[H]}{K_1}}\right)$$

Alternatively, k_{cat}- or k_{cat}/K_M -pH profiles approaches limiting values (Y_L and Y_H) at low and high pH, and thus data were fit to equation (2) as described elsewhere.(*206-208*)

Equation 2. $$\log Y = log\left(\frac{Y_L+Y_H\cdot\frac{K_1}{[H]}}{1+\frac{K_1}{[H]}}\right)$$

Anaerobic work. All anaerobic samples were prepared in a glove box (Coy Laboratory Products Inc., Grass City, MI) with the O_2 concentration maintained below 1 ppm. Solutions were degassed on a Schlenk line prior to transferring into the anaerobic chamber. Analytical grade argon was passed through a copper catalyst (Kontes, Vineland, N.J.) to remove trace O_2 impurities and then sparged through distilled water to hydrate the gas.

Physical Methods. All UV-visible measurements were made on an Agilent 8453 photo diode array spectrometer (Santa Clara, CA). Sample temperature was held constant by a 13 L circulating water bath and a thermostable cell holder (89054A) with magnetic stirrer. Measurements were made in ES Quartz cuvettes (NSG Precision Cells, Farmingdale, NY). X-band (9 GHz) EPR spectra were recorded on a Bruker (Billerica, MA) EMX Plus spectrometer equipped with a bimodal resonator (Bruker model 4116DM). Low-temperature measurements were made using an Oxford ESR900 cryostat and an Oxford ITC 503 temperature controller. A modulation frequency of 100 kHz was used for all EPR spectra. All experimental data used for spin-quantitation were collected under non-saturating conditions.

Analysis of the EPR spectra utilized the general spin Hamiltonian, Equation 3 $$\hat{H} = D\left(\hat{S}_Z^2 - \frac{S(S+1)}{3}\right) + E\left(\hat{S}_X^2 + \hat{S}_Y^2\right) + \beta \mathrm{B} \cdot g \cdot S$$

where *D* and *E* are the axial and rhombic zero-field splitting (*zfs*) parameters and *g* is the *g*-tensor(*118*). EPR spectra were simulated and quantified using Spin Count (ver. 5.4.5414.16762), written by Professor M. P. Hendrich at Carnegie Mellon University. The simulations were generated with consideration of all intensity factors, both theoretical and experimental, to allow for determination of species concentration. The only unknown factor relating the spin concentration to signal intensity was an instrumental factor that is specific to the microwave detection system. However, this was determined by a spin standard, Cu(EDTA), prepared from a copper atomic absorption standard solution purchased from Sigma-Aldrich.

*Nitric oxide additions. All s*amples of *Av* CDO used for EPR experiments were prepared at ~300 mM in ferrous iron. To ensure complete binding of L-Cys substrate and substrate-analogues (cysteamine and 3-mercapto propionic acid) a 15-fold molar excess was added to each sample and allowed to equilbrate for 20 min. Stoichiometric additions of nitric oxide were made by addition of a NO saturated buffer as previously described(*37*). The reversibility of NO-binding to the substrate-bound *Av* CDO was demonstrated by anaerobically thawing EPR samples under an argon atmosphere on a Schlenk line. Once thawed, the samples were exposed to a tungsten white light source collimated through a 250 mL round bottom flask contianing water for 10 min before gently exchaning the sample head space with fresh argon. This process was repeated 3 times prior to refreezing the sample for EPR analysis.

Results

Purification of Av CDO. Recombinant CDO from *Azotobacter vinelandii* (*Av* CDO) was purified and assayed for Fe-content as described in *Materials and Methods*. As indicated by the SDS PAGE shown Figure 4.2, the IPTG-inducible [lanes 2(-) and 3(+)] *Av* CDO protein exhibits an apparent molecular weight of ~23 kDa. Fractions of *Av* CDO were pooled on the basis of activity (TLC)(*47*) and SDS PAGE and treated with thrombin overnight at 4 °C to remove C-terminal $(His)_6$-tag (lane 5). In most instances, SDS PAGE was able to resolve a subtle decrease in the the observed molecular weight of the $(His)_6$-tagged *Av* CDO (lane 4) and the thrombin cleaved enzyme (lane 5).

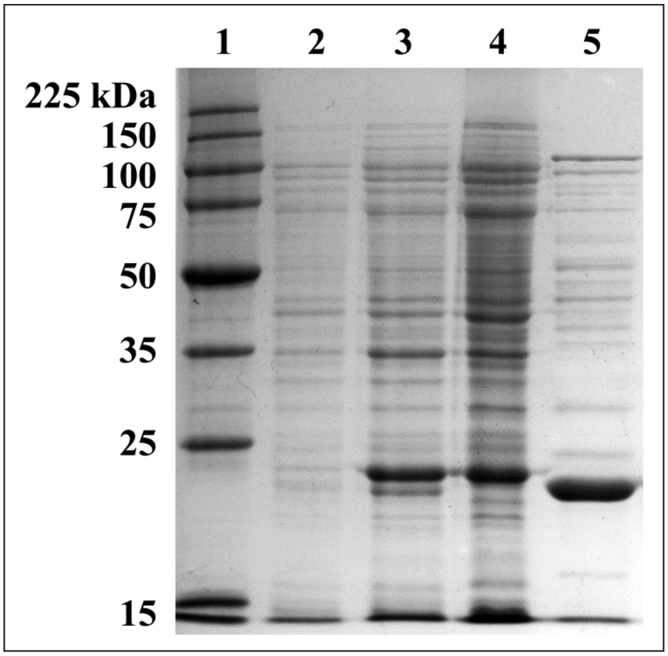

Figure 4.2 SDS PAGE (12 %) of sequential *Av* CDO purification steps. Lane: 1, protein markers; 2, pre-IPTG induced; 3, post-IPTG induced; 4, cell free extract; 5, thrombin-cleaved

Unlike its mamallian counterpart, the *Av* CDO enzyme lacks the C93-Y157 post-transcriptional modification and thus a single band is observed for the isolated enzyme. The molecular weight of *Av* CDO observed by SDS PAGE (~23 kDa) is consistent with the value expected from the amino acid sequence (22,696.51 Da). The stoichiometry of iron per *Av* CDO protein was determined by TPTZ, Bradford assay, and UV-visible spectroscopy as described previously(*37*). In multiple enzyme preparations, the average iron content is 0.8 ± 0.1 mol iron per *Av* CDO. Similar to *Mus musculus* (*Mm* CDO), nearly all 83 ± 13 % of the iron observed is in the catalytically relevant Fe(II) state.

Steady-state kinetics of Av CDO catalyzed reactions. Both O_2-consumption and CSA formation were measured using a calibrated Clarke-type O_2-electrode and reverse-phase HPLC as described previously(*40, 206*). For all steady-state assays, the observed initial rate was normalized by the concentration of ferrous iron in *Av* CDO (v_0/[E]). The values for k_{cat} and K_M were obtained at 25 ± 2 °C from fitting the data to the standard Michaelis-Menten equation. The steady-state kinetics for *Av* CDO with L-Cys is shown in Figure 4.3 (panel B). The dashed line represents a best-fit to the initial rate of O_2-consumption (*open circle*). From this analysis, the values of k_{cat} and K_M were determined to be 1.0 ± 0.04 s^{-1} and 8.6 ± 0.8 mM for the steady-state rate of O_2-consumption, respectively. In terms of O_2-consumption, the catalytic efficiency (k_{cat}/K_M) of this enzyme is 120 ± 14 $M^{-1}s^{-1}$. By comparison, the initial rate for CSA formation (*closed circles*), k_{cat} and K_M were determined to be 0.9 ± 0.1 s^{-1} and 13.5 ± 0.9 mM, respectively (k_{cat}/K_M = 90 ± 6 $M^{-1}s^{-1}$). The (CSA/O_2)-coupling efficiency is defined as the ratio of the k_{cat} for CSA formation divided by the k_{cat} for O_2-consumption (90 ± 6%). Additional steady-state *Av* CDO assays were performed using alternative thiol-bearing substrates of comparable size to L-cysteine [cysteamine (2-aminoethanethiol) and 3-mercaptopropionate]. Surprisingly, as illustrated in Figure 4.3A, steady-state assays for 3-mpa as a potential substrates exhibit significantly decreased K_M relative to L-cysteine. In steady-state assays using 3-mercaptopropionic acid (3-mpa), L-cysteine (cys), and cyteamine (ca), the maximal velocity (k_{cat} = v_0/[E]) of *Av* CDO is closely matched for each substrate (ranging from 0.2 to 1.0 s^{-1}). However, the observed specificity (k_{cat}/K_M = 18,200 $M^{-1}s^{-1}$) of *Av* CDO is over two orders of magnitude higher for 3-mpa as compared to equivalent reactions with cys (120 $M^{-1}s^{-1}$) and ca (20 $M^{-1}s^{-1}$). From these results, we conclude that 3-mpa is the physiologically relevant substrate.

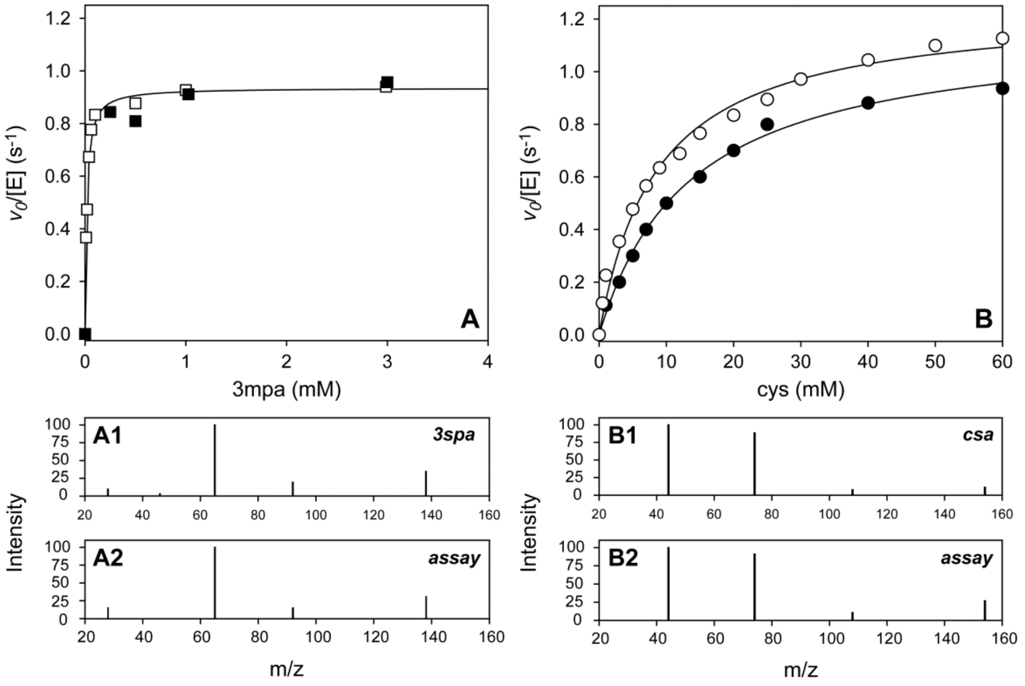

Figure 4.3 Steady state kinetics of *Av* CDO catalyzed 3MPA (A, *square*) and CSA (B, *circle*) formation. LC-MS/MS spectra of 3MPA and CSA MRM transitions of designated product ions are shown within the lower panels for comparison (the middle panel corresponds to the standard and the lower panel illustrates the peaks obtained from enzymatic assays)

CSA product formation was confirmed using multiple reaction monitoring (MRM) as described in *Materials and Methods*. In these experiments, the $[M+H]^+$ molecular ion for CSA (154 m/z) was selected for secondary fragmentation. The optimized MRM method was used to verify sulfinic acid product by direct injection of enzymatic assays (Figure 4.3, *panel* B1). The data obtained were then compared to direct injection of a CSA standard (*panel* B2) to confirm product identity. In addition to the 154 m/z parent $[M+H]^+$ ion, three additional ions are observed at 44, 74, and 108 m/z. The fragmentation pattern and relative intensities observed in enzymatic reactions exactly match those observed in CSA standard. The product of 3-mpa dioxygenation was also confirmed similarly by MRM method as shown in Figure 4.3 A1 and A2.

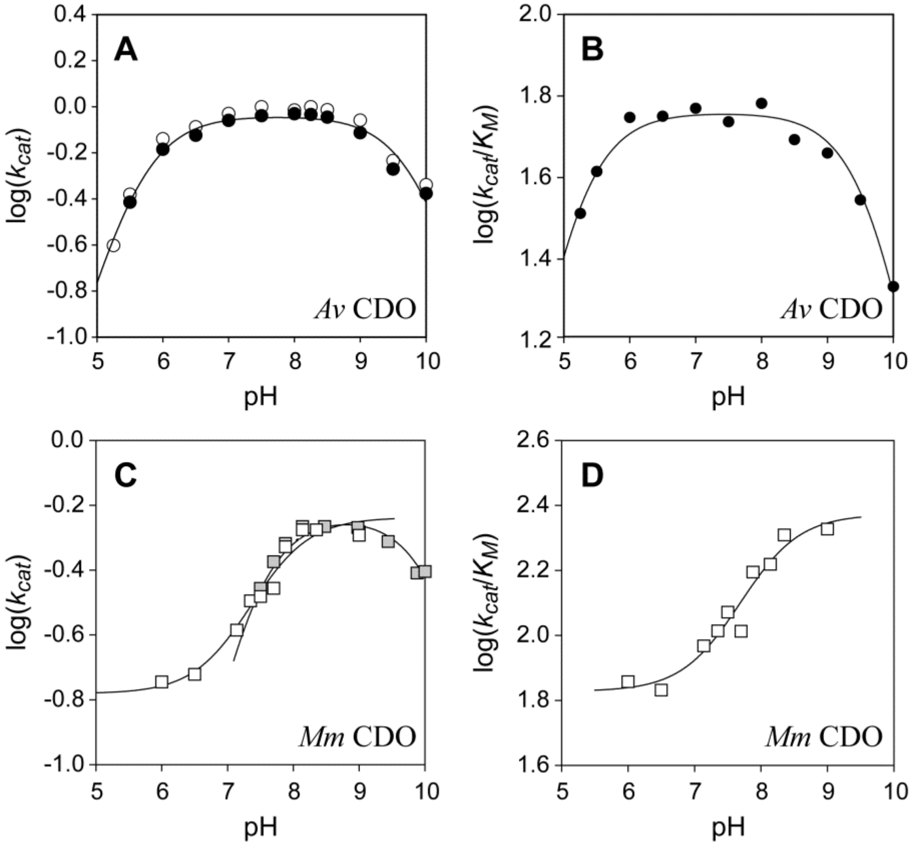

Figure 4.4 Comparison of pH-dependence of k_{cat} (A) and k_{cat}/K_M (B) for *Av* and *Mm* CDO. The maximum rate determined [v_0/[E] = k_{cat}] observed for both O_2-consumption (*white circles*) and CSA formation (*black circles*) are shown in panal A to illustrate the coupling efficiency of *Av* CDO. The k_{cat}/K_M data shown indicated by *black squares* in panel B. The pKa values obtained from k_{cat}-pH and k_{cat}/K_M-pH profiles (shown in Table 4.1) were determined by best fit of data to equations 1 and 2. For direct comparison, the pH-profile for *Mm* CDO k_{cat} and k_{cat}/K_M is re-ploted in panals C and D, respectively. A summary of steady-state kinetic parameters determined for *Av* CDO and *Mm* CDO is shown in Table 4.1

Additional mechanistic insight into ionizable groups involved in catalysis can be obtained from the pH-dependence on both k_{cat} and k_{cat}/K_M. The influence of pH on k_{cat} and k_{cat}/K_M for *Av* CDO was measured over the accessible pH range of the enzyme (5.5 < pH < 10). Figure 4.4 illustrates the k_{cat}- (A, *circles*) and k_{cat}/K_M -pH profiles (B, *squares*) obtained from the initial rate data of *Av* CDO. As with the steady-state curve shown in Figure 4.3, the value of k_{cat} was determined for both O_2-cosumption (○) and CSA formation (●) to establish the pH dependence on (CSA/O_2)-coupling. Both pH-profiles [log(k_{cat}) and log(k_{cat}/K_M)] exhibit a bell shaped curve with two resolved pKa values. One interesting observation is that the *Av* CDO exhibits a much broader pH-independent plateau as compared to *Mm* CDO.(*206*) Moreover, the (CSA/O_2)-coupling is essentially stoichiometric over the entire pH range assayed. The data were fit to equation (1) (*solid lines*) by method of least squares to obtain the observed pKa values for ionizable groups involved in catalysis. From this analysis, two pKa-values are obtained (5.64 ± 0.06 and 9.86 ± 0.06) was obtained from the k_{cat}-pH profile in reactions at 25 °C. The maximal k_{cat} value obtained pH-profile fitting is 0.93 ± 0.03 s^{-1}. Similarly, two pKa values were obtained from fitting the k_{cat}/K_M-pH data (5.11 ± 0.07 and 9.74 ± 0.07), which are quite comparable to what is observed for in the k_{cat}-pH profile.

We previously demonstrated that *Mm* CDO exhibits a single ionizable inflection point (pKa 7.4 ± 0.1) within the k_{cat}-pH profile within the pH range of 6-9(*206*). Within the same pH range, a single pKa value (7.9 ± 0.2) can be observed within the k_{cat}/K_M-pH data. The log(k_{cat}) and log(k_{cat}/K_M) data begins at a limiting minimum value and then increases to a maximum limiting value at elevated pH. However, if additional measurements are made up to pH 10 (Figure 4.4C, *gray squares*), k_{cat} values begin to degrease with increasing pH suggesting a second ionizable pKa of (10.30 ± 0.2)(*40*). Based on the k_{cat}-pH profile, the optimal pH for *Mm* CDO is 8.2. The limited stability of *Mm* CDO above pH

9 significantly increases the variability of K_M-values obtained and thus this data is omitted. A direct comparison of the pH-profile obtained from *Av* CDO and *Mm* CDO is shown in Figure 4.4 (panel C and D) and a summary of the steady-state kinetic parameters obtained for each enzyme is provided in Table 4.1.

Finally, as the *Av* CDO enzyme has not been previously characterized, the optimal temperature for this enzyme was determined. For simplicity, only the initial rate of O_2-consumption was measured as (CSA/O_2)-coupling is essentially stoichiometric. In these reactions, a saturating concentration of L-Cys was introduced to enzyme pre-incubated for 2 minutes at selected temperatures ranging from 15 - 45 °C. As illustrated by Figure 4.5, the observed data follows a typical Gaussian '*bell shaped curve*' with an optimal temperature of 34.8 ± 0.3 °C. The maximal specific activity (v_0/[E]) at this temperature is ~ 2.0 s^{-1}.

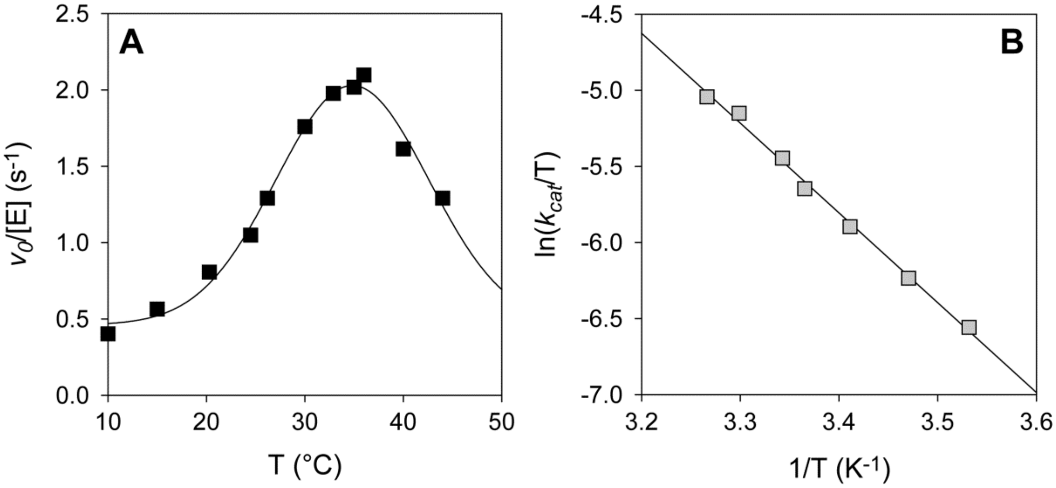

Figure 4.5 Temperature dependence (A) and Eyring Plot (B) of *Av* CDO catalyzed product formation. For all reactions, the enzyme (1 μM) was allowed to incubate at temperature for 2-minutes prior to initiation of reaction by addition of substrate.

Table 4.1 A summary of the steady-state kinetic parameters obtained for each enzyme

	kinetic	Substrate			
Enzyme	parameter	cys	3MPA	ca	*ref*
Av CDO (25 °C)	k_{cat} (s^{-1})	1.0 ± 0.1	0.9 ± 0.1	0.18 ± 0.02	*here*
	K_M (mM)	11.4 ± 0.9	0.02 ± 0.01	10 ± 3	
	k_{cat}/K_M (M^{-1} s^{-1})	110 ± 20	45,000 ± 5700	20 ± 5	
	Coupling (%)	92 ± 6	104 ± 6	not observed	
	pH optimum	8.2	8.18	not observed	
	log(k_{cat})				
	pKa_1	5.64 ± 0.06	7.79±0.11	-	
	pKa_2	9.86 ± 0.06	9.52±0.05	-	
	log(k_{cat}/K_M)				
	pKa_1	5.11 ± 0.07	7.84±0.12	-	
	pKa_2	9.74 ± 0.05	8.14±0.16	-	
Mm CDO (20 °C)	k_{cat} (s^{-1})	0.6 ± 0.1	no activity	*not observed*‡	(*201, 206*)
	K_M (mM)	2.3 ± 0.3	-	*not observed*‡	
	k_{cat}/K_M (M^{-1} s^{-1})	260 ± 30	-	< 0.01	
	Coupling (%)	76 ± 7	-	< 1%	
	pH optimum	8.6	no activity	*not observed*	
	log(k_{cat})				
	pKa_1	7.42 ± 0.1	-	-	
	pKa_2	10.30 ± 0.08	-	-	
	log(k_{cat}/K_M)				
	pKa_1	8.0 ± 0.2	-	-	
	pKa_2	n/a	-	-	

EPR Spectroscopy of substrate-bound iron-nitrosyl Av CDO (Av ES-NO). Addition of nitric oxide (NO) to a substrate-bound mononuclear non-heme iron center typically results in the formation of a $\{FeNO\}^7$ ($S = 3/2$) species characterized by an axial EPR spectrum ($g_{x,y,z}$ ~ 4, 4, 2). According to the Feltham–Enemark notation, the ground state $S = 3/2$ spin-manifold can be described by an antiferromagnetic coupling between a high-spin Fe^{III} ($S = 5/2$) and a bound NO^- anion ($S = 1$)(*209-211*). In contrast to this, addition of NO to the substrate-bound *Mm* CDO (*Mm* ES) produces an anisotropic $S = 1/2$ EPR signal with observed *g*-values of 2.07, 2.03, and 1.96(*37*). For comparison, complementary experiments were performed using CDO enzyme isolated from the soil bacteria *Azotobacter vinelandii* (*Av* CDO). In these studies, samples of the free *Av* CDO and substrate-bound *Av* CDO (*Av* ES) were treated anaerobically with nitric oxide to determine if the bacterial enzyme also exhibits an obligate ordered addition of L-Cys prior to NO (and presumably O_2). In the absence of L-Cys, no appreciable $\{FeNO\}^7$ ($S = 1/2$) or ($S = 3/2$) signals were observed by EPR upon stoichiometric addition of NO (*data not shown*). Thus, similar to the mammalian enzyme, the ferrous iron active site of *Av* CDO appears to have poor NO-binding affinity in the absence of substrate. However, addition of NO to *Av* CDO pre-complexed with excess L-Cys (10 molar equivalents relative to enzyme) produces the $\{FeNO\}^7$ ($S = 3/2$) species shown in Figure 4.6.

The EPR spectra for substrate-bound $\{FeNO\}^7$ *Av* CDO (*Av* ES-NO) has several observable *g*-values at 4.17, 4.07, 3.92, and 2.0 (*the g ~ 2 region was omitted for clarity*). All features within this spectrum can be accounted for by contributions from two spectroscopically distinct ($S = 3/2$) species (designated *1a'* and *1b'*) which differ by their rhombicity [E/D-values 0.010 (*1a'*) and 0.022 (*1b'*)]. These signals are only observed following pre-incubation with the substrate (L-Cys). Moreover, this speciation and their relative distributions are conserved across multiple enzyme preparations. Therefore, it is likely that these signals represent heterogeneous substrate binding within the active site of *Av* CDO as opposed to a contaminant within the sample. For quantitation purposes, all data was recorded below the microwave power necessary for half-saturation of the $\{FeNO\}^7$ $S = 3/2$ signal at 10 K ($P_{1/2} = 11 \pm 3$ mW).

The temperature normalized signal intensity for both *1a'* and *1b'* decreases with increasing temperature thus indicating that the $m_s = \pm 1/2$ doublet is the ground state for each species. The magnitude of the zero-field splitting parameter (*D*) was determined by plotting the EPR signal intensity for this species versus 1/T and fitting the data to a Boltzmann population distribution for a two level system. Within experimental error (0.8 cm^{-1}), both species appear to have comparable zero-field splitting ($D \sim 6.1 \pm 0.8$ cm^{-1}). As both *1a'* and *1b'* signals significantly overlap in field space the temperature dependent contributions to signal intensity for each individual species can be difficult to resolve. Therefore, additional corroboration of the zero-field splitting term was obtained by simultaneous simulation of EPR spectra collected at temperatures ranging from 4-25 K. Across this temperature range, all simulations accurately reproduce the relative intensity of *1a'* and *1b'* using this *D*-value. With the magnitude of the axial zero-field splitting validated, quantitative simulations of *1a'* and *1b'* (Figure 4.6, *dashed lines*) were calculated to determine the relative distribution of each species [40:60%], respectively. Collectively, the sum of these individual simulations account for ~80% of the total ferrous iron within the sample.

Analogous samples were prepared from cysteamine and 3-mercaptopropionate as a means to measure the substrate-specificity for this enzyme. As with L-Cys, obligate-ordered addition of the substrate-ligand was required prior to binding NO. Interestingly, samples prepared from L-Cys (1') and cysteamine (*not shown*) exhibit identical *g*-values and a similar distribution of *1a'* and *1b'* species, suggesting similar coordination heterogeneity for both ligands. However, in samples prepared using 3-mercaptopropionate (*2'*), only the single near axial S = 3/2 species is observed [E/D = 0.001] (spectroscopically equivalent to *1b'*). The reason for this deviation is not yet clear, but the simplest explanation is that L-Cys and cysteamine exhibit an equilibrium between mono- (*1a'*) and bidentate (*1b'*) substrate coordination whereas the 3-mercaptopropionate, which lacks the amine functional group, is only capable of monodentate coordination. Heterogeneous substrate-binding could also explain the relatively high K_M-value obtained for *Av* CDO in steady-state assays. Beyond its relaxed substrate specificity, the (S = 3/2) electronic structure of the *Av*-ES-NO is completely different from its mammalian analogue. In fact, the $\{FeNO\}^7$ species produced in *Av* CDO appears to more reminiscent with what have been observed in other non-heme mononuclear iron oxidase/oxygenase enzymes. The additional signal observed at g ~ 4.4 (trace *2'*) originates from trace amounts (< 10%) of substrate-bound *Av* CDO containing ferric iron in the active site. This signal and its temperature dependence are quite similar to what has been described for the mammalian enzyme(*47*). A summary of the parameters used simulate the $\{FeNO\}^7$ (S = 3/2) species produced in *Av* CDO is provided in Table 4.2. Simulation parameters for the *Mm* CDO $\{FeNO\}^7$ (S = 1/2) species is included for comparison.

It can also be demonstrated that NO-binding is reversible for *Av* ES by application of a vacuum. Samples of *Av* ES-NO were thawed anaerobically on a Schlenk line. A vacuum was applied to the aqueous sample on ice for 5 min prior exchanging the headspace with fresh argon. This process was repeated for several cycles for a total of 30 min prior to refreezing the sample and analysis by EPR. As illustrated in Figure 4.7A, within 30 minutes of repeating vacuum/argon cycling, the EPR signal intensity observed for both

1a' and *1b'* decrease by nearly 50% (*dashed line*). Within 1 hour both signals are nearly absent. Most importantly, both signals are recovered by addition of excess nitric oxide. Figure 4.7B illustrates the recovered S = 3/2 $\{FeNO\}^7$ species (*dashed line*) as compared to the original spectra prior to exposure to a vacuum (*solid line*). Interestingly, the relative distribution of *1a'* and *1b'* is slightly perturbed following re-introduction of NO [34:66%, respectably] with a greater recovery of the more rhombic specis. This may suggest a greater NO-affinity for this site. By contrast, the $\{FeNO\}^7$ (S = 1/2) species observed in samples of *Mm* CDO is completely insensitive to vacuum/argon cycling and thus NO-binding to the mammalian enzyme appears irreversible(*37*).

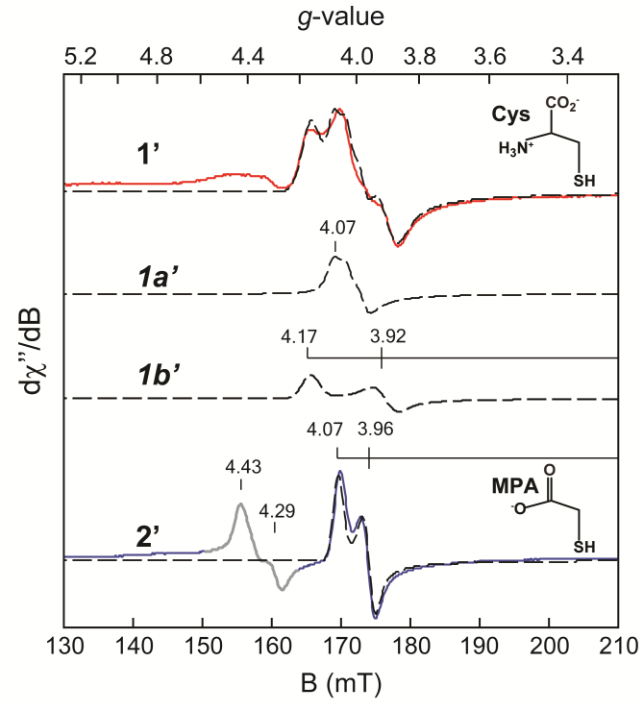

Figure 4.6 X-band EPR spectra of *Av*-ES-NO (spectrum 1', S = 3/2). Trace 1 is comprised to two (S = 3/2) species [*1a'* (40%) and *1b'* (60%)] with differing *E*/*D*-values. Trace 2' represents the signal produced when substituting 3-mercaptopropionate for Cysteine.

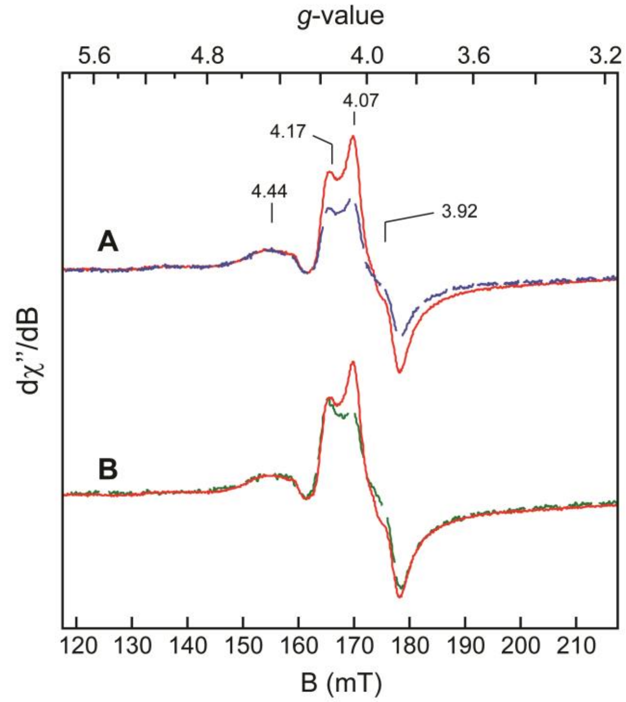

Figure 4.7 A. Reversible binding of NO to the substrate-bound *Av* CDO.

Table 4.2 EPR simulation parameters for the *Av* and *Mm* ES-NO

$\{FeNO\}^7$ Enzyme	Sim	*Spin*	*D* (cm^{-1})	*E*/*D*	g_1 (σg_1)	g_2 (σg_2)	g_3 (σg_3)	σ_B (mT)
Av CDO	L-Cys (*1a'*)	3/2	6.1 ± 0.6	0.01	2.02	2.01	1.96	0.4
	L-Cys (*1b'*)	3/2	6.0 ± 0.6	0.02	2.02	2.02	1.92	0.4
	3MPA (*2'*)	3/2	5.0 ± 0.6	0.01	2.01	2.01	2.00	0.6
Mm CDO	L-Cys	1/2	-	-	2.07 (0.006)	2.02 (0.009)	1.98 (>0.001)	

Discussion

Among the Arg- and Gln-type CDO enzymes the overall 3-His first coordination sphere appears to be largely conserved. However, the absence of the C93-Y157 pair and equivalent R60 residue in bacterial Gln-type CDO enzymes imply that there may be significant differences in both substrate-coordination and stabilizing outer-sphere interactions among these enzyme types. Catalytically, only modest differences are observed in the optimal k_{cat} (v_0/[E]) obtained for CDO isolated from *Mus musculus* (k_{cat} = 0.6 ± 0.1) and *Azotobacter vinelandii* (1.0 ± 0.1) under comparable assay conditions. On notable difference is the significantly higher Michaelis-Menten composite constant obtained for *Av* CDO (K_M = 11.4 ± 0.9 mM) as compared to *Mm* CDO (K_M = 2.3 ± 0.3 mM). As a result, the specificity of the mammalian enzyme (k_{cat}/K_M = 260 ± 30 $M^{-1}s^{-1}$) is higher than observed for the bacterial CDO (k_{cat}/K_M = 120 ± 20 $M^{-1}s^{-1}$).

Notably, the k_{cat}- and k_{cat}/K_M pH-profile obtained for *Av* CDO exhibits markedly different behavior as compared to *Mm* CDO. First, the pH-profile for both steady state kinetic parameters (k_{cat} and k_{cat}/K_M) are '*bell shaped*' in that they decreases at both low and high pH values. Within the accessible pH range of *Av* CDO (5.5 < pH < 10), two pKa-values can be obtained by fitting the k_{cat}-pH data to equation 1 [pKa_1 = 5.64 ± 0.06 and pKa_2 = 9.86 ± 0.06]. Thus, the 'Gln-type' bacterial CDO appears to have a much broader optimal pH range as compared to the mammalian enzyme. The basic pKa-value (pKa_2) is quite similar to what is observed for the *Mm* CDO [9.9 versus 10.3; ΔpKa = 0.4). This suggests that the basic ionizable group may be conserved between the two enzymes. This, and the fact that that pKa_2 is quite similar to what is typically observed for a tyrosine residue (pKa ~ 10) suggest that this ionizable group may be attributed to the conserved tyrosine residue Y159 in *Av* CDO. By contrast, the lower pKa-value is significantly more acidic in *Av* CDO as compared to *Mm* CDO [pKa_1 = 5.6 versus 7.4; ΔpKa = 1.8]. The shift in the acidic pKa_1 is much more pronounced in the k_{cat}/K_M-pH profile [pKa_2 of 5.11 ± 0.07 versus 7.9 ± 0.2; $\Delta pka_1 = 2.8$]. This suggests a significant change in the nature or identity of the acidic groups utilized in Arg- and Gln-type CDO enzymes. The identity of this ionizable group is not yet known but its pKa-value (5.1-5.6) is consistent values reported for catalytically essential His residues. As H157 is universally conserved among bacterial CDO enzymes (both Arg- and Gln-types), this residue is a strong candidate for further evaluation.

Another striking difference is that the (CSA/O_2)-coupling efficiency is significantly greater for *Av* CDO (90 ± 6 %) by comparison to the mammalian enzyme (76 ± 7%)(*201, 206*). Moreover, unlike *Mm* CDO(*40*), the bacterial enzyme appears to be nearly fully coupled across the entire accessible pH range of the enzyme. It has been demonstrated that formation of the C93-Y157 pair increases enzymatic specific activity and efficiency (*36, 39, 40*). Paradoxically, formation of the C93-Y157 cross-link also appears to be initiated by promiscuous (*uncoupled*) side reactions within the *Mm* CDO active site during turnover with cysteine(*201, 206*). It is therefore tempting to speculate that the decreased coupling efficiency observed in the mammalian CDO may provide a cysteine-dependent mechanism to increase enzymatic activity under physiologic conditions of excess turnover.

Beyond the differences noted in steady-state pH-profile of *Av* CDO, EPR spectroscopic characterization of the substrate-bound enzyme (ES) treated with nitric oxide (NO) reveal stark differences in the ground state electronic structure of the iron-nitrosyl complex produced in each enzyme. Typically, addition of nitric oxide (NO) to a substrate-bound mononuclear non-heme iron center typically results in the formation of a $\{FeNO\}^7$ ($S = 3/2$) species characterized by an axial EPR spectrum ($g_{x,y,z} \sim 4, 4, 2$). Interestingly, samples prepared from L-Cys (1’) and cysteamine (*not shown*) exhibit identical *g*-values and a similar distribution of mixed species, suggesting similar coordination heterogeneity for both ligands. However, in samples prepared using 3-mercaptopropionate, only the single near axial S = 3/2 species is observed [E/D = 0.001] sugesting that L-Cys and cysteamine exhibit an equilibrium between mono- and bidentate substrate coordination whereas the 3-mercaptopropionate, which lacks the amine functional group, is only capable of monodentate coordination. This heterogeneous substrate-binding could also explain the relatively high K_M-value obtained for L-Cys and Cysteamine substrates in steady-state assays.

Contrary to this, we have previously demonstrated that addition of NO to the *Mm* ES complex produces an anisotropic S = 1/2 EPR signal with observed g-values of 2.07, 2.03, and 1.96(*37*). Spin quantitation of this signal accounts for 70-85% of the total ferrous iron present in *Mm* CDO samples. Therefore, this species cannot be attributed to promiscuous reactions with NO or trace impurities. Furthermore, the *Mm*-ES-NO signal is only produced with the native L-Cys substrate and to a lesser extent with D-Cys;(*37*) although a recent report indicates that a similar signal can also be produced by addition of NO to enzyme pre-complexed with L-selenocysteine (L-Sec)(*212*). Unlike typical Fe-bound nitrosyl species, NO-binding to *Mm* ES is non-reversible; neither application of a vacuum for 1 hour or intense light had any impact on the *Mm*-ES-NO signal(*209, 210, 213*). Collectively, all our spectroscopic and computational modeling is consistent with the assignment of a low-spin iron(II) site coordinated to a ligand centered radical.

While unusual among non-heme iron enzymes, synthetic $\{FeNO\}^7$ (S = 1/2) complexes have been reported in the literature. For example, Wieghardt and coworkers have characterized several $\{FeNO\}^7$ (S = 1/2) model complexes with amine and thiolate coordination(*210, 214*). Indeed, these complexes were a useful point of comparison in our original assignments. In these studies, EPR and Mössbauer characterization of model complexes was used to validate DFT computational models, all of which were used to conclude that the ground state of these complexes can be described as a ligand-centered NO• radical (S = 1/2) coordinated to a low spin (S = 0) ferrous iron(*210, 211*). More recently, Goldberg *et al.* reported a pair of synthetic complexes specifically designed to model the substrate-bound active site of CDO. The NO-bound complexes also exhibit a similar $\{FeNO\}^7$ (S = 1/2) electronic configuration. Moreover, detailed spectroscopic (EPR, Mössbauer, and S-atom K-edge XAS) and computational DFT-modeling of these complexes agree with the assignment of this species as a low-spin Fe^{II} with a ligand centered radical(*215*).

As with the mammalian enzyme, it was observed that *Av* CDO also exhibits an obligate-ordered addition of L-Cys prior to NO consistent with the obligate ordered addition commonly observed among this enzyme class. However, in stark contrast to what is observed for *Mm* CDO, anaerobic addition of NO the substrate-bound *Av* CDO produces a $\{FeNO\}^7$ (S = 3/2) ground state electronic configuration.

From the experiments utilizing substrate-analogues cysteamine and 3-mercaptopropionate, it was concluded that the observed speciation of iron-nitrosyl sites produced in *Av* CDO (*1a'* and *1b'*) is likely due to an equilibrium between two substrate-bound structural configurations; potentially mono- versus bidentate coordination of the Cys-substrate. The fact that all ligands (L-cysteine, cysteamine, and 3-mercaptopropionate) are capable of gating the binding of NO to the Fe-site suggests that the substrate-specificity of *Av* CDO is more relaxed as compared to the mammalian enzyme. This suggests that the Gln-type CDO enzymes also utilize three simultaneous points of interaction between the substrate-and enzyme to gate reactivity with molecular oxygen(*38, 201*). Presumably, two points of simultaneous interaction are provided by the bidentate substrate coordination to the *Av* CDO Fe-site. A third point of interaction is likely produced by hydrogen bonding between the Cys-carboxylate group and the conserved tyrosine Y159 of *Av* CDO.

The quartet spin-state (S = 3/2) is commonly observed among non-heme iron iron-nitrosyl model complexes and enzymes; however, this result is surprising given that sequence homology suggests that the first-coordination sphere of both enzymes is likely conserved. While the crystal structure for the substrate-bound *Av* CDO has not been solved, structural comparisons can be inferred from the *Bacillus subtilis* CDO crystal structure (*Bs* CDO; pdb code 4QM8)(*202*). As illustrated in Figure 4.1, the most obvious difference between the *Bs* CDO and *Mm* CDO structure is the presence of the C93-Y157 pair., thus an important point of investigation is whether the cross-link alters the coordination geometry of the Fe-bound NO ligand. Potentially, this could alter the $\{FeNO\}^7$ ES-NO electronic structure and NO/thiolate reactivity among CDO enzymes.

In support of this hypothesis, one interesting conclusion from our previous spectroscopically trained computational studies of cyanide binding to Fe^{III}-CDO was that the S-atom of the C93-Y157 pair sterically impinges on the Fe^{III}-bound cyanide anion(*40*). It was determined that in the absence of the C93-Y157 pair, the Fe-C-N bond angle is nearly linear (176.3°). Alternatively, in the presence of the cross-link this angle is significantly decreases by 7.1° (169.2°). Moreover, the distal O-atom of NO is bent toward the Cys-substrate S-atom. While the perturbation to the Fe-C-N bond angle is relatively minor, it should be noted that cyano ligands exhibit a strong preference for linear coordination. It is reasonable that this effect may be more pronounced with a π-donating ligand like nitric oxide, which favors a bent coordination geometry. Clearly, additional work is necessary to explore the role of the C93-Y157 pair on the coordination geometry of Fe-bound ligands within mammalian cysteine dioxygenase enzymes.

Given that the most obvious difference between *Av* CDO and *Mm* CDO is the presence of the C93-Y157 pair, an obvious point of further investigation is whether the cross-link directly influences the coordination geometry of the Fe-bound NO ligand. Potentially, this could alter the {FeNO}^{7} ES-NO electronic structure and NO/thiolate reactivity among CDO enzymes.

Appendix A

Characterization of Heme enzyme (crocodile hemoglobin)

UV-Visible spectroscopic properties of crocodile α-globin chains

UV-Visible spectroscopy was utilized to interrogate the heme occupancy within CroHb α-globin. As expected for typical hematoporphyrin proteins, the purified α-globin chain exhibited an intense Soret absorption band at 415 nm and two weak bands (termed Q-bands) at 541 and 575 nm. The absorption maximum of the Soret band is consistent with 6-coordinate Hb in the α-peptide. The two smaller absorption peaks at 541 nm and 575 nm (designated β- and α-bands, respectively) are diagnostic of the oxidized resting Hb oxidation state (Figure 1, inset). Several attempts made to remove oxygen from samples of purified CroHb were made by repeated vacuum/Ar-purging on the Schlenk line. However, in these experiments, the spectroscopic features typically associated with deoxygenated Hb (deoxyHb) could not be obtained. Only by addition of sodium dithionite, the typical spectrum for deoxyHb obtained.

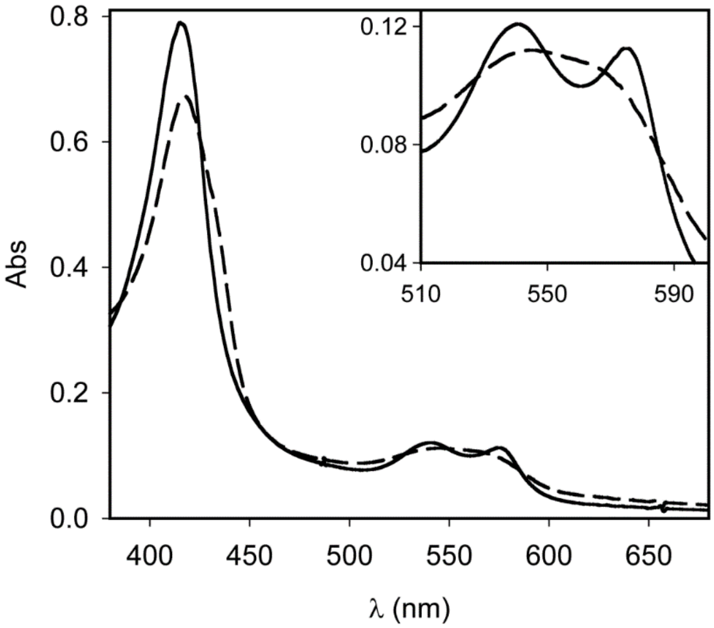

Figure 1. UV-Visible spectra of purified recombinant *C. siamensis* α-globins

By comparison to oxyHb, the Soret band for deoxyHb is slightly red-shifted (λ = 420 nm) and the Q-band splitting is lost. Instead a broad feature is observed in this region at ~550 nm which is characteristic of 5-coordinate Hb.Binding of potassium cyanide to the reduced CroHb α-globin was performed to demonstrate accessibility of the reduced heme active site to exogeneous ligands. In these experiments, UV-visible spectroscopy was used to monitor the change within the β- and α-absorption (Q-bands) upon treatment with the potent inhibitor, potassium cyanide. As indicated by Figure 2, the purified (oxy) CroHb exhibited the clearly distinct α- and β-bands consistent with the 6-coordinate heme center (solid line). However, as described above, reduction of CroHb results in the loss of the resolved Q-band α/β-peaks and replacement with a single broad absorption at ~ 550 nm. The loss of Q-band splitting is diagnostic of the decreased coordination number (5-coordinate) of the heme site upon reduction. However, upon addition of a slight molar excess of potassium cyanide (1.5 equivalents), the Q-band splitting is recovered indicating tight binding of cyanide and recovery of the 6-coordinate heme center

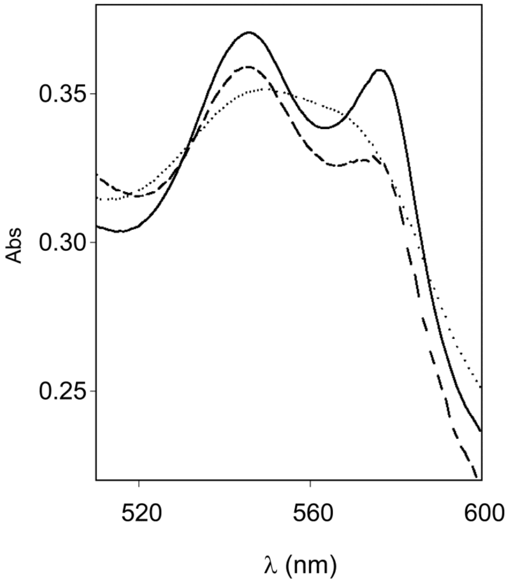

Figure 2. The UV-Visible spectra of cyanide binding; CN^- in reduced Hb (dash).

Electron paramagnetic resonance (EPR) spectroscopy

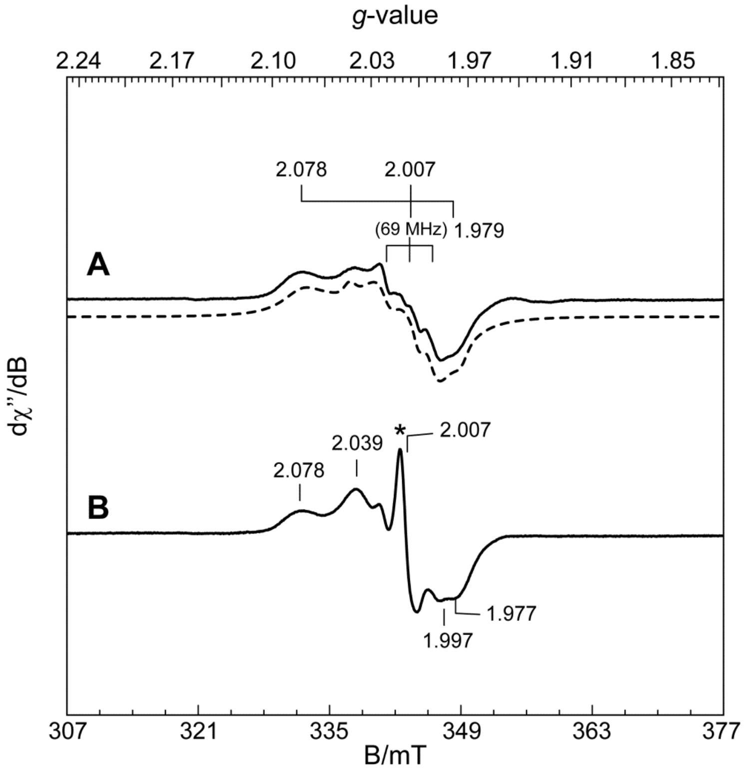

Figure 3. The EPR spectra of the reduced CroHb α-globin upon addition of substoichiometric (A) and excess NO (B). EPR simulation of the *S* = 1/2 signal dashed line is overlaid on the spectra for comparisons.

EPR spectroscopy was used to study the binding of nitric oxide to crocodile α-globin. In these experiments (Figure 3), NO was added to reduced CroHb α-globin substoichiometrically (spectra A) under strict anaerobic conditions. For comparison, spectrum B was collected following addition of excess NO relative to α-globin. The sharp isotropic *g* ~ 2.0 signal designated (*) is due to residual methyl viologen and dithionite. The resulting *S* = 1/2 signal from NO-bound crocodile α-globins exhibits *g*-values [2.08, 2.01, and 1.98] very similar to those observed for NO-bound hemoglobin. The clear triplet feature split by 1.7 mT (*A* ~ 69 MHz) observed within the g ~ 2 region (spectra A) originates from

NO-binding to the 5-coordinate heme (^{14}N, $I = 1$). Historically, this triplet feature has been exclusively associated with NO-binding within the α-globin of Hb under conditions of substoichiometric NO addition. The additional shoulder features observed at $g \sim 2.04$ (spectra B) are observed under conditions of excess NO. As described elsewhere, these additional features and apparent loss of the clear triplet feature is consistent with additional conformational speciation within the NO-bound active site.

Circular dichroism (CD)

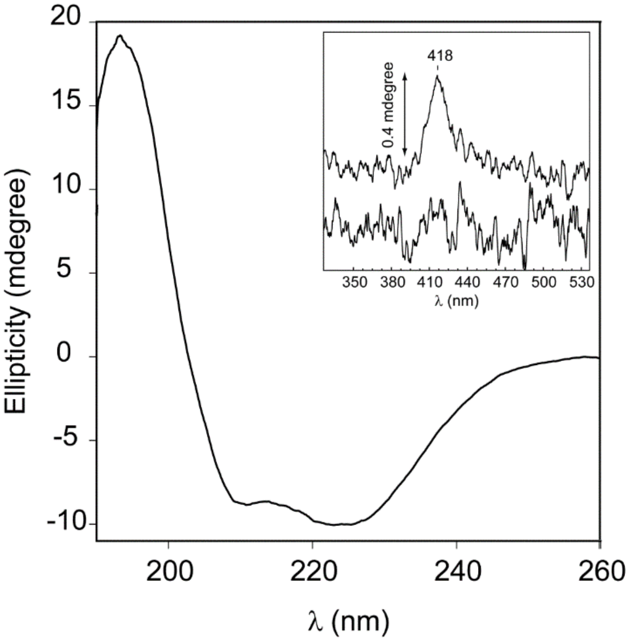

Figure 4. Circular Dichroism (CD) spectra for the purified CroHb α-globins. The inset shows the CD spectra of Soret band in oxidized state (upper) and reduced state (lower).

Appendix B

Characterization of Manganese-oxo complexes

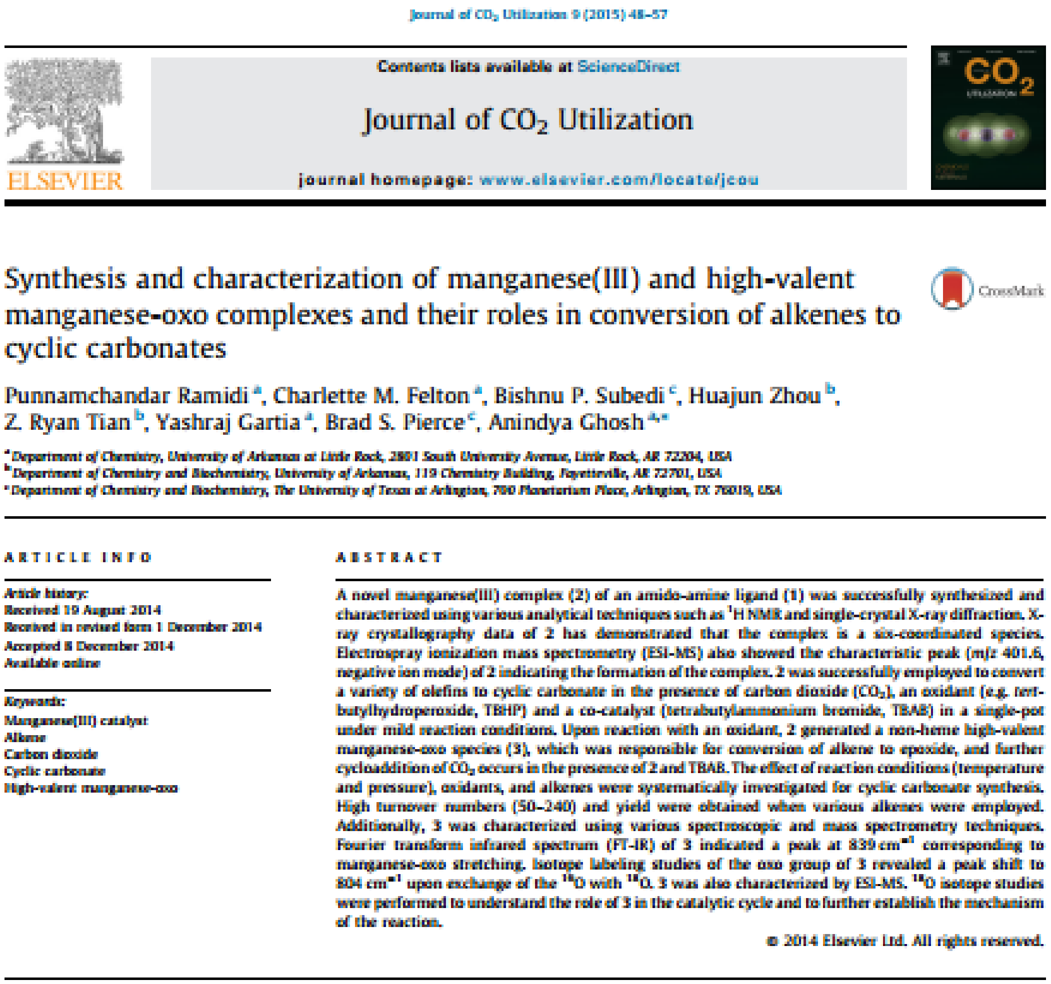

Journal of CO_2 Utilization 9 (2015) 48–57

Contents lists available at ScienceDirect

Journal of CO_2 Utilization

journal homepage: www.elsevier.com/locate/jcou

Synthesis and characterization of manganese(III) and high-valent manganese-oxo complexes and their roles in conversion of alkenes to cyclic carbonates

Punnamchandar Ramidi [a], Charlette M. Felton [a], Bishnu P. Subedi [c], Huajun Zhou [b], Z. Ryan Tian [b], Yashraj Gartia [a], Brad S. Pierce [c], Anindya Ghosh [a,*]

[a] *Department of Chemistry, University of Arkansas at Little Rock, 2801 South University Avenue, Little Rock, AR 72204, USA*
[b] *Department of Chemistry and Biochemistry, University of Arkansas, 119 Chemistry Building, Fayetteville, AR 72701, USA*
[c] *Department of Chemistry and Biochemistry, The University of Texas at Arlington, 700 Planetarium Place, Arlington, TX 76019, USA*

ARTICLE INFO

Article history:
Received 19 August 2014
Received in revised form 1 December 2014
Accepted 8 December 2014
Available online

Keywords:
Manganese(III) catalyst
Alkene
Carbon dioxide
Cyclic carbonate
High-valent manganese-oxo

ABSTRACT

A novel manganese(III) complex (2) of an amido-amine ligand (1) was successfully synthesized and characterized using various analytical techniques such as ^1H NMR and single-crystal X-ray diffraction. X-ray crystallography data of 2 has demonstrated that the complex is a six-coordinated species. Electrospray ionization mass spectrometry (ESI-MS) also showed the characteristic peak (*m*/*z* 401.6, negative ion mode) of 2 indicating the formation of the complex. 2 was successfully employed to convert a variety of olefins to cyclic carbonate in the presence of carbon dioxide (CO_2), an oxidant (e.g. *tert*-butylhydroperoxide, TBHP) and a co-catalyst (tetrabutylammonium bromide, TBAB) in a single-pot under mild reaction conditions. Upon reaction with an oxidant, 2 generated a non-heme high-valent manganese-oxo species (3), which was responsible for conversion of alkene to epoxide, and further cycloaddition of CO_2 occurs in the presence of 2 and TBAB. The effect of reaction conditions (temperature and pressure), oxidants, and alkenes were systematically investigated for cyclic carbonate synthesis. High turnover numbers (50–240) and yield were obtained when various alkenes were employed. Additionally, 3 was characterized using various spectroscopic and mass spectrometry techniques. Fourier transform infrared spectrum (FT-IR) of 3 indicated a peak at 839 cm^{-1} corresponding to manganese-oxo stretching. Isotope labeling studies of the oxo group of 3 revealed a peak shift to 804 cm^{-1} upon exchange of the ^{16}O with ^{18}O. 3 was also characterized by ESI-MS. ^{18}O isotope studies were performed to understand the role of 3 in the catalytic cycle and to further establish the mechanism of the reaction.

Appendix C

Supplementary Figures (Chapter 2)

Qualitative substrate screening was performed by thin layer chromatography (TLC) to analyze product formation (Figure S1).

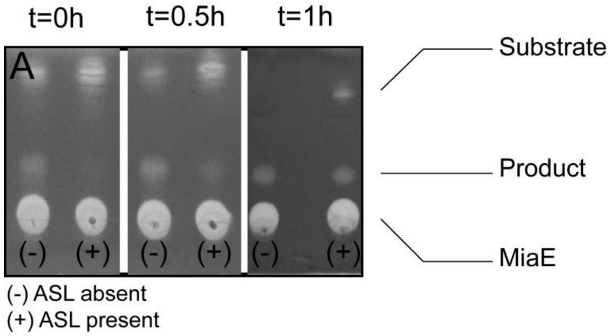

Figure S1. TLC indicates loss of substrate 5c and appearance of MiaE hydroxylated product with time. TLC stained in $KMnO_4$ to aid in qualitative analysis.

HILIC chromatogram of *E/Z* product standards

Diastereomeric mixtures of both *E*-8c and *Z*-8'c standards were analyzed by HILIC chromatography alongside enzymatic assay of 5c in order to evaluate stereoselectivity. Top line represents *Z*-8'c, middle line represents *E*-8c, and bottom chromatograph represents the enzymatic assay quenched at 10 min.

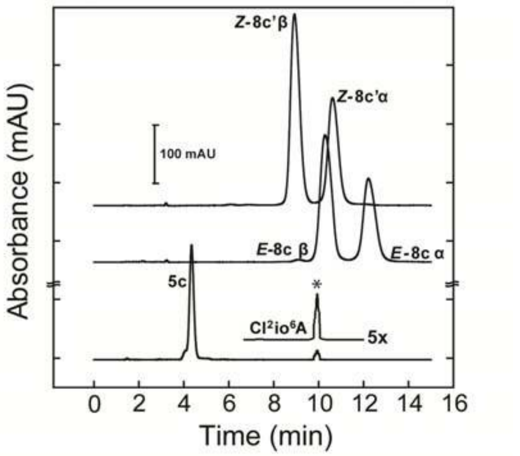

Figure S2. Chromatogram indicates similar retention times of enzymatic product and the *E*-8c synthetic standard.

Calibration of sodium dithionite solutions used in reductive titrations: Stock solutions of sodium dithionite were prepared by weighing dry $Na_2S_2O_4$ (Sigma Aldrich) into anaerobic buffer (20 mM HEPES, 40 mM NaCl, pH 8.0) within in a Coy anaerobic glove box (Coy Laboratory Products Inc., Grass City, MI).

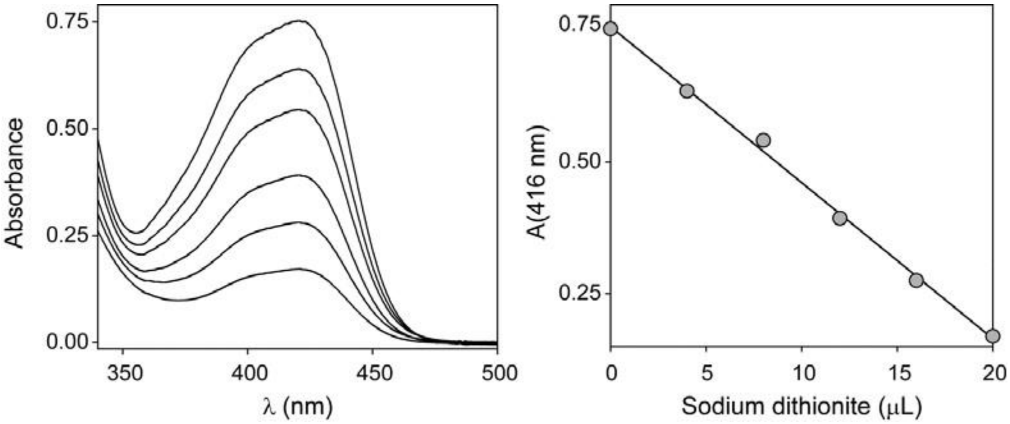

Figures S3. Stacked UV visible spectra of $K_3[Fe(CN)_6]$ showing the decrease in absorbance at 420 nm with addition of sodium dithionite solution (*left*). Representative sodium dithionite solution calibration curve (*right*); slope of best fit line, m = -0.0296 $AU \cdot \mu L^{-1}$ (50.7 $nmol \cdot \mu L^{-1}$)

For each reductive titration, a fresh stock dithionite solution was prepared and calibrated by titrating with 1.8 mL ~ 0.7 mM $K_3[Fe(CN)_6]$ solution prior to use. Figure S3 shows representative stacked UV-visible spectra (*left*) illustrating the decrease in absorbance of a potassium ferricyanide solution at 420 nm upon titration with freshly prepared sodium dithionite solution. From the volume of $K_3[Fe(CN)_6]$ solution (1.8 mL), the extinction coefficient of $K_3[Fe(CN)_6]$ (ε_{420} = 1,050 $M^{-1}cm^{-1}$) and the slope of the calibration curve (m = -0.0296 $AU \cdot \mu L^{-1}$) shown in Figure S3 (*right*) the concentration of total 'reducing equivalents' within the dithionite solution was determined; in this instance, 51 mM reducing equivalents. Prior to use in reductive titrations, the calibrated dithionite solution was diluted

8.6-fold with anaerobic buffer (20 mM HEPES, 40mM NaCl, pH 8.0) containing catalytic methyl viologen (~ 0.4 μM).

Reductive titration of resting MiaE:

Figure S4 shows representative UV-visible spectra of MiaE during reductive titration. Aliquots (~4 μL) of standardized sodium dithionite solution (5.9 mM reducing equivalents) were added under constant mixing to 1.4 mL of anaerobic MiaE using a 10 μL Hamilton gas-tight syringe. Following each addition of dithionite solution, the UVvisible spectrum was monitored for ~5 min to ensure that reduction had gone to completion prior to adding more dithionite solution.

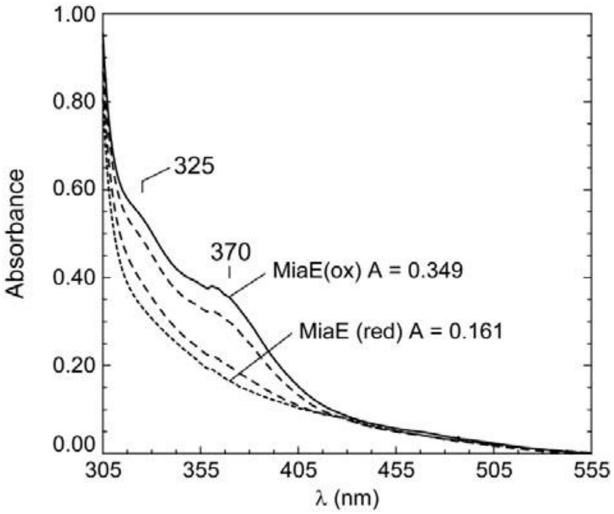

Figure S4. Selected UV-visible spectra of MiaE during reductive titration with calibrated sodium dithionite solution. The fully oxidized spectra and fully reduced spectra are indicated by the solid and dotted lines, respectively. Partially reduced MiaE spectra (dashed lines) following addition of 6 and 14 μL sodium dithionite solution.

pH dependence of the Fe-associated bands:

As stated in *Materials and Methods*, typically purified MiaE fractions are selected on the basis of the ratio of UV-visible absorbance at 280nm over 370 nm. At pH 8.0, resting MiaE typically exhibits a A_{280}/A_{370} ratio of ~7.8 ± 0.3. However, as illustrated in Figure S5, this ratio is decreases with increasing pH. While the absorbance at 280 nm appears to be relatively unaffected within the pH range (±7%), the intensity of the absorbance at 370 nm shows a clear pH dependence. Maximum intensity at 370 nm is observed at pH 8.4 with an apparent midpoint pH ~ 8.1.

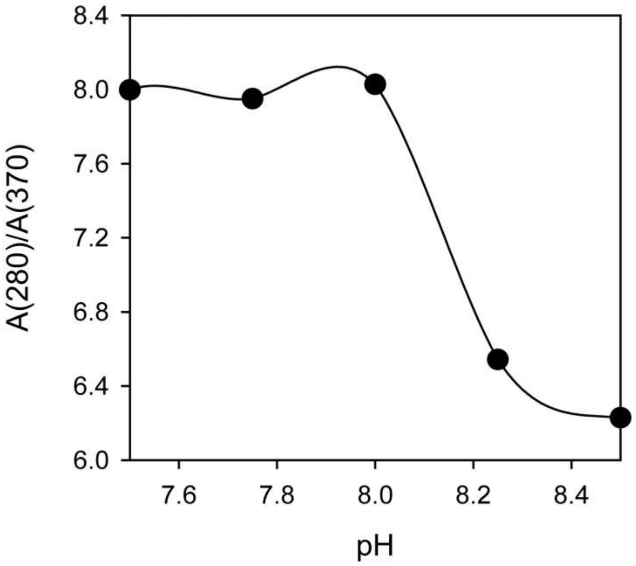

Figure S5. Observed change in the A280/A370 observed by UV-visible spectroscopy as a function of pH.

For all pH measurements, an initial sample of purified MiaE (200 μM) was diluted 50fold into an appropriate Good's buffer [HEPES, pKa 7.55; MES, pKa 6.15; CHES; pKa 9.55] (200 mM) previously titrated to the desired pH. Following dilution, the final MiaE concentration of UV-visible samples was 4 μM. The protein was allowed to equilibrate at the new pH for 60-minutes on ice prior to measuring the UV-visible spectra. MiaE showed significant precipitation below pH 7.0 and above 8.5 and thus these results were omitted. Since maximum stability was observed at pH 8.0, this pH was selected for subsequent experiments.

Catalase activity of MiaE: In these experiments, a standard Clarke-type oxygen electrode was used to monitor the amount and initial rate (v_0) of O_2-evolved upon addition of as-isolated MiaE to 20 mM HEPES, 100 mM NaCl, and pH 8 at H_2O_2 concentrations ranging between 15 and 80 μM at 25 °C. The volume of each reaction was fixed at 1.5 mL with a final MiaE Fe_2-site concentration of 5 μM.

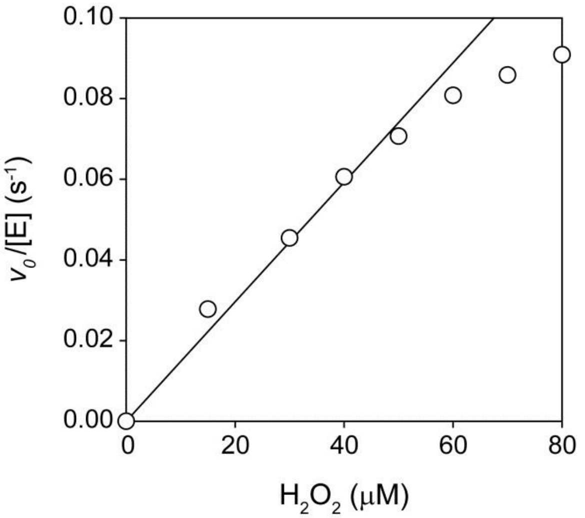

Figure S6. Kinetics of MiaE catalase activity as measured by O2-selective Clarke electrode. The pseudo-second order rate constant was determined by linear regression.

Appendix D

Supplementary Figures (Chapter 3)

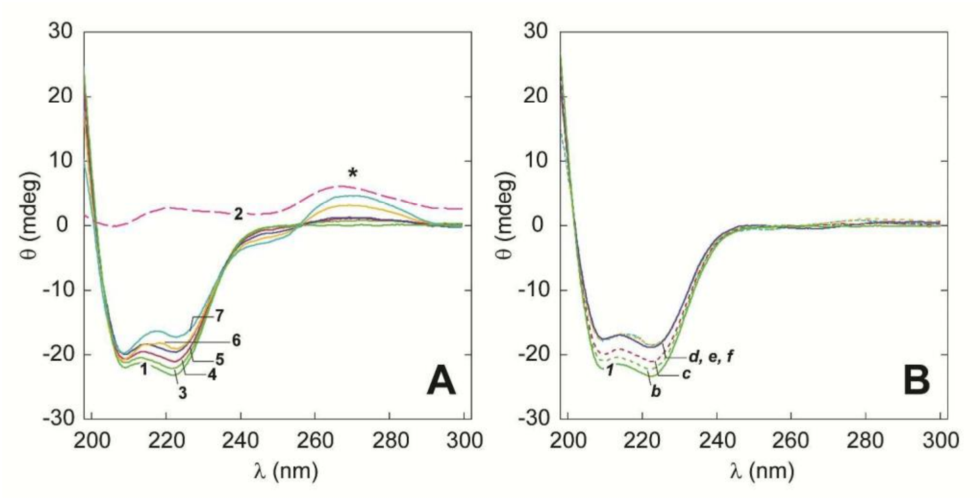

Figure S1. CD titration of oxidized MiaE with ACSL^{Trp}. A. Stacked CD spectra of resting MiaE (5 μM) with increasing concentration of ACSL^{Trp} RNA oligomer. Difference spectra b-f (panel B) are produced by subtracting the ACSL^{Trp} CD spectrum (*scaled for concentration*) from observed spectra 3-7.

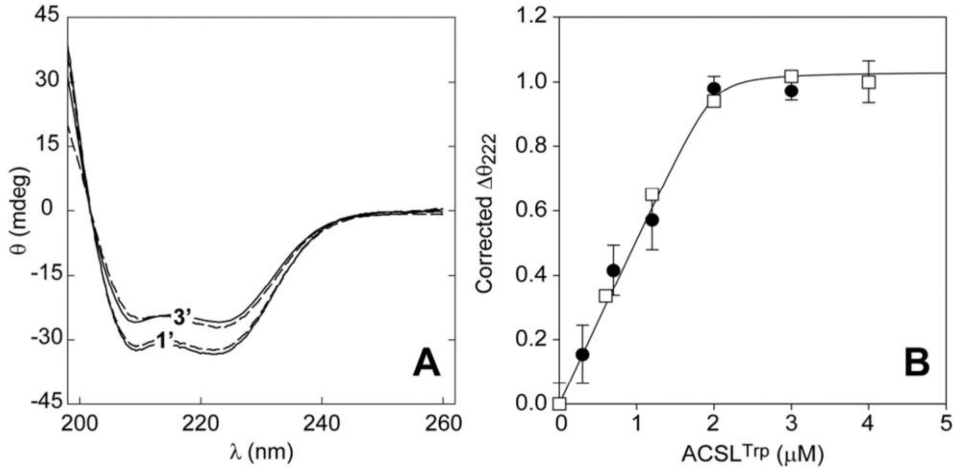

Figure S2. Comparison of oxidized and reduced MiaE CD spectra with and without stoichiometric ASCL^{Trp}. A. CD spectra of oxidized (*solid line*) and reduced (*dashed line*) MiaE in the presence and absence of ACSL^{Trp}. Sample conditions: 5 μM MiaE with 0 molar equivalents (1') ACSL^{Trp}, 1.5 equivalent ACSL^{Trp} (3'). B. Titration of 2 μM oxidized (●) and reduced MiaE (□) with ACSL^{Trp}. Given the limited data collected and instrumental sensitivity, it is not possible to resolve any difference between the RNA-binding affinity of oxidized and reduced enzyme using CD spectroscopy.

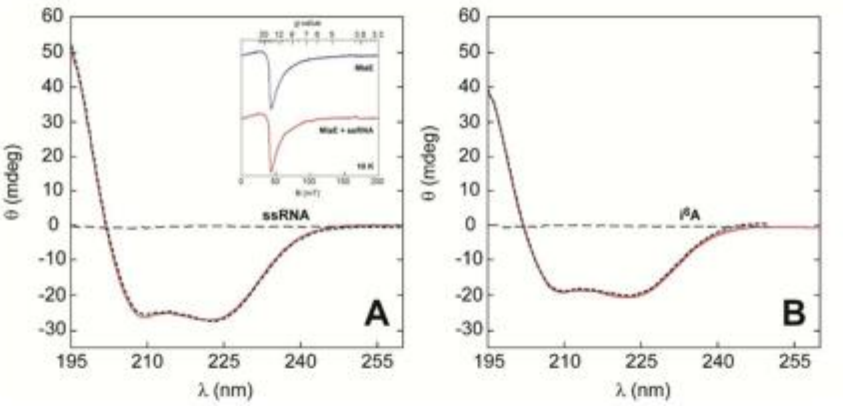

Figure S3. A. CD spectra of resting MiaE (*solid line*) and with addition of 1.5 mol equivalents ssRNA (*dashed line*). The inset of panel A demonstrates the equivalence of the parallel mode *g* ~ 16 EPR signal observed for reduced MiaE in the presence and absence of ssRNA. B. Influence of i^6A-nucleoside (*3-fold molar excess*) addition on the resting MiaE CD spectra (4 µM). Dashed line represents the CD spectra for (12 µM) i^6A nucleoside (*ms^2i^6A and Cl^2i^6A not shown*). EPR results not collected due to the low solubility of the i^6A free nucleoside.

The above CD experiments demonstrate that the RNA hairpin loop is required to produce the observed conformational change within the protein-RNA complex. An obvious follow up question is whether or not this interaction is specific to RNA sequences that MiaE recognizes as a substrate. Therefore, similar CD titration experiments as described for $ACSL^{Trp}$ were performed for $ACSL^{Leu}$ and $ACSL^{Met}$ RNA oligomers (*Supporting Information*, Table S2). Only $tRNA^{Trp}$ and $tRNA^{Leu}$ (*complementary to codons starting with U*) represent physiological substrates for the MiaA/B/E hypermodification pathway. $ACSL^{Met}$ was included to evaluate the specificity of MiaE for tRNA-interactions. In these experiments no significant difference could be observed in the binding affinity for each oligomers. This suggests that binding of MiaE to any a hairpin loop elicits the observed conformational change regardless of RNA sequence.

Normalized change in the *g* ~ 16 parallel mode EPR signal with added ASCL^{Trp}.

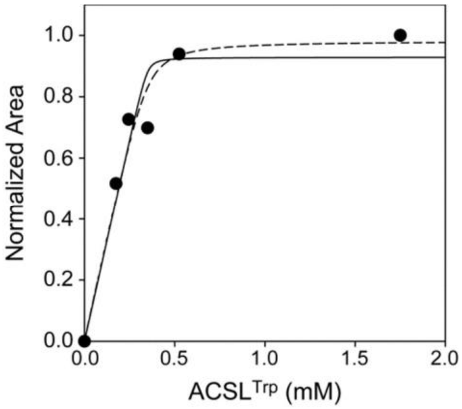

Figure S4. Relative change in the X-band parallel mode (∥) EPR spectra of reduced MiaE upon addition of ACSL^{Trp}

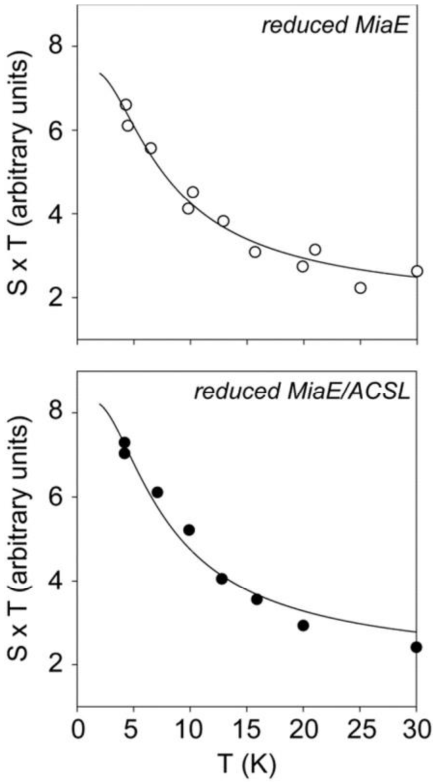

Figure S5. Temperature normalized signal intensity of *g* ~ 16 parallel mode EPR signal.

Table S1. Spectroscopic parameters

		UV-Vis		Mössbauer parameters	
				FeIII-FeIII	FeII-FeII
Enzyme	Class	λ_{max}	ε(M-1cm-1)	$\delta/\Delta E_Q$	$\delta/\Delta E_Q$
MiaE	Monooxygenase	320 370	5800	[1] 0.50/0.65 [2] 0.53/1.57 [3] 0.49/2.20	[1] 1.19/2.86 [2] 1.32/3.12
MMOH	Monooxygenase			0.50/0.87 0.51/1.16	1.3 /3.14 1.3/ 2.5
T4MOH	Monooxygenase			0.51/0.93 0.56/1.55	1.31/ 2.68 1.31/ 3.21
Hemerythrin	O_2-transport			[1] 0.50/1.40 [2] 0.50/1.96	
RNR-R2	Ribonucleotide modification	325 370	9400 7200	0.53/1.66 0.44/ 2.45	1.26/3.13 1.19/2.91
Δ9D	Desaturase	340	8000	0.50/ 0.74 0.53/1.54 0.50/2.2	1.30/3.04 1.30/3.36

Table S2. Selected hairpin sequences for tRNA anticodon stem loop (ACSL) regions for *Salmonella Typhimurium LT2.*

	Name	Anticodon	Codon	ACSL 5’-Sequence-3’	MWT (Da)	T_m (°C)*
	(ACSL)$_1^{\text{Leu}}$	CAA	UUG	^{28}GUU**G**AU**UCAA**AAUCAA^{44}C	5,600.3	44 $^{[47.3,\ 50.3]}$
	(ACSL)$_2^{\text{Leu}}$	UAA	UUA	^{28}AGG**G**AU**UUAA**AAUCCC^{44}U	5,616.3	46
●	(ACSL)$^{\text{Met}}$	CAU	AUG	^{28}CAUCACU**CAU**AAUGAU^{44}G	5,576.2	46 $^{[37.1]}$
	(ACSL)$^{\text{Tyr}}$	GUA	UAU/UAC	^{28}GCA**G**AC**UGUA**AAUCUG^{44}C	5,631.3	50
	(ACSL)$^{\text{Phe}}$	GAA	UUU/UUC	^{27}GGG**G**AU**UGAA**AAUCCC^{43}C	5,670.3	52
	(ACSL)$^{\text{Cys}}$	GCA	UGC	^{26}GCG**G**AU**UGCA**AAUCCG^{42}U	5,647.3	52
●	(ACSL)$_{\text{I.V}}^{\text{Ser}}$	GGA	UCC	^{28}CAC**G**CC**UGGA**AAGUGU^{44}G	5,686.3	54
	(ACSL)$_2^{\text{Ser}}$	CGA	UCG	^{28}CCG**G**UC**UCGA**AAACCG^{44}G	5,645.3	56
	(ACSL)$^{\text{Trp}}$	CCA	UGG	^{27}CCG**G**UC**UCCA**AAACCG^{43}G	5,605.3	56 $^{[55.6]}$

Predicted Wallace melting temperature designated by (*), IDT DNA technologies predicted temperature indicated in superscripted square brackets [ ]. With the exception of tRNA$_{\text{I.V}}^{\text{Ser}}$, tRNAs complementary to codons staring with U are viable substrates for MiaE. Non-MiaE substrate ACSL sequences are designated by (●).

Sequence comparison between ACSL regions (Leu$_1$, Met, and Trp)-tRNA, position 37 indicated by white lettering.

(ACSL)$_1^{\text{Leu}}$ ^{28}GUUGAUUCAAAAUCAA^{44}C

(ACSL)$^{\text{Trp}}$ ^{27}CCGGUCUCCAAAACCG^{43}G

(ACSL)$^{\text{Met}}$ ^{28}CAUCACUCAUAAUGAU^{44}G

References

1. Bertini, I. (2007) *Biological Inorganic Chemistry: Structure and Reactivity*, University Science Books.
2. Solomon, E. I., Decker, A., and Lehnert, N. (2003) Non-heme iron enzymes: contrasts to heme catalysis, *Proc Natl Acad Sci U S A 100*, 3589-3594.
3. Pierce, B. S., Elgren, T. E., and Hendrich, M. P. (2003) Mechanistic implications for the formation of the diiron cluster in ribonucleotide reductase provided by quantitative EPR spectroscopy, *J Am Chem Soc 125*, 8748-8759.
4. Fox, B. G., Lyle, K. S., and Rogge, C. E. (2004) Reactions of the diiron enzyme stearoyl-acyl carrier protein desaturase, *Acc Chem Res 37*, 421-429.
5. Abu-Omar, M. M., Loaiza, A., and Hontzeas, N. (2005) Reaction mechanisms of mononuclear non-heme iron oxygenases, *Chem Rev 105*, 2227-2252.
6. Neidig, M. L., and Solomon, E. I. (2005) Structure-function correlations in oxygen activating non-heme iron enzymes, *Chem Commun (Camb)*, 5843-5863.
7. Rybak-Akimova, E. V. (2010) Mechanisms of Oxygen Binding and Activation at Transition Metal Centers, *John Wiley & Sons, Inc*.
8. Feig, A. L., and Lippard, S. (1993) Relations of non-heme iron(II) centers with dioxygen in biology and chemistry, *Chem. Rev. 94*, 759-805.
9. Costas, M., Mehn, M. P., Jensen, M. P., and Que, L. (2004) Dioxygen Activation at Mononuclear Nonheme Iron Active Sites: Enzymes, Models, and Intermediates, *Chem. Rev. 104*, 939-986.
10. Que, L., Jr., and Ho, R. Y. (1996) Dioxygen Activation by Enzymes with Mononuclear Non-Heme Iron Active Sites, *Chem Rev 96*, 2607-2624.
11. Stipanuk, M. H. (2004) Sulfur Amino Acid Metabolism: Pathways for Production and Removal of Homocysteine and Cysteine, *Annu Rev Nutr. 24*, 539-577.
12. Ewetz, L., and Sorbo, B. (1966) Characteristics of the Cysteinesulfinate-Forming Enzyme System in Rat Liver, *Biochim Biophys Acta. 128*, 296-305.
13. Sorbo, B., and Ewetz, L. (1965) The Enzymatic Oxidation of Cysteine to Cysteinesulfinate in Rat Liver, *Biochem Biophys Res Commun. 18*, 359-363.
14. Lombardini, J. B., Singer, T. P., and Boyer, P. D. (1969) Cysteine Oxygenase, *J Biol Chem. 244*, 1172-1175.
15. Stipanuk, M., Simmons, C., Andrew Karplus, P., and Dominy, J. (2010) Thiol dioxygenases: unique families of cupin proteins, *Amino Acids*, 1-12.
16. Vitvitsky, V., Garg, S. K., and Banerjee, R. (2011) Taurine Biosynthesis by Neurons and Astrocytes, *J Biol Chem. 286*, 32002-32010.
17. Kabil, O., and Banerjee, R. (2010) Redox Biochemistry of Hydrogen Sulfide, *J Biol Chem. 285*, 21903-21907.
18. Chai, S. C., Jerkins, A. A., Banik, J. J., Shalev, I., Pinkham, J. L., Uden, P. C., and Maroney, M. J. (2005) Heterlogous Expression, Purification, and Characterization of Recombinant Rat Cysteine Dioxygenase, *J Biol Chem. 280*, 9865-9869.
19. Dominy, J. E., Jr., Simmons, C. R., Karplus, P. A., Gehring, A. M., and Stipanuk, M. H. (2006) Identification and Characterization of Bacterial Cysteine Dioxygenases: a New Route of Cysteine Degradation for Eubacteria, *J Bacteriol. 188*, 5561-5569.
20. Bagley, P. J., Hirschberger, L. L., and Stipanuk, M. H. (1995) Evaluation and Modification of an Assay Procedure for Cysteine Dioxygenase Activity: HPLC Method for Measurement of Cysteine Sulfinate and Demonstration of Physiological Relevance of Cysteine Dioxygenase Activity in Cysteine Catabolism, *Anal Biochem. 227*, 40-48.

21. Driggers, C. M., Cooley, R. B., Sankaran, B., Hirschberger, L. L., Stipanuk, M. H., and Karplus, P. A. (2013) Cysteine Dioxygenase Structures from pH 4 to 9: Consistent Cys-Persulfenate Formation at Intermediate pH and a Cys-Bound Enzyme at Higher pH, *Molecular Microbiology 425*, 3121-3136.
22. McCoy, J. G., Bailey, L. J., Bitto, E., Bingman, C. A., Aceti, D. J., Fox, B. G., and Phillips, G. N., Jr. (2006) Structure and mechanism of mouse cysteine dioxygenase, *Proc Natl Acad Sci USA. 103*, 3084-3089.
23. Simmons, C. R., Krishnamoorthy, K., Granett, S. L., Schuller, D. J., Dominy, J. E., Begley, T. P., Stipanuk, M. H., and Karplus, P. A. (2008) A Putative Fe^{2+}-Bound Persulfenate Intermediate in Cysteine Dioxygenase, *Biochemistry 47*, 11390-11392.
24. Simmons, C. R., Liu, Q., Huang, Q., Hao, Q., Begley, T. P., Karplus, P. A., and Stipanuk, M. H. (2006) Crystal Structure of Mammalian Cysteine Dioxygenase, *J Biol Chem. 281*, 18723-18733.
25. Ye, S., Wu, X. a., Wei, L., Tang, D., Sun, P., Bartlam, M., and Rao, Z. (2007) An Insight into the Mechanism of Human Cysteine Dioxygenase: Key Roles of the Thioether-Bonded Tyrosine-Cysteine Cofactor, *J Biol Chem. 282*, 3391-3402.
26. Straganz, G. D., and Nidetzky, B. (2006) Variations of the 2-His-1-carboxylate Theme in Mononuclear Non-Heme Fe(II) Enzymes, *ChemBioChem 7*, 1536-1548.
27. Unpublished crystal structure, RCSB Protein Data Bank ID (3BAL). http://www.rcsb.org
28. Diebold, A. R., Neidig, M. L., Moran, G. R., Straganz, G. D., and Solomon, E. I. (2010) The Three-His Triad in Dke1: Comparisons to the Classical Facial Triad, *Biochemistry 49*, 6945-6952.
29. Straganz, G. D., Diebold, A. R., Egger, S., Nidetzky, B., and Solomon, E. I. (2010) Kinetic and CD/MCD Spectroscopic Studies of the Atypical, Three-His-Ligated, Non-Heme Fe^{2+} Center in Diketone Dioxygenase: The Role of Hydrophilic Outer Shell Residues in Catalysis, *Biochemistry 49*, 996-1004.
30. Dominy, J. E., Simmons, C. R., Hirschberger, L. L., Hwang, J., Coloso, R. M., and Stipanuk, M. H. (2007) Discovery and Characterization of a Second Mammalian Thiol Dioxygenase, Cysteamine Dioxygenase, *J Biol Chem. 282*, 25189-25198.
31. Bruland, N., Wubbeler, J. H., and Steinbuchel, A. (2009) 3-mercaptopropionate dioxygenase, a cysteine dioxygenase homologue, catalyzes the initial step of 3-mercaptopropionate catabolism in the 3,3-thiodipropionic acid-degrading bacterium variovorax paradoxus, *The Journal of biological chemistry 284*, 660-672.
32. Brandt, U., Waletzko, C., Voigt, B., Hecker, M., and Steinbuchel, A. (2014) Mercaptosuccinate metabolism in Variovorax paradoxus strain B4-a proteomic approach, *Applied microbiology and biotechnology 98*, 6039-6050.
33. Ito, N., Phillips, S. E. V., Stevens, C., Ogel, Z. B., McPherson, M. J., Keen, J. N., Yadav, K. D. S., and Knowles, P. F. (1991) Novel thioether bond revealed by a 1.7 Å crystal structure of galactose oxidase, *Nature 350*, 87-90.
34. Schnell, R., Sandalova, T., Hellman, U., Lindqvist, Y., and Schneider, G. (2005) Siroheme- and [Fe_4-S_4]-dependent NirA from *Mycobacterium tuberculosis* Is a Sulfite Reductase with a Covalent Cys-Tyr Bond in the Active Site, *J Biol Chem. 280*, 27319-27328.
35. Whittaker, J. W. (2003) Free Radical Catalysis by Galactose Oxidase, *Chem Rev. 103*, 2347-2363.
36. Dominy, J. E., Jr., Hwang, J., Guo, S., Hirschberger, L. L., Zhang, S., and Stipanuk, M. H. (2008) Synthesis of Amino Acid Cofactor in Cysteine Dioxygenase Is

Regulated by Substrate and Represents a Novel Post-translational Regulation of Activity, *J Biol Chem. 283*, 12188-12201.

37. Pierce, B., Gardner, J., Bailey, L., Brunold, T., and Fox, B. (2007) Characterization of the nitrosyl adduct of substrate-bound mouse systeine dioxygenase by electron paramagnetic resonance: electronic structure of the active site and mechanistic implications, *Biochemistry 46*, 8569-8578.
38. Easson, L. H., and Stedman, E. (1933) Studies on the relationship between chemical constitution and physiological action: Molecular dissymmetry and physiological activity, *The Biochemical journal 27*, 1257-1266.
39. Siakkou, E., Rutledge, M. T., Wilbanks, S. M., and Jameson, G. N. L. (2011) Correlating crosslink formation with enzymatic activity in cysteine dioxygenase, *Biochim Biophys Acta. 1814*, 2003-2009.
40. Li, W., Blaesi, E. J., Pecore, M. D., Crowell, J. K., and Pierce, B. S. (2013) Second-sphere interactions between the C93-Y157 cross-link and the substrate-bound Fe site influence the O_2-coupling efficiency in mouse cysteine dioxygenase, *Biochemistry 52*, 9104-9119.
41. Solomon, E. I., Decker, A., and Lehnert, N. (2003) Non-heme iron enzymes: contrasts to heme catalysis, *Proc Natl Acad Sci USA. 100*, 3589-3594.
42. Solomon, E. I., Brunold, T. C., Davis, M. I., Kemsley, J. N., Lee, S.-K., Lehnert, N., Neese, F., Skulan, A. J., Yang, Y.-S., and Zhou, J. (2000) Geometric and Electronic Structure/Function Correlations in Non-Heme Iron Enzymes, *Chem Rev. 100*, 235-349.
43. Costas, M., Mehn, M. P., Jensen, M. P., and Que, L. J. (2004) Dioxygen Activation at Mononuclear Nonheme Iron Active Sites: Enzymes, Models, and Intermediates, *Chem Rev. 104*, 939-986.
44. Kumar, D., Thiel, W., and de Visser, S. P. (2011) Theoretical Study on the Mechanism of the Oxygen Activation Process in Cysteine Dioxygenase Enzymes, *J Am Chem Soc. 133*, 3869-3882.
45. de Visser, S. P., and Straganz, G. D. (2009) Why Do Cysteine Dioxygenase Enzymes Contain a 3-His Ligand Motif Rather than a 2His/1Asp Motif Like Most Nonheme Dioxygenases?, *J Phys Chem A. 113*, 1835-1846.
46. Aluri, S., and de Visser, S. P. (2007) The Mechanism of Cysteine Oxygenation by Cysteine Dioxygenase Enzymes, *J Am Chem Soc. 129*, 14846-14847.
47. Crawford, J. A., Li, W., and Pierce, B. S. (2011) Single turnover of substrate-bound ferric cysteine dioxygenase (CDO) with superoxide anion: enzymatic reactivation, product formation, and a transient intermediate, *Biochemistry*, (Just Accepted, reference bi2011724).
48. Rocklin, A. M., Tierney, D. L., Kofman, V., Brunhuber, N. M. W., Hoffman, B. M., Christoffersen, R. E., Reich, N. O., Lipscomb, J. D., and Que, L. (1999) Role of the nonheme Fe(II) center in the biosynthesis of the plant hormone ethylene, *Proc Natl Acad Sci USA. 96*, 7905-7909.
49. Brown, C. D., Neidig, M. L., Neibergall, M. B., Lipscomb, J. D., and Solomon, E. I. (2007) VTVH-MCD and DFT Studies of Thiolate Bonding to $\{FeNO\}^7/\{FeO2\}^8$ Complexes of Isopenicillin N Synthase: Substrate Determination of Oxidase versus Oxygenase Activity in Nonheme Fe Enzymes, *J Am Chem Soc. 129*, 7427-7438.
50. Hirao, H., and Morokuma, K. (2010) Ferric Superoxide and Ferric Hydroxide Are Used in the Catalytic Mechanism of Hydroxyethylphosphonate Dioxygenase: A Density Functional Theory Investigation, *J Am Chem Soc. 132*, 17901-17909.

51. Denisov, I. G., Mak, P. J., Makris, T. M., Sligar, S. G., and Kincaid, J. R. (2008) Resonance Raman Characterization of the Peroxo and Hydroperoxo Intermediates in Cytochrome P450, *J Phys Chem A. 112*, 13172-13179.
52. Galinato, M. G. I., Spolitak, T., Ballou, D. P., and Lehnert, N. (2010) Elucidating the Role of the Proximal Cysteine Hydrogen-Bonding Network in Ferric Cytochrome P450cam and Corresponding Mutants Using Magnetic Circular Dichroism Spectroscopy, *Biochemistry 50*, 1053-1069.
53. Hirotsu, S., Chu, G. C., Unno, M., Lee, D.-S., Yoshida, T., Park, S.-Y., Shiro, Y., and Ikeda-Saito, M. (2004) The Crystal Structures of the Ferric and Ferrous Forms of the Heme Complex of HmuO, a Heme Oxygenase of *Corynebacterium diphtheriae*, *J Biol Chem. 279*, 11937-11947.
54. Mbughuni, M. M., Chakrabarti, M., Hayden, J. A., Bominaar, E. L., Hendrich, M. P., Münck, E., and Lipscomb, J. D. (2010) Trapping and spectroscopic characterization of an Fe^{III}-superoxo intermediate from a nonheme mononuclear iron-containing enzyme, *Proc Natl Acad Sci USA. 107*, 16788-16793.
55. Emerson, J. P., Kovaleva, E. G., Farquhar, E. R., Lipscomb, J. D., and Que, L. (2008) Swapping metals in Fe- and Mn-dependent dioxygenases: Evidence for oxygen activation without a change in metal redox state, *Proc Natl Acad Sci USA. 105*, 7347-7352.
56. Gunderson, W. A., Zatsman, A. I., Emerson, J. P., Farquhar, E. R., Que, L., Lipscomb, J. D., and Hendrich, M. P. (2008) Electron Paramagnetic Resonance Detection of Intermediates in the Enzymatic Cycle of an Extradiol Dioxygenase, *J Am Chem Soc. 130*, 14465-14467.
57. Solomon, E. I., Decker, A., and Lehnert, N. (2003) Non-heme iron enzymes: Contrasts to heme catalysis, *Proc Natl Acad Sci U S A 100*, 3589-3594.
58. Pikus, J. D., Studts, J. M., Achim, C., Kauffmann, K. E., Munck, E., Steffan, R. J., McClay, K., and Fox, B. G. (1996) Recombinant toluene-4-monooxygenase: catalytic and Mossbauer studies of the purified diiron and rieske components of a four-protein complex, *Biochemistry 35*, 9106-9119.
59. Solomon, E. I., Brunold, T. C., Davis, M. I., Kemsley, J. N., Lee, S. K., Lehnert, N., Neese, F., Skulan, A. J., Yang, Y. S., and Zhou, J. (2000) Geometric and electronic structure/function correlations in non-heme iron enzymes, *Chem Rev 100*, 235-350.
60. Wallar, B. J., and Lipscomb, J. D. (1996) Dioxygen Activation by Enzymes Containing Binuclear Non-Heme Iron Clusters, *Chem Rev 96*, 2625-2658.
61. Kurtz, D. M. (1990) Oxo-Bridged and Hydroxo-Bridged Diiron Complexes - a Chemical Perspective on a Biological Unit, *Chemical Reviews 90*, 585-606.
62. Kurtz, D. M., Boice, E., Caranto, J. D., Frederick, R. E., Masitas, C. A., and Miner, K. D. Iron: Non-Heme Proteins with Diiron-Carboxylate Active Sites, in *Encyclopedia of Inorganic and Bioinorganic Chemistry*, John Wiley & Sons, Ltd.
63. Kurtz Jr, D. M. (1997) Structural similarity and functional diversity in diiron-oxo proteins, *JBIC Journal of Biological Inorganic Chemistry 2*, 159-167.
64. Donald M. Kurtz Jr, E. B., Jonathan D. Caranto, Rosanne E. Frederick, Cesar A. Masitas, Kyle D. Miner. (2013) Iron: Non-Heme Proteins with Diiron-Carboxylate Active Sites, *Encyclopedia of Inorganic and Bioinorganic Chemistry*.
65. Lei, Q. P., Cui, X., Kurtz, D. M., Amster, I. J., Chernushevich, I. V., and Standing, K. G. (1998) Electrospray mass spectrometry studies of non-heme iron-containing proteins, *Anal Chem. 70*, 1838-1846.

66. Notomista, E., Lahm, A., Di Donato, A., and Tramontano, A. (2003) Evolution of Bacterial and Archaeal Multicomponent Monooxygenases, *J Mol Evol. 56*, 435-445.
67. Feig, A. L., and Lippard, S. (1993) Reations of non-heme iron(II) centers with dioxygen in biology and chemistry, *Chem Rev. 94*, 759-805.
68. Wallar, B. J., and Lipscomb, J. D. (1996) Dioxygen activation by enzymes containing binuclear non-heme iron clusters, *Chem Rev. 96*, 2625-2658.
69. Broadwater, J. A., Ai, J., Loehr, T. M., Sanders-Loehr, J., and Fox, B. G. (1998) Peroxodiferric intermediate of stearoyl-acyl carrier protein delta 9 desaturase: oxidase reactivity during single turnover and implications for the mechanism of desaturation, *Biochemistry 37*, 14664-14671.
70. Sjöberg, B. M., Karlsson, M., and Jornvall, H. (1987) Half-site reactivity of the tyrosyl radical of ribonucleotide reductase from *Escherichia coli*, *J Biol Chem. 262*, 9736-9743.
71. Ge, J., Perlstein, D. L., Nguyen, H. H., Bar, G., Griffin, R. G., and Stubbe, J. (2001) Why multiple small subunits (Y2 and Y4) for yeast ribonucleotide reductase? Toward understanding the role of Y4, *Proc Natl Acad Sci U S A 98*, 10067-10072.
72. Sommerhalter, M., Voegtli, W. C., Perlstein, D. L., Ge, J., Stubbe, J., and Rosenzweig, A. C. (2004) Structures of the Yeast Ribonucleotide Reducatase Rnr2 and Rnr4 Homodimers, *Biochemistry 43*, 7736-7742.
73. Lyle, K. S., Haas, J. A., and Fox, B. G. (2003) Rapid-Mix and Chemical Quench Studies of Ferredoxin-Reduced Stearoyl-Acyl Carrier Protein Desaturase, *Biochemistry 42*, 5857-5866.
74. Pierce, B. S., Elgren, T. E., and Hendrich, M. P. (2003) Mechanistic implications for the formation of the diiron cluster in ribonucleotide reductase provided by quantitative EPR spectroscopy, *Journal of the American Chemical Society 125*, 8748-8759.
75. Pierce, B. S., and Hendrich Michael, P. (2005) Local and global effects of metal binding within the small subunit of ribonucleotide reductase, *Journal of the American Chemical Society 127*, 3613-3623.
76. Pierce, B. S., Sobrado, P., Elsen, N. L., Charkrabarti, M., Münck, E., and Fox, B. G. Pre-steady state and spectroscopic characterizaton of substrate-gated reduction of stearoly-ACP Δ^9-Desaturase by [2Fe-2S] ferredoxin, *(unpublished results)*.
77. Mathevon, C., Pierrel, F., Oddou, J.-L., Garcia-Serres, R., Blondin, G., Latour, J.-M., Menage, S., Gambarelli, S., Fontecave, M., and Atta, M. (2007) tRNA-modifying MiaE protein from *Salmonella typhimurium* is a nonheme diiron monooxygenase, *Proc Natl Acad Sci U S A 104*, 13295-13300.
78. Corder, A. L., Subedi, B. P., Zhang, S., Dark, A. M., Foss, F. W., and Pierce, B. S. (2013) Peroxide-Shunt Substrate-Specificity for the *Salmonella typhimurium* O_2-Dependent tRNA Modifying Monooxygenase (MiaE), *Biochemistry 52*, 6182-6196.
79. Björk, G. R., Ericson, J. U., Gustafsson, C. E. D., Hagervall, T. G., Jonsson, Y. H., and Wikstrom, P. M. (1987) Transfer RNA modification, *Annu Rev Biochem. 56*, 263-285.
80. Durand, J. M., Björk, G. R., Kuwae, A., Yoshikawa, M., and Sasakawa, C. (1997) The modified nucleoside 2-methylthio-N^6-isopentenyladenosine in tRNA of *Shigella flexneri* is required for expression of virulence genes *J Bacteriol. 179*, 5777-5782.
81. Persson, B. C. (1993) Modification of tRNA as a regulatory device, *Mol Microbiol. 8*, 1011-1016.

82. Ajitkumar, P., and Cherayil, J. D. (1985) Presence of 2-methylthioribosyl-trans-zeatin in *Azotobacter vinelandii* tRNA, *J Bacteriol. 162*, 752-755.
83. Kaminska, K. H., Baraniak, U., Boniecki, M., Nowaczyk, K., Czerwoniec, A., and Bujnicki, J. M. (2008) Structural bioinformatics analysis of enzymes involved in the biosynthesis pathway of the hypermodified nucleoside $ms^2io^6A_{37}$ in tRNA, *Proteins 70*, 1-18.
84. Persson, B. C. (1993) Modification of tRNA as a regulatory device, *Mol Microbiol 8*, 1011-1016.
85. Bjork, G. R., Durand, J. M., Hagervall, T. G., Leipuviene, R., Lundgren, H. K., Nilsson, K., Chen, P., Qian, Q., and Urbonavicius, J. (1999) Transfer RNA modification: influence on translational frameshifting and metabolism, *FEBS Lett 452*, 47-51.
86. Bjork, G. R., Ericson, J. U., Gustafsson, C. E., Hagervall, T. G., Jonsson, Y. H., and Wikstrom, P. M. (1987) Transfer RNA modification, *Annu Rev Biochem 56*, 263-287.
87. Mathevon, C., Pierrel, F., Oddou, J. L., Garcia-Serres, R., Blondin, G., Latour, J. M., Menage, S., Gambarelli, S., Fontecave, M., and Atta, M. (2007) tRNA-modifying MiaE protein from *Salmonella typhimurium* is a nonheme diiron monooxygenase, *Proc Natl Acad Sci U S A 104*, 13295-13300.
88. Petersson, L., Graslund, A., Ehrenberg, A., Sjöberg, B. M., and Reichard, P. (1980) The iron center in ribonucleotide reductase from *Escherichia coli*, *J Biol Chem 255*, 6706-6712.
89. Moore, J. A., and Poulter, C. D. (1997) *Escherichia coli* dimethylallyl diphosphate:tRNA dimethylallyltransferase: A binding mechanism for recombinant enzyme, *Biochemistry 36*, 604-614.
90. Anton, B. P., Russell, S. P., Vertrees, J., Kasif, S., Raleigh, E. A., Limbach, P. A., and Roberts, R. J. (2010) Functional characterization of the YmcB and YqeV tRNA methylthiotransferases of *Bacillus subtilis*, *Nucleic Acids Research 38*, 6195-6205.
91. Pierrel, F., Douki, T., Fontecave, M., and Atta, M. (2004) MiaB Protein is a bifunctional radical-S-adenosylmethionine enzyme involved in thiolation and methylation of tRNA, *J Biol Chem 279*, 47555-47563.
92. Arragain, S., Handelman, S. K., Forouhar, F., Wei, F.-Y., Tomizawa, K., Hunt, J. F., Douki, T., Fontecave, M., Mulliez, E., and Atta, M. (2010) Identification of Eukaryotic and Prokaryotic Methylthiotransferase for Biosynthesis of 2-Methylthio-N6-threonylcarbamoyladenosine in tRNA, *J Biol Chem. 285*, 28425-28433.
93. Björk, G. R., Durand, J. M., Hagervall, T. G., Leipuviene, R., Lundgren, H. K., Nilsson, K., Chen, P., Qian, Q., and Urbonavicius, J. (1999) Transfer RNA modification: influence on translational frameshifting and metabolism, *FEBS Lett. 452*, 47-51.
94. Esberg, B., Leung, H.-C. E., Tsui, H.-C. T., Björk, G. R., and Winkler, M. E. (1999) Identification of the *miaB* Gene, Involved in Methylthiolation of Isopentenylated A_{37} Derivatives in the tRNA of *Salmonella typhimurium* and *Escherichia coli*, *J Bacteriol. 181*, 7256-7265.
95. Buck, M., and Ames, B. N. (1984) A modified nucleotide in tRNA as a possible regulator of aerobiosis: Synthesis of cis-2-methyl-thioribosylzeatin in the tRNA of Salmonella, *Cell 36*, 523-531.
96. Esberg, B., and Björk, G. R. (1995) The methylthio group (ms^2) of N^6-(4-hydroxyisopentenyl)-2-methylthioadenosine (ms^2io^6A) present next to the anticodon contributes to the decoding efficiency of the tRNA, *J Bacteriol. 177*, 1967-1975.

97. Bailey, L. J., and Fox, B. G. (2009) Crystallographic and catalytic studies of the peroxide-shunt reaction in a diiron hydroxylase, *Biochemistry 48*, 8932-8939.

98. Froland, W. A., Andersson, K. K., Lee, S.-K., Liu, Y., and Lipscomb, J. D. (1992) Methane Monooxygenase Component B and Reductase Alter the Regioselectivity of the Hydroxylase Component-catalyzed Reactions, *J Biol Chem. 267*, 17588-17597.

99. Hirao, H., Li, F., Que, L., Jr., and Morokuma, K. (2011) Theoretical study of the mechanism of oxoiron(IV) formation from H2O2 and a nonheme iron(II) complex: O-O cleavage involving proton-coupled electron transfer, *Inorg Chem. 50*, 6637-6648.

100. Murray, L. J., and Lippard, S. J. (2007) Substrate trafficking and dioxygen activation in bacterial multicomponent monooxygenases, *Accounts of chemical research 40*, 466-474.

101. Kopp, D. A., Gassner, G. T., Blazyk, J. L., and Lippard, S. J. (2001) Electron-transfer reactions of the reductase component of soluble methane monooxygenase from Methylococcus capsulatus (Bath), *Biochemistry 40*, 14932-14941.

102. Lee, D., and Lippard, S. J. (2002) Synthetic analogue of the [Fe(2)(μ-OH)(2)(μ-O(2)CR)](3+) core of soluble methane monooxygenase hydroxylase via synthesis and dioxygen reactivity of carboxylate-bridged diiron(II) complexes, *Inorganic chemistry 41*, 827-837.

103. Lipscomb, J. D. (1994) Biochemistry of the soluble methane monooxygenase, *Annu Rev Microbiol. 48*, 371-399.

104. Baik, M. H., Newcomb, M., Friesner, R. A., and Lippard, S. J. (2003) Mechanistic studies on the hydroxylation of methane by methane monooxygenase, *Chem Rev. 103*, 2385-2419.

105. Murray, L. J., Naik, S. G., Ortillo, D. O., Garcia-Serres, R., Lee, J. K., Huynh, B. H., and Lippard, S. J. (2007) Characterization of the arene-oxidizing intermediate in ToMOH as a diiron(III) species, *J Am Chem Soc. 129*, 14500-14510.

106. Gustilo, E. M., Vendeix, F. A. P., and Agris, P. F. (2008) tRNA's modifications bring order to gene expression, *Curr Opin Microbiol. 11*, 134-140.

107. Björk, G. R., Ericson, J. U., Gustafsson, C. E. D., Hagervall, T. G., Jonsson, Y. H., and Wikstrom, P. M. (1987) Transfer RNA Modification, *Annu Rev Biochem. 56*, 263-285.

108. Persson, B. C. (1993) Modification of tRNA as a regulatory device, *Mol Microbiol. 8*, 1011-1016.

109. Petersson, L., Graslund, A., Ehrenberg, A., Sjoberg, B. M., and Reichard, P. (1980) The iron center in ribonucleotide reductase from Escherichia coli, *J Biol Chem. 255*, 6706-6712.

110. Durand, J. M., Bjork, G. R., Kuwae, A., Yoshikawa, M., and Sasakawa, C. (1997) The modified nucleoside 2-methylthio-N6-isopentenyladenosine in tRNA of *Shigella flexneri* is required for expression of virulence genes *J Bacteriol. 179*, 5777-5782.

111. Pierrel, F., Douki, T., Fontecave, M., and Atta, M. (2004) MiaB Protein is a bifunctional radical-S-adenosylmethionine enzyme involved in thiolation and methylation of tRNA, *J Biol Chem. 279*, 47555-47563.

112. Persson, B., Olafsson, O., Lundgren, H., Hederstedt, L., and Bjork, G. (1998) The $ms^2io^6A_{37}$ modification of tRNA in *Salmonella typhurium* regulates growth on Citric Acid cycle intermediates, *J Bacteriol. 180*, 3144-3151.

113. Persson, B. C., and Bjork, G. R. (1993) Isolation of the Gene (*miaE*) Encoding the Hydroxylase Involved in the Synthesis of 2-Methylthio-cis-Ribozeatin in tRNA of *Salmonella typhimurium* and Characterization of Mutants, *J Bacteriol. 175*, 7776-7785.
114. Kuo, H. H., and Mauk, A. G. (2012) Indole peroxygenase activity of indoleamine 2,3-dioxygenase, *Proc Natl Acad Sci U S A 109*, 13966-13971.
115. Brookes, E. H., and Demeler, B. (2007) Parsimonious regularization using genetic algorithms applied to the analysis of analytical ultracentrifugation experiments, in *Proceedings of the 9th annual conference on Genetic and evolutionary computation*, pp 361-368.
116. Demeler, B., and Brookes, E. (2008) Monte carlo analysis of sedimentation experiments, *Colloid Polym Sci. 286*, 129-137.
117. Newman, L., and Wackett, L. (1995) Purification and characterization of toluene 2-monooxygenase from *Bukholderia cepacia* G4., *Biochemistry 34*, 14066-14076.
118. Abragam, A., and Bleaney, B. (1970) *Electron Paramagnetic Resonance of Transition Ions (International Series of Monographs on Physics)*.
119. Chomczynski, P., and Sacchi, N. (1987) Single-step method of RNA isolation by acid guanidinium thiocyanate-phenol-chloroform extraction, *Anal Biochem. 162*, 156-159.
120. Connolly, D. M., and Winkler, M. E. (1989) Genetic and physiological relationships among the miaA Gene, 2-Methylthio-N6-(z2-Isopentenyl)-adenosine tRNA modification, and spontaneous mutagenesis in *Escherichia coli* K-12, *J Bacteriol. 171*, 3233-3246.
121. Gehrke, C. W., and Kuo, K. C. (1989) Ribonucleoside Analysis by Reversed-Phase High-Performance Liquid-Chromatography, *J Chromatogr. 471*, 3-36.
122. Yost, R. A., and Fetterolf, D. D. (1983) Tandem mass spectrometry (MS/MS) instrumentation, *Mass Spectrom Rev. 2*, 1-45.
123. Spichal, L. (2009) Substituted 6-anilinopurine derivatives as inhibitors of cytokinin oxidase/dehydrogenase and preparations containing these derivatives; Patent version number (2,009,003,428).
124. Ragnarsson, U., and Grehn, L. (1991) Novel Gabriel reagents, *Acc Chem Res. 24*, 285-289.
125. Dumas, D. J. (1988) Total synthesis of peramine, *J Org Chem 53*, 4650-4653.
126. Mahmud, H. (2000) Thesis title; "Studies toward the total synthesis of martinelline and martinellic acid"; Department of Chemistry and Biochemistry The University of Texas at Arlington, Arlington.
127. Montgomery, J. A., and Holum, L. B. (1957) Synthesis of potential anticancer agents. III. hydrazino analogs of biologically active purines, *J Am Chem Soc. 79*, 2185-2188.
128. Oumata, N., Ferandin, Y., Meijer, L., and Galons, H. (2009) Practical Synthesis of Roscovitine and CR8, *Org Process Res Dev. 13*, 641-644.
129. Liu, H., and Pinto, B. M. (2004) Efficient synthesis of the glucosidase inhibitor blintol, the selenium analogue of the naturally occurring glycosidase inhibitor salacinol, *J Org Chem 70*, 753-755.
130. Vorbrüggen, H., and Ruh-Pohlenz, C. (2001) *Handbook of nucleoside synthesis*, John Wiley & Sons, Inc.
131. Ginisty, M., Gravier-Pelletier, C., and Le Merrer, Y. (2006) Chemical investigations in the synthesis of O-serinyl aminoribosides, *Tetrahedron: Asymmetry 17*, 142-150.

132. Sun, Z., Wang, H., Wen, K., Li, Y., and Fan, E. (2011) Solvent-free or low-solvent large-scale preparation of chloropyrimidine and analogues, *J Org Chem 76*, 4149-4153.
133. Piguel, S., and Legraverend, M. (2007) Selective amidation of 2,6-dihalogenopurines: application to the synthesis of new 2,6,9-trisubstituted purines, *J Org Chem. 72*, 7026-7029.
134. Hara, R., Sato, K., Sun, W., and Takahashi, T. (1999) Catalytic dechlorination of aromatic chlorides using Grignard reagents in the presence of $(C_5H_5)_2TiCl_2$, *Chem Commun.*, 845-846.
135. Powell, D. A., and Batey, R. A. (2002) Total synthesis of the alkaloids martinelline and martinellic acid via a hetero Diels-Alder multicomponent coupling reaction, *Org Lett. 4*, 2913-2916.
136. Hemström, P., and Irgum, K. (2006) Hydrophilic interaction chromatography, *J. Sep Sci. 29*, 1784-1821.
137. Kurtz, D. M. (1990) Oxo-Bridged and Hydroxo-Bridged Diiron Complexes - a Chemical Perspective on a Biological Unit, *Chem Rev. 90*, 585-606.
138. Ehrenberg, A., and Reichard, P. (1972) Electron spin resonance of the iron-containing protein B2 from ribonucleotide reductase, *J Biol Chem. 247*, 3485-3488.
139. Sanders-Loehr, J., Wheeler, W., Shiemke, A., Averill, B., and Loehr, T. (1989) Electronic and Raman spectroscopic properties of oxo-bridged dinuclear iron centers in proteins and model compounds, *J Am Chem Soc. 111*, 8084-8093.
140. Fox, B. G., Shanklin, J., Somerville, C., and Münck, E. (1993) Stearoyl-acyl carrier protein delta 9 desaturase from Ricinus communis is a diiron-oxo protein, *Proc Natl Acad Sci U S A 90*, 2486-2490.
141. Cadieux, E., Vrajmasu, V., Achim, C., Powlowski, J., and Münck, E. (2002) Biochemical, Mössbauer, and EPR Studies of the diiron cluster of phenol hydroxylase from *Pseudomonas* sp. Strain CF 600, *Biochemistry 41*, 10680-10691.
142. Pikus, J. D., Studts, J. M., Achim, C., Kauffmann, K. E., Münck, E., Steffan, R. J., McClay, K., and Fox, B. G. (1996) Recombinant toluene-4-monooxygenase: catalytic and Mössbauer studies of the purified diiron and Rieske components of a four-protein complex, *Biochemistry 35*, 9106-9119.
143. Hendrich, M. P., and Debrunner, P. G. (1989) Integer-spin electron paramagnetic resonance of iron proteins, *Biophys J. 56*, 489-506.
144. Paulsen, K. E., Liu, Y., Fox, B. G., Lipscomb, J. D., Münck, E., and Stankovich, M. T. (1994) Oxidation-reduction potentials of the methane monooxygenase hydroxylase component from *Methylosinus trichosporium* OB3b, *Biochemistry 33*, 713-722.
145. Elgren, T. E., Hendrich, M. P., and Que, L., Jr. (1993) Azide binding to the diferrous clusters of the R2 protein of ribonucleotide reductase from *Escherichia coli*, *J Am Chem Soc. 115*, 9291-9292.
146. Jang, H. G., Hendrich, M. P., and Que, L. (1993) Insight into the $g \approx 16$ EPR signals of reduced diiron-oxo proteins. Structure and properties of $[Fe^{II}{}_2BPMP\{O_2P(OC_6H_5)_2\}_2]Cl$, *Inorg Chem. 32*, 911-918.
147. Vreman, H. J., Schmitz, R. Y., and Skoog, F. (1974) Synthesis of 2-methylthio-*cis*- and *trans*-ribosylzeatin and their isolation from *Pisum tRNA*, *Phytochemistry 13*, 31-37.
148. Lichtenthaler, F. W., Voss, P., and Heerd, A. (1974) Nucleosides, XX. Stannic Chloride catalyzed glycosidations of silylated purines with fully acylated sugars, *Tetrahedron Lett. 15*, 2141-2144.

149. Ottria, R., Casati, S., Manzocchi, A., Baldoli, E., Mariotti, M., Maier, J. A. M., and Ciuffreda, P. (2010) Synthesis and evaluation of in vitro anticancer activity of some novel isopenenyladenosine derivatives, *Bioorg Med Chem. 18*, 4249-4254.
150. Jordan, A., Pontis, E., Atta, M., Krook, M., Gibert, I., Barbe, J., and Reichard, P. (1994) A second class I ribonucleotide reductase in Enterobacteriaceae: characterization of the Salmonella typhimurium enzyme, *Proc Natl Acad Sci U S A 91*, 12892-12896.
151. Fox, B. G., Shanklin, J., Ai, J., Loehr, T. M., and Sanders-Loehr, J. (1994) Resonance Raman evidence for an Fe-O-Fe center in stearoyl-ACP desaturase. Primary sequence identity with other diiron-oxo proteins, *Biochemistry 33*, 12776-12786.
152. Xiong, J., Phillips, R. S., Kurtz, D. M., Jr., Jin, S., Ai, J., and Sanders-Loehr, J. (2000) The O_2 binding pocket of myohemerythrin: role of a conserved leucine, *Biochemistry 39*, 8526-8536.
153. Merkx, M., Kopp, D. A., Sazinsky, M. H., Blazyk, J. L., Müller, J., and Lippard, S. J. (2001) Dioxygen Activation and Methane Hydroxylation by Soluble Methane Monooxygenase: A Tale of Two Irons and Three Proteins, *Angew Chem Int Ed Engl. 40*, 2782-2807.
154. Kao, W. C., Wang, V. C., Huang, Y. C., Yu, S. S., Chang, T. C., and Chan, S. I. (2008) Isolation, purification and characterization of hemerythrin from Methylococcus capsulatus (Bath), *J Inorg Biochem. 102*, 1607-1614.
155. Xiong, J., Kurtz, D. M., Jr., Ai, J., and Sanders-Loehr, J. (2000) A hemerythrin-like domain in a bacterial chemotaxis protein, *Biochemistry 39*, 5117-5125.
156. Lei, Q. P., Cui, X., Kurtz, D. M., Amster, I. J., Chernushevich, I. V., and Standing, K. G. (1998) Electrospray Mass Spectrometry Studies of Non-Heme Iron-Containing Proteins, *Anal Chem. 70*, 1838-1846.
157. Sjoberg, B. M., Karlsson, M., and Jornvall, H. (1987) Half-site reactivity of the tyrosyl radical of ribonucleotide reductase from Escherichia coli, *J Biol Chem. 262*, 9736-9743.
158. Cherayil, J. D., and Lipsett, M. N. (1977) Zeatin ribonucleosides in the transfer ribonucleic acid of Rhizobium leguminosarum, Agrobacterium tumefaciens, Corynebacterium fascians, and Erwinia amylovora, *J Bacteriol. 131*, 741-744.
159. Gustilo, E. M., Vendeix, F. A. P., and Agris, P. F. (2008) tRNA's modifications bring order to gene expression, *Curr Opin Microbiol. 11*, 134-140.
160. Björk, G. R., Durand, J. M., Hagervall, T. G., Leipuviene, R., Lundgren, H. K., Nilsson, K., Chen, P., Qian, Q., and Urbonavicius, J. (1999) Transfer RNA modification: influence on translational frameshifting and metabolism, *FEBS Lett 452*, 47-51.
161. Cabello-Villegas, J., Winkler, M. E., and Nikonowicz, E. P. (2002) Solution Conformations of Unmodified and A_{37} N^6-dimethylallyl Modified Anticodon Stem-loops of *Escherichia coli* $tRNA^{Phe}$, *J Mol Biol. 319*, 1015-1034.
162. Persson, B. C. (1993) Modification of tRNA as a regulatory device, *Mol Microbiol. 8*, 1011-1016.
163. Yonath, A. (2005) ANTIBIOTICS TARGETING RIBOSOMES: Resistance, Selectivity, Synergism, and Cellular Regulation, *Annu Rev Biochem. 74*, 649-679.
164. Abbink, T. E. M., and Berkhout, B. (2008) HIV-1 reverse transcription initiation: A potential target for novel antivirals?, *Virus Res. 134*, 4-18.
165. Ju, J., Jiang, J., and Fesler, A. (2013) miRNA: the new frontier in cancer medicine, *Future Med Chem. 5*, 983-985.

166. Wu, J., Liu, S., Yu, J., Zhou, G., Rao, D., Jay, C. M., Kumar, P., Sanchez, R., Templeton, N., Senzer, N., Maples, P., Nemunaitis, J., and Brunicardi, F. C. (2014) Vertically integrated translational studies of PDX1 as a therapeutic target for pancreatic cancer via a novel bifunctional RNAi platform, *Cancer Gene Ther.* .

167. Persson, B. C., Olafsson, O., Lundgren, H. K., Hederstedt, L., and Björk, G. R. (1998) The ms^{2}io^{6}A37 modification of tRNA in *Salmonella typhimurium* regulates growth on citric acid cycle intermediates, *J Bacteriol 180*, 3144-3151.

168. Petersson, L., Gräslund, A., Ehrenberg, A., Sjöberg, B. M., and Reichard, P. (1980) The iron center in ribonucleotide reductase from *Escherichia coli*, *J Biol Chem. 255*, 6706-6712.

169. Broadwater, J. A., Ai, J., Loehr, T. M., Sanders-Loehr, J., and Fox, B. G. (1998) Peroxodiferric intermediate of stearoyl-acyl carrier protein delta-9-desaturase: oxidase reactivity during single turnover and implications for the mechanism of desaturation, *Biochemistry 37*, 14664-14671.

170. Lyle, K. S., Haas, J. A., and Fox, B. G. (2003) Rapid-mix and chemical quench studies of ferredoxin-reduced stearoyl-acyl carrier protein desaturase, *Biochemistry 42*, 5857-5866.

171. Sazinsky, M. H., and Lippard, S. J. (2006) Correlating Structure with Function in Bacterial Multicomponent Monooxygenases and Related Diiron Proteins, *Acc Chem Res. 39*, 558-566.

172. Mitchell, K. H., Studts, J. M., and Fox, B. G. (2002) Combined Participation of Hydroxylase Active Site Residues and Effector Protein Binding in a Para to Ortho Modulation of Toluene 4-Monooxygenase Regiospecificity, *Biochemistry 41*, 3176-3188.

173. Cheng, H., Westler, W. M., Xia, B., Oh, B. H., and Markley, J. L. (1995) Protein expression, selective isotopic labeling, and analysis of hyperfine-shifted NMR signals of Anabaena 7120 vegetative [2Fe-2S]ferredoxin, *Arch Biochem Biophys 316*, 619-634.

174. Hoffman, B. J., Broadwater, J. A., Johnson, P., Harper, J., Fox, B. G., and Kenealy, W. R. (1995) Lactose fed-batch overexpression of recombinant metalloproteins in *Escherichia coli* BL21 (DE3): process control yielding high levels of metal-incorporated, soluble protein, *Protein Expr Purif 6*, 646-654.

175. Leung, H. C., Chen, Y., and Winkler, M. E. (1997) Regulation of substrate recognition by the MiaA tRNA prenyltransferase modification enzyme of *Escherichia coli* K-12, *J Biol Chem. 272*, 13073-13083.

176. Greenfield, N. J. (2007) Using circular dichroism spectra to estimate protein secondary structure, *Nat. Protocols 1*, 2876-2890.

177. Abragam, A., and Bleaney, B. (1970) *Electron paramagnetic resonance of transition ions*, Oxford University Press, New York.

178. Cohen-Tannoudji, C., Diu, B., and Laloë, F. (1977) *Quantum mechanics*, Vol. II, John Wiley & Sons, New York.

179. Hendrich, M. P., Petasis, D., Arciero, D. M., and Hooper, A. B. (2001) Correlations of structure and electronic properties from EPR spectroscopy of hydroxylamine oxidoreductase, *J. Am. Chem. Soc. 123*, 2997-3005.

180. Weil, J. A., Bolton, J. R., and Wertz, J. E. (1993) *Electron paramagnetic resonance: elementary theory and practical applications*, John Wiley & Sons, Inc., New York.

181. Cockrell, A., McCormick, S. P., Moore, M. J., Chakrabarti, M., and Lindahl, P. A. (2014) Mössbauer, EPR, and Modeling Study of Iron Trafficking and Regulation in Δccc1 and CCC1-up *Saccharomyces cerevisiae*, *Biochemistry 53*, 2926-2940.

182. Haas, J. A., and Fox, B. G. (1999) Role of hydrophobic partitioning in substrate selectivity and turnover of the *Ricinus communis* stearoyl acyl carrier protein Δ^9-desaturase, *Biochemistry 38*, 12833-12840.

183. Shaw, S. J., Desiderio, D. M., Tsuboyama, K., and McCloskey, J. A. (1970) Mass spectrometry of nucleic acid components. Analogs of adenosine, *J Am Chem Soc 92*, 2510-2522.

184. Pikus, J. D., Studts, J. M., Achim, C., Kauffmann, K. E., Münck, E., Steffan, R. J., McClay, K., and Fox, B. G. (1996) Recombinant toluene-4-monooxygenase: catalytic and Mössbauer studies of the purified diiron and rieske components of a four-protein complex, *Biochemistry 35*, 9106-9119.

185. LeCloux, D. D., Barrios, A. M., Mizoguchi, T. J., and Lippard, S. J. (1998) Modeling the Diiron Centers of Non-Heme Iron Enzymes. Preparation of Sterically Hindered Diiron(II) Tetracarboxylate Complexes and Their Reactions with Dioxygen, *J Am Chem Soc. 120*, 9001-9014.

186. Clark, P. E., and Webb, J. (1981) Mössbauer spectroscopic studies of hemerythrin from *Phascolosoma lurco* (syn. *Phascolosoma Arcuatum*), *Biochemistry 20*, 4628-4632.

187. Lynch, J. B., Juarez-Garcia, C., Münck, E., and Que, L. (1989) Mössbauer and EPR studies of the binuclear iron center in ribonucleotide reductase from *Escherichia coli*. A new iron-to-protein stoichiometry, *J Biol Chem. 264*, 8091-8096.

188. Shu, L. J., Broadwater, J. A., Achim, C., Fox, B. G., Münck, E., and Que, L. (1998) EXAFS and Mössbauer characterization of the Diiron(III) site in stearoyl-acyl carrier protein Delta(9-) desaturase, *J Biol Inorg Chem. 3*, 392-400.

189. Fox, B. G., Hendrich, M. P., Surerus, K. K., Andersson, K. K., Froland, W. A., Lipscomb, J. D., and Münck, E. (1993) Mössbauer, EPR, and ENDOR studies of the hydroxylase and reductase components of methane monooxygenase from *Methylosinus trichosporium* OB3b, *J Am Chem Soc. 115*, 3688-3701.

190. Traut, T. (2008) *Allosteric Regulatory Enzymes; Chapter 2. The Limits for Life Define the Limits for Enzymes*, Springer, New York.

191. Corder, A. L., Subedi, B. P., Zhang, S., Dark, A. M., Foss, F. W., Jr., and Pierce, B. S. Peroxide-shunt substrate-specificity for the Salmonella typhimurium O2-dependent tRNA modifying monooxygenase (MiaE), *Biochemistry 52*, 6182-6196.

192. Reddie, K. G., and Carroll, K. S. (2008) Expanding the functional diversity of proteins through cysteine oxidation, *Curr Opin Chem Biol. 12*, 746-754.

193. Winyard, P. G., Moody, C. J., and Jacob, C. (2005) Oxidative activation of antioxidant defence, *Trends Biochem Sci. 30*, 453-461.

194. Trachootham, D., Alexandre, J., and Huang, P. (2009) Targeting cancer cells by ROS-mediated mechanisms: a radical therapeutic approach?, *Nat Rev Drug Discov 8*, 579-591.

195. Behave, D. P., Muse, W. B., and Carroll, K. S. (2007) Drug Targets in Mycobacterial Sulfur Metabolism, *Infect Disord Drug Targets. 7*, 140-158.

196. Deth, R., Muratore, C., Benzecry, J., Power-Charnitsky, V.-A., and Waly, M. (2008) How environmental and genetic factors combine to cause autism: A redox/methylation hypothesis, *NeuroToxicology 29*, 190-201.

197. James, S. J., Cutler, P., Melnyk, S., Jernigan, S., Janak, L., Gaylor, D. W., and Neubrander, J. A. (2004) Metabolic biomarkers of increased oxidative stress and impaired methylation capacity in children with autism, *Am J Clin Nutr. 80*, 1611-1617.

198. Gordon, C., Emery, P., Bradley, H., and Waring, H. (1992) Abnormal sulfur oxidation in systemic lupus erythematosus, *Lancett 229*, 25-26.
199. Heafield, M. T., Fearn, S., Steventon, G. B., Waring, R. H., Williams, A. C., and Sturman, S. G. (1990) Plasma cysteine and sulfate levels in patients with motor neurone, Parkinson's and Alzheimer's disease, *Neurosci Lett. 110*, 216-220.
200. Unpublished crystal structure, RCSB Protein Data Bank ID (3BAL). http://www.rcsb.org
201. Li, W., and Pierce, B. S. (2015) Steady-state substrate specificity and O_2-coupling efficiency of mouse cysteine dioxygenase, *Arch Biochem Biophys. 565*, 49-56.
202. Driggers, C. M., Hartman, S. J., and Karplus, P. A. (2015) Structures of Arg- and Gln-type bacterial cysteine dioxygenase homologs, *Protein Science 24*, 154-161.
203. Crawford, J. A., Li, W., and Pierce, B. S. Single turnover of substrate-bound ferric cysteine dioxygenase with superoxide anion: enzymatic reactivation, product formation, and a transient intermediate, *Biochemistry 50*, 10241-10253.
204. Pierce, B. S., Gardner, J. D., Bailey, L. J., Brunold, T. C., and Fox, B. G. (2007) Characterization of the Nitrosyl Adduct of Substrate-Bound Mouse Cysteine Dioxygenase by Electron Paramagnetic Resonance: Electronic Structure of the Active Site and Mechanistic Implications†, *Biochemistry 46*, 8569-8578.
205. Collins, P. F., Diehl, H., and Smith, G. F. (1959) 2,4,6-Tripyridyl-s-triazine as Reagent for Iron. Determination of Iron in Limestone, Silicates, and Refractories, *Analytical Chemistry 31*, 1862-1867.
206. Crowell, J. K., Li, W., and Pierce, B. S. (2014) Oxidative uncoupling in cysteine dioxygenase is gated by a proton-sensitive intermediate, *Biochemistry 53*, 7541-7548.
207. Denu, J. M., and Fitzpatrick, P. F. (1994) pH and kinetic isotope effects on the oxidative half-reaction of D-amino-acid oxidase, *J Biol Chem. 269*, 15054-15059.
208. Cleland, W. W. (1982) [22] The use of pH studies to determine chemical mechanisms of enzyme-catalyzed reactions, in *Methods in Enzymology* (Daniel, L. P., Ed.), pp 390-405, Academic Press.
209. Wanat, A., Schneppensieper, T., Stochel, G., van Eldik, R., Bill, E., and Wieghardt, K. (2002) Kinetics, Mechanism, and Spectroscopy of the Reversible Binding of Nitric Oxide to Aquated Iron(II). An Undergraduate Text Book Reaction Revisited., *Inorg. Chem. 41*, 4-10.
210. Li, M., Bonnet, D., Bill, E., Neese, F., Weyhermèuller, T., Blum, N., Sellmann, D., and Wieghardt, K. (2002) Tuning the Electronic Structure of Octahedral Iron Complexes [FeL(X)] (L=1-Alkyl-4,7-bis(4-tert-butyl-2-mercaptobenzyl)-1,4,7-triazacyclononane, X = Cl, CH_3O, CN, NO). The S = 1/2 - S = 3/2 Spin Equilibrium of [FeL^{Pr}(NO)], *Inorg. Chem. 41*, 3444-3456.
211. Sellmann, D., Blum, N., Heinemann, F. W., and Hess, B. A. (2001) Synthesis, Reactivity, and Structure of Strictly Homologous 18 and 19 Valence Electron Iron Nitrosyl Complexes, *Chem. Eur. J. 7*, 1874-1880.
212. Blaesi, E. J., Gardner, J. D., Fox, B. G., and Brunold, T. C. (2013) Spectroscopic and Computational Characterization of the NO Adduct of Substrate-Bound Fe(II) Cysteine Dioxygenase: Insights into the Mechanism of O2 Activation, *Biochemistry 52*, 6040-6051.
213. Clay, M. D., Cosper, C. A., Jenney, F. E., Adams, M. W. W., and Johnson, M. K. (2003) Nitric oxide binding at the mononuclear active site of reduced Pyrococcus furiosus superoxide reductase, *Proc Natl Acad Sci USA. 100*, 3796-3801.

214. Surawatanawong, P., Sproules, S., Neese, F., and Wieghardt, K. (2011) Electronic Structures and Spectroscopy of the Electron Transfer Series [Fe(NO)L2]z (z = 1+, 0, 1–, 2–,3–; L = Dithiolene), *Inorganic Chemistry 50*, 12064-12074.

215. McQuilken, A. C., Ha, Y., Sutherlin, K. D., Siegler, M. A., Hodgson, K. O., Hedman, B., Solomon, E. I., Jameson, G. N. L., and Goldberg, D. P. (2013) Preparation of Non-heme {FeNO}7 Models of Cysteine Dioxygenase: Sulfur versus Nitrogen Ligation and Photorelease of Nitric Oxide, *J Am Chem Soc. 135*, 14024-14027.

Biographical Information

Bishnu Subedi received Master of Science degree in Chemistry from Tribhuvan University Nepal in 2004. He enrolled in the University of Texas at Arlington in 2009 as a graduate student in the Department of Chemistry and Biochemistry. His doctoral research was focused on mechanistic study of metalloenzymes utilizing biochemical, biophysical and spectroscopic methods. He completed his PhD degree in chemistry in May 2015 and going to further work as a postdoctoral researcher on enzymology.